Passive Microwave Remote Sensing of Ice Cover on Large Northern Lakes: Great Bear Lake and Great Slave Lake, Northwest Territories, Canada

by

Kyung Kuk Kang

A thesis
presented to the University of Waterloo
in fulfillment of the
thesis requirement for the degree of
Doctor of Philosophy
in
Geography

Waterloo, Ontario, Canada, 2012

AUTHOR'S DECLARATION

I hereby declare that I am the sole author of this thesis. This is a true copy of the thesis, including any required final revisions, as accepted by my examiners.

I understand that my thesis may be made electronically available to the public.

ABSTRACT

Time series of brightness temperature (T_B) measurement obtained at various frequencies by the Advanced Microwave Scanning Radiometer–Earth Observing System (AMSR-E) are investigated to determine ice phenology parameters and ice thickness on Great Bear Lake (GBL) and Great Slave Lake (GSL), Northwest Territories, Canada. T_B measurements from the 6.9, 10.7, 18.7, 23.8, 36.5, and 89.0 GHz channels (H- and V- polarization) are compared to assess their potential for detecting freeze-onset (FO)/melt-onset (MO), ice-on/ice-off dates, and ice thickness on both lakes. The sensitivity of T_B measurements at 6.9, 10.7, and 18.7 GHz to ice thickness is also examined using a previously validated thermodynamic lake ice model and the most recent version of the Helsinki University of Technology (HUT) model, which accounts for the presence of a lake-ice layer under snow.

This study shows that 18.7 GHz H-pol is the most suitable AMSR-E channel for detecting ice phenology events, while 18.7 GHz V-pol is preferred for estimating lake ice thickness on the two large northern lakes. These two channels therefore form the basis of new ice cover retrieval algorithms. The algorithms were applied to map monthly ice thickness products and all ice phenology parameters on GBL and GSL over seven ice seasons (2002-2009).

Through application of the algorithms much was learned about the spatio-temporal dynamics of ice formation, decay and growth rate/thickness on the two lakes. Key results reveal that: 1) both FO and ice-on dates occur on average 10 days earlier on GBL than on GSL; 2) the freeze-up process or freeze duration (FO to ice-on) takes a comparable amount of time on both lakes (two to three weeks); 3) MO and ice-off dates occur on average one week and approximately four weeks later, respectively, on GBL; 4) the break-up process or melt duration (MO to ice-off) lasts for an equivalent period of time on both lakes (six to eight weeks); 5) ice cover duration is about three to four weeks longer on GBL compared to its more southern counterpart (GSL); and 6) end-of-winter ice thickness (April) on GBL

tends to be on average 5-15 cm thicker than on GSL, but with both spatial variations across lakes and differences between years.

ACKNOWLEDGEMENTS

First of all, I, Kevin Kang, would like to express my truthful gratitude to my advisor Dr. Claude R. Duguay for his professional supervision, research supports, and, in particular, continuous encouragements *with fresh coffee and red wine* during my Ph.D. program. My thesis could not have been finished without his academic and research supports. Furthermore, I have learned 'Being Patient' in my mind to reach the level of scientific research. Thank you very much for providing me good opportunities to explore one of the hottest topics in Cryosphere, *lake ice*, through the entire period of my graduate work at University of Waterloo. I would also like to offer my sincere appreciation to all members of my thesis committee, Dr. Chris Derksen, Dr. Stephen Howell, Dr. Antony Endres, Dr. Richard Kelly and Dr. Alexei Kouraev for their expert advice and feedback during the preparation of my thesis.

Many thanks to the most innovative research group of the World, UW-Cryogroup graduates since 2007. In particular, Laura Brown and Steve, Niina Luus, Michelle Ruddy, Miranda Lewis, Kheyrollah-Pour and Cristina Surdu, Kelly Mclean, as well as Grant Gunn, Patrick Nicholson, Andrew Kasurak, Josh King, Raymond Cabrera, Nic Svacina and Ryan Ahola. I always have enjoyed my research work, field campaigns, and Cryogroup meetings in EIT and RAC1 day and overnight as well as our Thursday night tradition at the Graduate House. Also, thanks for Scott MacFarlane and Mike Lackner in MAD-helpdesk.

A special thanks to Dr. Panseok Yang, Misuk Yun, Dr. Hyun-woo Lee, as well as Drs. Wooil Moon and Joong-Sun, Won.

Finally, I am most gratefully to my parents and my younger brother's (Dr. Seung-Kuk, Kang) family. Without their support and patience for more than five years, I would not have been able to concentrate on my favorite academic work at University of Waterloo.

TABLE OF CONTENTS

LIST OF FIGURES

LIST OF TABLES

PREFACE

In addition to introductory, research contents, study area and general conclusions chapters, this thesis contains three chapters (Chapters 4, 5 and 6) written in the form of journal articles.

One article (Chapter 5), titled "Sensitivity of brightness temperature from AMSR-E frequency channels to the seasonal evolution of lake ice thickness in Great Bear and Great Slaves Lakes*"*, was published in 2010 in *Geoscience and Remote Sensing Letters*. The second article (Chapter 4) on "Estimating ice phenology on large northern lakes from AMSR-E: Algorithm development and application to Great Bear Lake and Great Slave Lake, Canada" was published in 2012 to *The Cryosphere*. This Chapter 4 was modified from the second article. The last article (Chapter 6), titled "Estimating ice thickness on Great Bear Lake and Great Slave Lake from AMSR-E brightness temperature measurements", was recently submitted (May 2012) to *Remote Sensing of Environment*. Chapters 4, 5, and 6 are modified versions of the previously published journal articles.

The first article (Chapter 5) is the result of direct collaboration with Prof. Claude R. Duguay, Dr. Stephen E. L. Howell, Dr. Chris P. Derksen, and Prof. Richard E. J. Kelly who provided guidance and comments throughout the duration of the study. Prof. Duguay advised with the initial scheme of the article as well as with the interpretation of results. Prof. Kelly's contributions included explanations of AMSR-E data structure and processing of brightness temperature measurements. Drs. Derksen and Howell of Environment Canada provided comments in committee meeting and during the preparation of the manuscript.

The second (Chapter 4) and third articles (Chapter 6) are the result of a close collaboration with Prof. Duguay. He contributed some ideas during the early stages of the development of lake ice phenology and thickness algorithms, as well as for the validation of the algorithms. Dr. Stephen Howell shared some of his experience in the development of active and passive microwave sea ice retrieval algorithm, which was useful when developing the

lake ice phenology algorithm. He also provided useful comments on the second article before its submission. Mr. Juha Lemmetyinen contributed simulated brightness temperatures of GBL and GSL obtained with the Helsinki University of Technology (HUT) model for comparison with AMSR-E measurements used in the third article. In this last article, Prof. Yulia Gel provided valuable statistical advice for the improvement of ice thickness retrieval algorithm using non-adaptive scheme of linear regression and out-of-sample prediction methodology.

Chapter 1: Introduction

When a lake surface approaches 4 °C, which is the temperature of maximum density of freshwater, the surface water becomes denser. With further cooling, the surface water layer becomes stable and lighter. As this water layer approaches the freezing point (0 °C), ice starts to form on the lake surface (Jeffries et al., 2005b). The thermodynamics of lake ice depends on energy movement, which occurs during temperature change. Heat and energy transfer influences ice growth and thickening, and the timing of freeze-up and break-up. Freshwater ice scientists refer to freeze-up/break-up dates and the duration of ice on lakes (and rivers) as ice phenology (Jeffries and Morris, 2007). More specifically, lake ice phenology encompasses: freeze-up in the autumn; a long period of growth and thickening in winter; a short period of ice melting and thinning, and finally, break-up and the complete disappearance of the ice cover in spring, depending on lake bathymetry and its latitudinal position. Lake ice growth occurs between ice-on date (late stage of freeze-up period) and melt-onset (early stage of break-up period) as a result of energy loss by the conductive heat flow to the atmosphere above from the water under the ice through the ice/snow interface.

As freeze-up and break-up dates, and maximum ice thickness, are good proxy indicators of climate variability and change, such ice information on lakes is crucial for understanding lake ice thermodynamics as well as the energy balance of the cold regions of the Northern Hemisphere. Understanding of lake ice phenology contributes not only to our understanding of environmental changes in northern Canada but also provides useful information for hydroelectric power generation and winter transportation on ice roads in the North. Shorter ice cover duration, thinner ice, and earlier break-up can influence the winter road season, thereby affecting industrial development and the delivery of goods in northern communities. Furthermore, changes in lake ice duration play a significant role in hydrological processes, and have important ecological implications (Duguay et al., 2006). For the aspects of lake ecology, the duration of ice cover and the date of break-up have an impact on lake oxygenation, fish winterkills, phytoplankton production, species

composition and abundance (Livingstone, 1997). Given the significance of freshwater ice as a climate indicator, the Global Climate Observing System (GCOS) requires the precise observation of complete freeze-over and water clear of ice dates (ideally at daily intervals) for several hundred of lakes at high latitudes (Key et al., 2007). In a recent study, it was also shown that knowledge of the entire extent of lake ice cover average is useful for calculating the total amount of shortwave radiation relating the area-averaged deficit of heat received by the lake during a winter/spring season (Austin and Colman, 2007).

Circumpolar regions are strongly sensitive to global warming, which causes increasing melting of snow and ice; significant alteration of weather patterns (Woo et al., 2007). Trends towards earlier water clear of ice dates (i.e. when ice is no longer present on a lake), as determined through the analysis of ground-based observations, have provided much of the explanation for the increasingly shorter ice cover season on many lakes across Canada during the later part of the twentieth century (Duguay et al., 2006). Canada's government-funded historical ground-based observational network has provided much of the evidence for the documented changes and the links established with atmospheric forcings. However, this network has almost totally vanished over the last two decades. Also, although the ground-based ice observations were spatially consistent (usually the same site was observed year after year), they were not representative of the entire lake surfaces. Now, satellite remote sensing provides an attractive alternative for rebuilding the lost observational lake ice network, which had been previously available in a lake ice database, and also for providing more spatially representative information regarding both ice phenology and ice thickness.

1.1 Thesis goal and objectives

The main goal of this research is to improve our monitoring capabilities and understanding of lake ice thermodynamic processes in response to climate conditions on two large lakes in northern Canada: Great Bear Lake (GBL) and Great Slave Lake (GSL), Northwest Territories. For this purpose, ice cover retrieval algorithms were developed using Advanced

Microwave Scanning Radiometer for EOS (AMSR-E) passive microwave brightness temperature measurements. This doctoral thesis has three main objectives:

1. To develop and evaluate an algorithm for determining lake ice phenological parameters (freeze onset, ice on, melt onset, ice off, and ice duration) on GBL and GSL.

2. To develop and evaluate algorithms for estimating lake ice thickness on GBL and GSL.

3. To apply the developed retrieval algorithms for mapping the spatial and temporal patterns of lake ice phenology and ice thickness on GBL and GSL, and advancing our understanding of the response of ice cover on these two large northern lakes in response to air temperature variability.

1.2 Structure of the thesis

Chapter 2 introduces lake ice thermodynamics, remote sensing of lake ice, as well as the fundamentals and previous work on passive microwave (radiometry) of lake ice. Chapter 3 briefly describes the characteristics of GBL and GSL, and our current knowledge of the response of ice cover on these lakes to climate conditions. Chapter 4 presents the development of an ice phenology algorithm from AMSR-E brightness temperature measurements and its application to map ice cover on GBL and GSL (2002-2009). Chapter 5 describes the sensitivity of AMSR-E brightness temperature measurements to the seasonal evolution of lake ice thickness on the same lakes. As an extension of Chapter 5, Chapter 6 presents the development of ice thickness retrieval algorithms and its application to map the monthly distribution of ice thickness on GBL and GSL. Finally, Chapter 7 provides a summary of the main findings of this thesis and recommends future research directions regarding remote sensing of lake ice.

Chapter 2: Research context

2.1 Lake ice thermodynamics

Ice growth occurs between ice-on date and melt-onset as a result of an energy surplus or deficit in the energy balance (Brown et al., 2010; Jeffries et al., 2006) and, in particular, energy loss through the conductive heat flow to the atmosphere above from the underlying freshwater under the lake ice to the ice/snow boundary. The thickness and condition of the ice layer are dependent on surficial and internal ice melting (i.e. candling), surface albedo and the insulating properties of the snow cover, deformation and fracture of ice by snow load, and ice growth rates at the ice-water interface (Livingstone, 1997), as well as thermal expansion/contraction of ice. The insulating role of snow causes a high temperature gradient between the air/snow and snow/ice interface, and this controls lake ice development and ice composition owing to the lower thermal conductivity of snow (0.08-0.54 $Wm^{-2}K^{-1}$) in opposition to 2.24 $Wm^{-2}K^{-1}$ for ice (Brown et al., 2010). In addition, the presence of clouds can promote ice growth through cooling effect due to reflected solar radiation as well as warming effect by trapping emitted longwave radiation from the ice cover (Brown et al., 2010). Black ice (clear ice or congelation ice) and snow ice contribute to the thermodynamic thickening of lake ice: the former originates from freezing of water at the bottom of the ice cover. The latter is formed through refreezing of wet snow at the top of the ice cover following a slushing event, by liquid precipitation and associated water percolating through the snow to lake ice cover, or from snow precipitation incorporated into the ice during its initial formation (Brown et al., 2010; Duguay et al., 2003b; Jeffries et al., 2006).

The equilibrium between shortwave and longwave radiative fluxes at air/ice interfaces, sensible and latent heat fluxes, and the conductive heat flux through ice layers are the fundamental thermodynamics processes of lake ice (Duguay et al., 2003b; Jakkia et al., 2009; McKay et al., 1985). The latent heat flux characterizes heat transfer when phase changes (i.e. solid to liquid, or water to ice) on lake ice surface; melting process is

described as the heat exchange related to the surface melt of different types of snow/ice. Furthermore, sensible heat flux occurs when temperature changes; the conductive heat flux plays a significant role in destroying the vertical temperature profile in the subsurface and restoring thermal equilibrium in ice cover (Duguay et al., 2003b; Serreze et al., 2005). Water currents in completely ice-covered lakes, where one half of the solar radiation penetrates through the top surface while the other half is absorbed at the surface, are commonly in a laminar-turbulent transition regime (Jakkia et al., 2009). The surface energy budget (*F*) is

$$\boldsymbol{F_0 = F_{lw} - \varepsilon\sigma T_s^4(0,t) + (1-\alpha)(1-I_0)F_{sw} + F_{lat} + F_{sens}} \qquad \textbf{(2.1)}$$

where $\boldsymbol{F_{lw}}$ is the downward longwave radiative flux (W m^{-2}), and $\boldsymbol{F_{sw}}$ shows downward shortwave flux (W m^{-2}). The upward longwave radiation is calculated from $\boldsymbol{\varepsilon\sigma T_s^4}$, where $\boldsymbol{\varepsilon}$ is surface emissivity (equal to 0.99), σ is a Stefan-Boltzmann constant (5.6697×10^{-8} W m^{-2} K^{-4}), and $\boldsymbol{T_s}$ is surface temperature (in K). Otherwise, upward shortwave flux is derived from $\boldsymbol{\alpha F_{sw}}$, where $\boldsymbol{\alpha}$ is surface albedo. $\boldsymbol{I_0}$ is fraction of shortwave radiation flux that penetrates the surface, equal to 0.17 if snow depth ≤ 0.01 m, and equal to 0 if snow depth > 0.1 m. $\boldsymbol{F_{lat}}$ and $\boldsymbol{F_{sens}}$ are downward latent and sensible heat fluxes, respectively (Duguay et al., 2003b). A schematic illustration of lake ice thermodynamics, as represented in the Canadian Lake Ice Model (CLIMo), is shown in **Figure 2.1.** In lake ice models, with the exclusion of downward longwave flux, all of the expressions in Equation 2.1 are dependent, either explicitly or implicitly, on surface temperature (Duguay et al., 2003b). Changes in the direction and magnitude of these heat fluxes determine ice growth and thickening on northern lakes such as GBL and GSL, the two lakes investigated in this thesis.

Both the latent and sensible heat fluxes on GSL are higher than those of GBL; the latter being located at a more northern latitude (Rouse et al., 2009). Freeze-onset (FO) occurs when latent and sensible heat fluxes increase rapidly in the early winter season (Rouse et al., 2009). As these two heat fluxes reach zero, complete freeze over (CFO) occurs across the lake surface. In addition, conductive heat flux increases gradually from FO to CFO due to temperature gradient changes. As incoming solar radiation increases in spring on both

lakes (GSL first) the latent heat flux gradually increases from melt-onset (MO) and continues to increase until the complete disappearance of ice. The sensible heat flux increases negatively from MO to ice-off dates (Rouse et al., 2009).

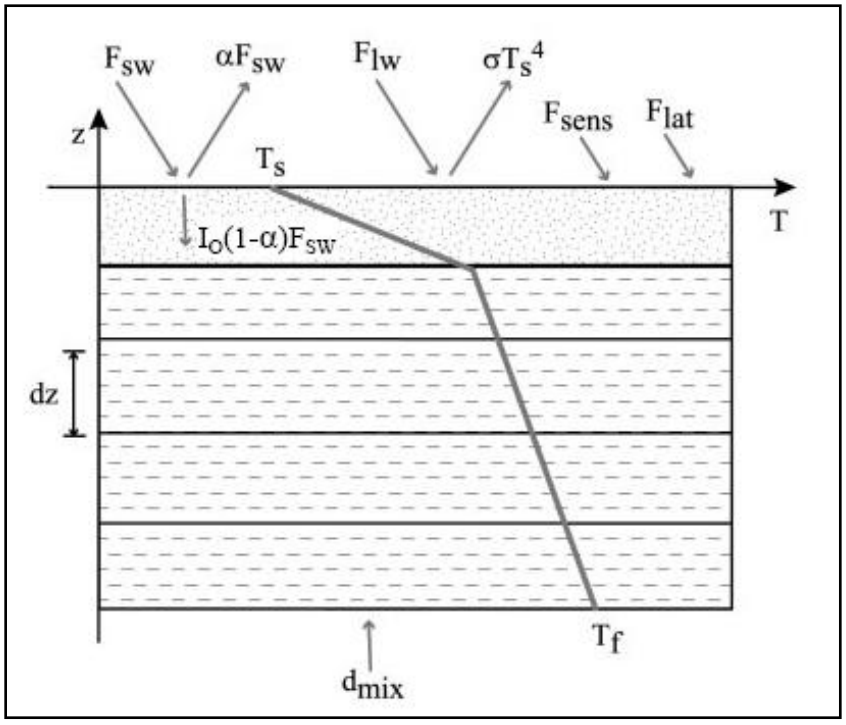

Figure 2.1: Schematic illustration of lake ice thermodynamics during the ice season (Duguay et al., 2003b). The layers with dots and with dashed lines point to snow and ice with depth (dz), respectively. The thick grey line represents the temperature profile from the surface temperature (T_s) on lake ice surface to the freezing temperature of fresh water (T_f).

2.2 Remote sensing of lake ice

2.2.1 Optical remote sensing

Optical remote sensing instruments offer more limited potential for the retrieval of ice phenological information over lakes compared to microwave systems due to their sensitivity to the presence of clouds, polar darkness and generally lower temporal resolution. Spaceborne optical sensors such as LANDSAT-Multispectral Scanner (MSS), National Oceanic and Atmospheric Administration (NOAA)–Advanced Very High

Resolution Radiometer (AVHRR), Operational Linescan System (OLS) on Defense Meteorological Satellites Program (DMSP) have been used in a few studies for detecting ice formation, freeze-up/break-up dates, and ice type classification on the Great Lakes (Wiesnet, 1979; Leshkevich et al., 1985; 1988) and northern European lakes (Maslanik et al., 1987; Skorve et al., 1987). Satellite-derived ice phenological dates from AVHRR have also been utilized to improve ground observations, which are more spatially limited (Wynne et al., 1993; 1996).

Ice break-up dates have been extracted recently with some degree of success from a long time series of NOAA-AVHRR data (1985-2004) for selected lakes across Canada (Latifovic et al., 2007). MODIS (Moderate-resolution Imaging Spectroradiometer) and ASTER (Advanced Spaceborne Thermal Emission and Reflection Radiometer) derived snow/ice surface temperature have also been identified as useful for learning about land surface processes and the influencing local climate (Hall et al., 2008). Finally, MODIS visible and near-infrared data have been used for the verification of lake ice cover parameters derived from active and passive microwave sensors under clear-sky conditions (Howell et al., 2009a; Kouraev et al., 2007a).

2.2.2 Active microwave remote sensing

Active microwave satellite sensors offer an advantage over optical satellite sensors; they provide data regardless of cloud presence and polar darkness, and, therefore, are of particular interest for monitoring of lake ice cover. In this respect, several studies have shown the potential of airborne/spaceborne radar (altimetry, scatterometry, but with emphasis on synthetic aperture radar or SAR) for lake ice investigations (Sellmann et al., 1975; Elachi et al., 1976; Weeks et al., 1977, 1978, 1981; Swift et al., 1980; Mellor et al., 1982; Leconte et al., 1991; Weydahl 1993; Hall et al., 1994; Jeffries et al., 1994, 1996; Morris et al., 1995; Duguay et al., 2002, 2003a; Kouraev et al., 2007a; Howell et al., 2009a). SAR data has been shown to be useful for detecting freeze-up dates (Hall et al., 1994). A number of radar-based studies have been carried out to monitor ice formation and growth,

floating and grounded lake ice, and the ice decay process near Churchill, Manitoba (Duguay et al., 1997, 1999, 2002, 2003a), the North Slope of Alaska (Jeffries et al., 1994, 1996; Morris et al., 1995; Kozlenko et al., 2000; White et al., 2008), on a large, deep Siberian lake (El′gygytgyn) (Nolan et al., 2003), on shallow lakes of the N.W.T. (Hirose et al., 2008), as well as on GBL and GSL (Howell et al., 2009a), in addition to ice type classification (Leshkevich et al., 2007; Nghiem et al., 2007). One disadvantage of the use of SAR from current satellites is that data can only be acquired in one imaging mode (higher or lower spatial resolution) at a time and in some cases the data is not free-of-charge. The latter has been a major impediment to the operational use of RADARSAT data for lake ice monitoring in Canada.

2.2.3 Passive microwave remote sensing

Similar to active microwave satellite sensors, passive microwave systems can also provide data independent of the presence of clouds and polar darkness, and with frequent and large area coverage acquisitions (more than once daily). Although data from microwave radiometers are acquired at spatial resolutions in the order of tens of kilometres, the frequency range at which these systems operate (circa 6-89 GHz) makes this technology particularly interesting for operational lake ice monitoring on the very largest lakes of the Northern Hemisphere.

2.2.3.1 Radiometry of lake ice

2.2.3.1.1 Microwave dielectric properties of freshwater ice

A term used in the literature is the *relaxation frequency (f_0),* where

$$f_0 = (2\pi\tau)^{-1} \qquad (2.2)$$

The relaxation frequency of pure water (f_{w0}) is placed in the microwave regions; for example, f_{w0} at 0 °C and at 20 °C are approximately 9 and 17 GHz, respectively (Ulaby et al., 1986). The upper panel of **Figure 2.2** shows the relaxation frequency behavior of ϵ'_w

water at 0 °C and 20 °C. These relaxation frequencies are influenced by molecular dipole in water (H_3O^+).

Unlike liquid water, whose relaxation frequency is placed in the microwave region, the relaxation of pure ice takes place in the kilohertz region. The relaxation frequency (f_{i0}) in freshwater ice is equal to 7.23 kHz at 0 °C, and reduces with negative temperature to 3.5 Hz at - 66 °C (Ulaby et al., 1986). Freshwater ice (ϵ_i') is often assigned a constant value (3.15) because experimental evidence shows that the permittivity of ice is close to being independent of both temperature and frequency in the microwave region (Ulaby et al., 1986). The loss factor of ice (ϵ_i''), however, exhibits strong variations with both frequency and temperature. The range of values of ϵ_i'' at frequencies from 10^7 to 2×10^{11} Hz and temperatures from 190 to 265 K, in the bottom panel of **Figure 2.2,** indicates that ϵ_i'' changes slope at about 1 GHz and then begins to increase with increasing frequency.

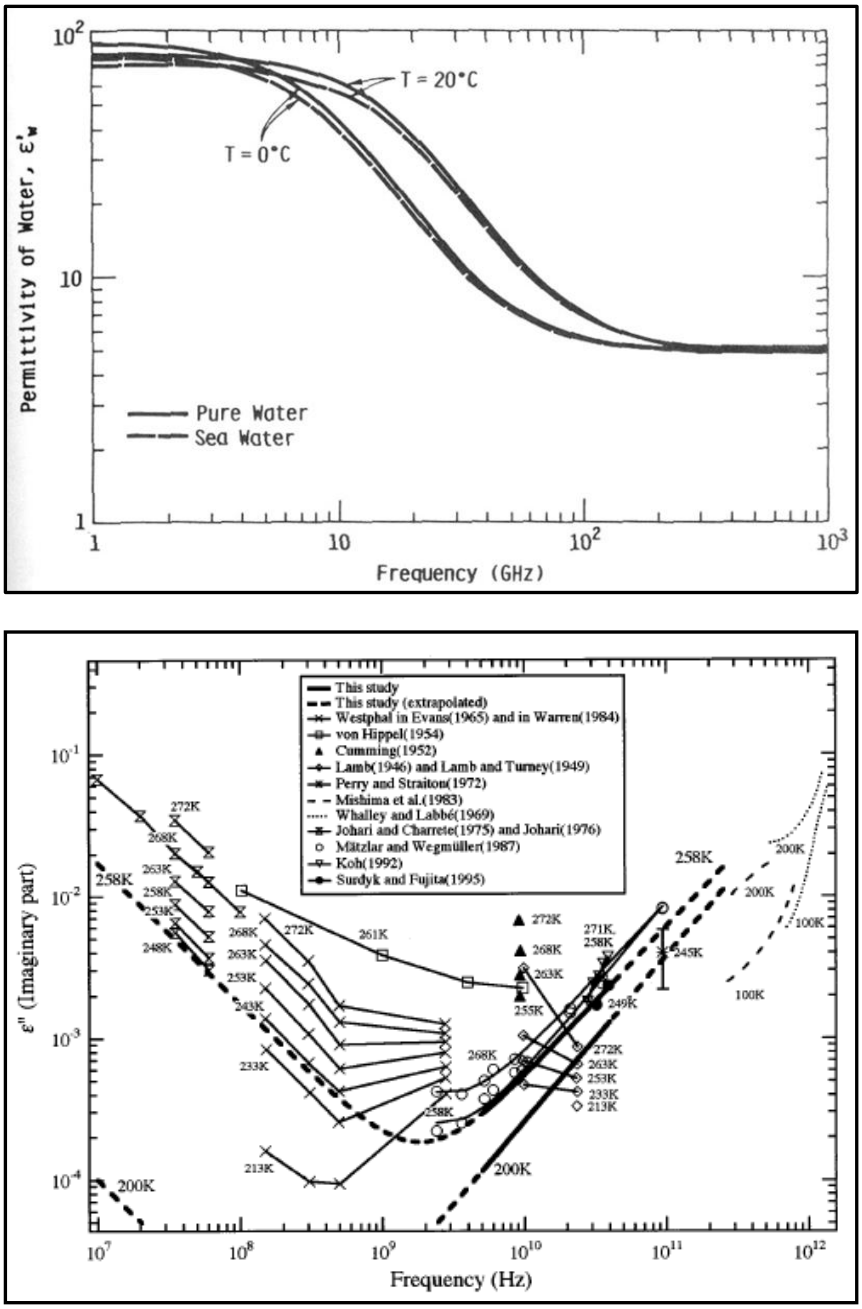

Figure 2.2: Plots of real parts of the complex dielectric constant of pure water at 0 °C and at 20 °C (upper, Ulaby et al., 1986), and loss factor of pure- and fresh-water ice against frequency at various temperatures (bottom, Matsuoka et al., 1996).

2.2.3.1.2 Emissivity, penetration depth, and brightness temperature

The dielectric constant (ε) and refractive index (*n*) are the physical properties of a material and are given by

$$\varepsilon = \varepsilon' - j\varepsilon'' \qquad n = n' - jn'' \tag{2.3}$$

where ε'(*n*') and ε"(*n*") are the real and imaginary parts of the dielectric constant (refractive index) (Mätzler et al., 1987). Permittivity describes what happens with electromagnetic energy when it impinges upon a boundary, and loss describes the electromagnetic loss once energy has penetrated the material (Ulaby et al., 1986). This total loss is a combination of the absorption loss (i.e., the transformation of energy into another form) and scattering loss (energy deflected to travel in directions other than that of incident) (Ulaby et al., 1986). For non-magnetic materials such as ice, a simple formula is applied:

$$\varepsilon' = n' \qquad \varepsilon'' = 2n'n'' \tag{2.4}$$

The real parts are approximately constant (ε' = 3.17, *n*' = 1.78) over a large frequency range (from 10 MHz to 1000 GHz) with a very slight temperature dependence (Mätzler et al., 1987). The penetration depth (*p*) at which the energy transmitted across the boundary penetrates a medium can be expressed as:

$$p = \frac{\lambda_0}{4\pi n''} = \frac{\lambda_0 \sqrt{\varepsilon'}}{2\pi\varepsilon''} \tag{2.5}$$

where λ is wavelength in metres (Mätzler et al., 1987). The penetration depth (*p)* is dependent of frequency and temperature at fixed incident angles (Table 2.1).

Table 2.1. Microwave penetration depth (m) in freshwater ice as a function of temperature and frequency

	Penetration Depth (m)				Reference
	6.6 GHz	10.7 GHz	18 GHz	37 GHz	
190.00 K	58.00	20.00	6.60	1.40	*Surdyk*,2002
230.00 K	34.00	12.00	4.20	0.90	
265.00 K	19.00	8.00	2.80	0.70	
253.15 K			4.42	0.81	*Chang et al.*, 1997
		10 GHz		30 GHz	
258.15 K		6.50		0.79	*Rees*, 2006
268.15 K		4.30		0.63	

The upwelling radiation observed as the apparent temperature at a spaceborne passive microwave radiometer (T_B) can be expressed as

$$T_B = (RT_{sky} + (1-R)T_{surf})e^{-\tau} + T_{atm} \quad \textbf{(2.6)}$$

where $e^{-\tau}$ is the atmospheric transmissivity; R is the surface reflectivity; T_{sky} is the sky radiation; T_{surf} is the surface emission, and T_{atm} is the atmospheric component (Kelly, 2009). In most cases, T_{atm} and T_{sky} are neglected because they are only small amounts. Thus, T_B is directly related to surface conditions, and if microwave atmospheric windows are used, atmospheric transmissivity is maximized (~1) (Kelly, 2009). The frequency-dependent surface emission is a function of physical temperature and surface emissivity of lake ice and the overlying snow cover. Thus, T_B from a passive microwave sensor is defined as the product of the emissivity (ε) and physical temperature (T_{kin}) by Ulaby et al. (1986):

$$T_B = \varepsilon T_{kin} \quad \textbf{(2.7)}$$

The emissivity is a ratio of the radiant energy of an object to that of a black body at the same temperature. Since emissivity has a range between 0 and 1, the T_B is lower than the real kinetic temperature. Passive microwave systems, regardless of cloud coverage and darkness, can measure naturally emitted radiation by T_B, which consists of the product of real physical temperature (T_{kin}) and the emissivity (ε) of the object (equation 2.7). In contrast to the high-loss characteristics of sea ice (due to salinity), one of the major microwave characteristics of pure ice (or freshwater ice) is its low-loss transmission behavior.

The discrimination of ice characteristics using passive microwave technique requires a good knowledge of the radiometric properties of ice in nature (Kouraev et al., 2007a). One complicating factor pertaining to downward-looking radiometric observations of lake ice is that the surface of the ice is often overlain by snow cover, which modifies the radiative transfer problem, resulting in a reduction in radiometric sensitivity to the variation in ice-thickness. Such a reduction in sensitivity is dependent on the snow depth (or density), wetness of surface conditions, and microwave frequency (Ulaby et al, 1986).

2.2.3.2 Previous work

T_Bs measured by airborne and spaceborne passive microwave systems have shown to be sensitive to the presence/absence of ice on lakes (Gloersen, 1973; Melloh et al., 1990; Barry et al., 1993; Walker et al., 1993; Pilant, 1995; Kouraev et al., 2007a) and ice thickness (Swift et al., 1980; Hall et al., 1981, 1993; Chang et al., 1997). Early airborne passive microwave measurement campaigns concurrent with limited in-situ observations from the Walden Reservoir, Colorado showed a strong relation between T_B and ice thickness at frequencies between about 5 and 22 GHz (Hall et al., 1981). In particular, a higher sensitivity of T_B to ice thickness was found at 5 GHz. A study by Hall (1993) also suggested that the frequencies of the Special Sensor Microwave/Imager (SSM/I) onboard of DMSP were not well-suited to studying lake ice thickness, but were suitable for monitoring ice growth and decay processes on large lakes, albeit the larger footprint of SSM/I at mid frequencies (18-37 GHz).

Work in the Climate Research Division at Environment Canada (CRD-EC) focused for several years on assembling a historical time series of ice freeze-up and break-up dates (corresponding to complete freeze over and ice-free conditions) over GSL through visual interpretation of SSM/I 85 GHz images (Schertzer et al., 2008; Walker et al., 1993; 2000). Determined ice break-up and freeze-up dates, and corresponding ice-free days are shown in **Figure 2.3.** Based on a composite of ice breakup and freeze-up dates from 1988 to 2003, the central basin of GSL is expected to be ice-free by DY 168 (June 17) on average and ice freeze-over is expected by DY 342 (December 8), and with an average ice-free duration of 174 days (Schertzer et al., 2008; Walker et al., 1999). The 85 GHz SSM/I frequency (H- and V-pol) channels yield considerably higher resolution than the other SSM/I channels (about 15 km, with sampling distance of 12.5 km). However, the atmosphere is far more opaque at 85 GHz compared to 19 and 37 GHz, and can cause severe biases for data obtained at 85 GHz, particularly in cloud-covered areas which are prevalent during fall/early winter freeze-up in northern Canada.

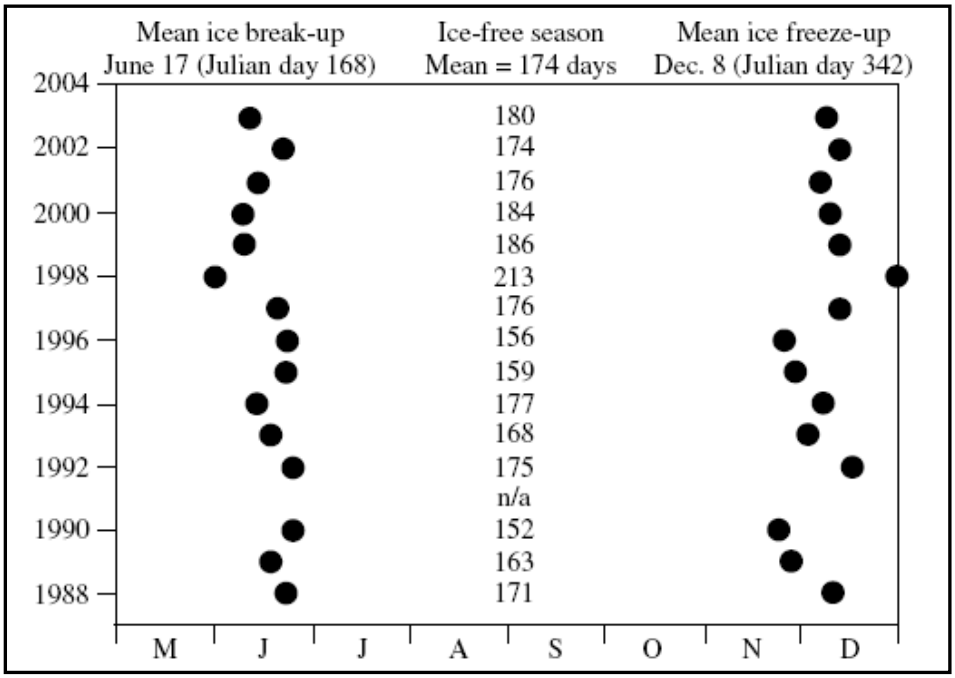

Figure 2.3: Lake ice break-up and freeze-up dates, and corresponding ice-free seasons for 1988-2003 period in the central basin of GSL as determined from the visual interpretation of 85 GHz SSM/I images (Schertzer et al., 2003; Walker et al., 1999).

Recently, Kouraev et al. (2007ab) showed that the combination of data from satellite altimetric and radiometric missions provide a significant potential for discriminating seasonal/regional ice phenological events on Lake Baikal, which has a large surface area and with complicated hydrological and weather regimes in its various sub-regions. A wide range of existing satellite radar altimetry (i.e. TOPEX/Poseidon, Jason-1, ENVISAT and Geosat Follow-On) and spaceborne radiometry data (i.e. SSM/I) was used to demonstrate applicability for lake ice/freshwater discrimination, and to determine the timing of freeze-up and break-up (FO, ice-on, MO, and ice-off dates) on the lake (Kouraev et al., 2007a). The justification for the combination of altimetry and radiometry measurements is as follows. First, the longitudinal (narrow) shape of Lake Baikal makes the use of SSM/I alone somewhat limitative due to land contamination along lakeshore within of its large footprint. Second, altimetry data does not provide extra ice information when large lake areas are completely frozen, or when the whole lake changes simultaneously during the rapid freeze-up or break-up transition periods.

Figure 2.4 illustrates that radar altimeter backscatter acquired at Ku-band (13.6 GHz) and passive microwave T_B measurements obtained at 18.7 and 37.0 GHz enhance the capabilities of microwave measurements for lake ice studies. Observations from these two types of satellite sensors provide particular advantages: 1) broad spatial coverage and good temporal resolution for SSM/I sensor; and 2) high radiometric sensitivity and along-track finer spatial resolution of altimetric measurements during ice formation, ice growth and decay periods (Kouraev et al., 2007a).

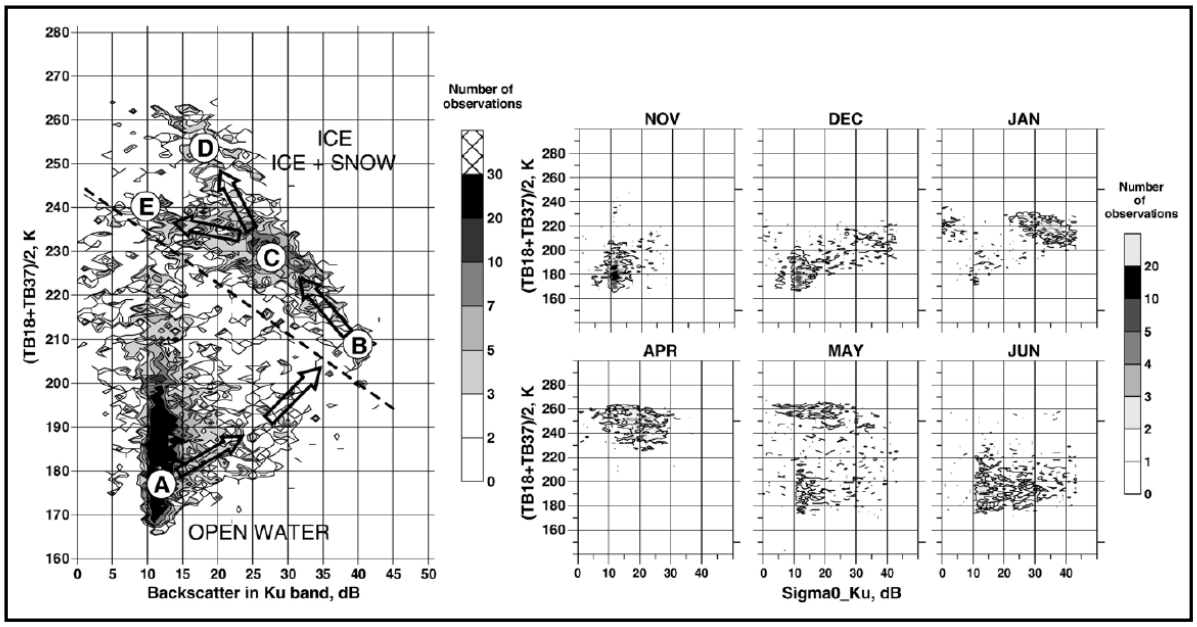

Figure 2.4: Two-dimensional histograms between average brightness temperature at 18 and 37 GHz in SSM/I, and backscatter coefficient at Ku-band (13.6 GHz) of TOPEX/Poseidon. Two main classes (open water and ice cover) and boundary (dashed line) are shown on the left panel. Arrows indicate the temporal evolution from open water (A) to freeze-onset (B) to complete freeze over (C), and then to snow accumulation, ice ageing and decay (D and E) (Kouraev et al., 2007a).

The work described thus far in section 2.2 relates to research-oriented investigations that have largely focused on demonstrating the potential of various satellite sensors to determine one or a few lake ice cover parameters. There are, however, a number of operational satellite products we are aware of that either use optical data alone or in combination with microwave data, mostly through visual interpretation, to monitor snow/lake ice cover. These are presented next. Both the previous work reviewed above and the survey of existing operational products will help to better place the main contributions of this thesis in the area of ice cover mapping/monitoring from satellite remote sensing.

2.2.4 Operational products

MODIS snow products: Earth Observation System (EOS) MODIS data from the Terra and Aqua satellite platforms are used to generate composites of daily global snow-cover products from the automated SNOWMAP algorithm, which provides ice cover information at 500-m spatial resolution in all inland water bodies (mainly medium-size to large lakes). The snow-mapping algorithm makes use of a grouped-criteria technique using the Normalized Difference Snow Index (NDSI) with the NDSI = (band 4 – band 6)/(band 4 + band 6) in MODIS, and other spectral threshold tests to identify snow on a pixel-by pixel basis as snow has a strong reflectance in the visible (band 4: (0.545-0.565 μm) and strong shortwave absorption characteristics in the mid-infrared (IR) (band 6: 1.628-1.652 μm) (Hall et al., 2001). However, clouds are highly variable and may be detected by their generally high reflectance in the visible and near-IR parts of the electromagnetic spectrum. Derived from the land/water mask, pixels on inland water bodies are calculated from same SNOWMAP algorithm as applied on land. Recently, new MODIS Cloud-Gap-Filled snow-cover products by data assimilation technique are developed (Hall et al., 2010). Although the MODIS SNOWMAP product has not been validated yet over lakes, the algorithm is known to be able to detect snow-covered lake ice. Pixels over bare clear (black) ice, however, may be incorrectly labelled as open water pixels since reflectance in band 4 will be lower than that of snow-covered lake ice, and therefore may result in a NDSI threshold value lower than 0.4 set as the minimum to detect snow.

NOAA IMS Daily Snow and Ice 4 km/24 km products: The National Oceanic and Atmospheric Administration/National Environmental Satellite, Data, and Information Service (NOAA/NESDIS) creates Interactive Multisensor Snow and Ice Mapping System (IMS, http://www.natice.noaa.gov/ims/) daily 4-km resolution (6144 × 6144) and 24-km resolution (1024 × 1024) grid products with four different categories: water, land, snow, and ice (Helfrich et al., 2007). The IMS products integrate an extensive variety of satellite imagery (AVHRR, Geostationary Operational Environmental Satellite (GOES), and Special Sensor Microwave/Imager (SSM/I)), mapped products (USAF Snow/Ice Analysis, and the Advanced Microwave Sounding Unit (AMSU)) and ground observations for the improvement in the output resolutions (Key et al., 2007). Ice cover analysis relies on a different approach than snow cover for mapping. Ice cover determination depends less on high albedo, stagnate cover, and meteorological conditions (Helfrich et al., 2007). The presence of lake ice, however, can be unrelated to current meteorological conditions due to ice cover movement (dynamics), ice thickness, and water temperature among other factors. The 24- km (1997-present) and the 4-km (2004-present) IMS grid products provide ice extent/fraction information for all resolvable lakes at these resolutions. However, neither of these products has been validated or compared to date against other satellite-derived products.

Canadian Ice Service lake-ice product: Ice analysts at the Canadian Ice Service (CIS) estimate lake ice cover fraction in tenths (0: open water – 10: complete ice cover) for nearly 140 lakes across Canada/northern US, including GBL and GSL, on a weekly basis from visual interpretation of NOAA AVHRR 1.1 km and RADARSAT ScanSAR 100 m imagery (Howell et al., 2009a). CIS generates this product as a single lake-wide value per lake (text file) to support operational requirements for numerical weather forecasting by the Canadian Meteorological Centre (CMC) (Key et al., 2007). Complete freeze over (CFO) dates can be determined from the CIS file when the ice fraction on a lake changes from 9 to 10. Water clear of ice (WCI) dates can be derived when the ice fraction passes from 1 to 0. CFO and WCI derived dates can be estimated with about a one-week accuracy due to the weekly

nature of the product (Howell et al., 2009a). The accuracy of the information in the lake-ice fraction file provided by CIS is influenced not only by the amount of cloud cover over a particular lake in AVHRR imagery but also by the number of RADARSAT images acquired during the week.

Great Lakes ice charts: Great Lakes synoptic ice charts are produced from the interpretation of a blend of observations from lakeshore, vessel, aircraft-based visual observations, and spaceborne- remote sensing measurements that cover the entire area of all five Great Lakes of southern Canada/northern US. Their production started in the 1970s, with the latest satellite technology being integrated over the years in the interpretation process (Assel et al., 2003; Key et al., 2007). Ice analysis charts provide information on estimated daily/weekly ice cover conditions (i.e. ice type, stage of development, and ice formation) from December to April every winter seasons by using the Egg Code format of the World Meteorological Organization (WMO). These ice charts products are available on the Canadian Ice Service (CIS) website as the Great Lakes regional area at http://www.ec.gc.ca/glaces-ice/default.asp.

2.3 Summary

In this chapter, basic principles of ice thermodynamics and previous lake ice research and operational products derived at a wide range of wavelengths were reviewed. The main limitation of lake ice products derived from optical satellite sensors is that they are influenced by polar darkness and persistent periods of cloud cover at high latitudes such as the GBL and GSL regions, particularly during the late fall/early-winter freeze-up period. Cloud cover remains somewhat of a problem during the spring break-up period as well. Also, optical sensors are still influenced by polar darkness for some time during the ice growth season, and the wavelengths at which these sensors operate do not permit to estimate ice thickness. Both active and passive microwave sensors are more suitable for estimating ice thickness and determining all ice phenological parameters (ice onset, ice on, melt onset, ice off, ice duration) since they operate at wavelengths sensitive to ice growth

and largely unaffected by cloud cover and by polar darkness. Active microwave satellite systems are an attractive technology for estimating ice phenological parameters and thickness because they can acquire data at high spatial resolution (about 3-100 m range). However, most past and current satellites (ERS-1/2, RADARSAT-1/2, TerraSAR-X) do not provide the large swath and revisit cycle needed to determine these parameters over large lakes, such as GBL and GSL, at the temporal resolution required by the weather forecasting and climate communities (e.g. every 1-2 days). Satellite passive microwave systems, on the other hand, provide the large swath and adequate revisit time (more than once daily) for monitoring ice phenology and thickness on the largest lakes of the northern hemisphere. Although the coarse spatial resolution of such systems (e.g. SSM/I, tens of kilometres footprints) has been a limiting factor to the development of ice cover retrieval algorithms, due to land contamination problems along lakeshores, some improvements have been made. Since 2002, NASA's Aqua satellite has been operating the AMSR-E passive microwave radiometer which can acquire data at resolutions two to three times better than SSM/I. Surprisingly, to our knowledge, no previous investigation has examined the potential of AMSR-E for retrieving lake ice phenology and thickness. Therefore, the main contribution of this thesis is the development and application of new, novel, algorithms for determination of lake ice cover parameters on two of the largest lakes of the northern hemisphere, GBL and GSL.

Chapter 3: Study area

Great Slave Lake and Great Bear Lake are, respectively, the 10th and 8th world largest freshwater lakes. Both lakes are also known as the Mackenzie Great Lakes, being located in the Mackenzie River Basin (MRB), within two physiographic regions of Canada's Northwest Territories (NWT): the Precambrian Shield and the Interior Plains (**Figure 3.1**). The eastern parts of both lakes are situated in the Precambrian Shield. Its undulating topography with bedrock outcrops causes the formation of rounded hills and valleys. In addition, widespread discontinuous permafrost exists in surrounding lakes, but sporadic discontinuous permafrost is found in the west of GSL (French et al., 1993). The high topography of the western Cordillera, and low relief of the central and eastern parts of the Mackenzie Basin strongly influence the regional climate (e.g. atmospheric circulation pattern and the advective heat and moisture fluxes) (Woo et al., 2008). Most of GBL and the western and central parts of GSL are located in the flat-lying Interior Plains and underlain by thick glacial, fluvial, and lacustrine deposits; in addition, the Plains are dotted with numerous wetlands and lakes (Woo et al., 2008).

GSL and GBL lie between 60° to 67° N and between 109° to 126° W (**Figure 3.1**), and with surface areas of 286,000 km^2 and 313,000 km^2, and average depths of 88 m and 76 m, respectively (Rouse et al., 2008b; Woo et al., 2008). Both lakes experience very short nighttime periods in summer and equally long ones in winter. The different hydrological systems and energy balance of GBL and GSL result in distinct thermodynamic, hydrodynamic, and surface climatic cycles. In general, for both lakes, early ice break-up is accompanied by later freeze-up and late ice break-up by early freeze-up (Rouse et al., 2008a). The relation between the timing of lake ice break-up and the amount of the absorbed solar radiation, which delays freeze-up makes the two large lakes very sensitive to climatic variability (Rouse et al., 2008a). The lakes have regional annual air temperatures within 2 °C of each other, but GSL shows a longer open-water period with higher water temperatures than its counterpart, GBL (Rouse et al., 2008a).

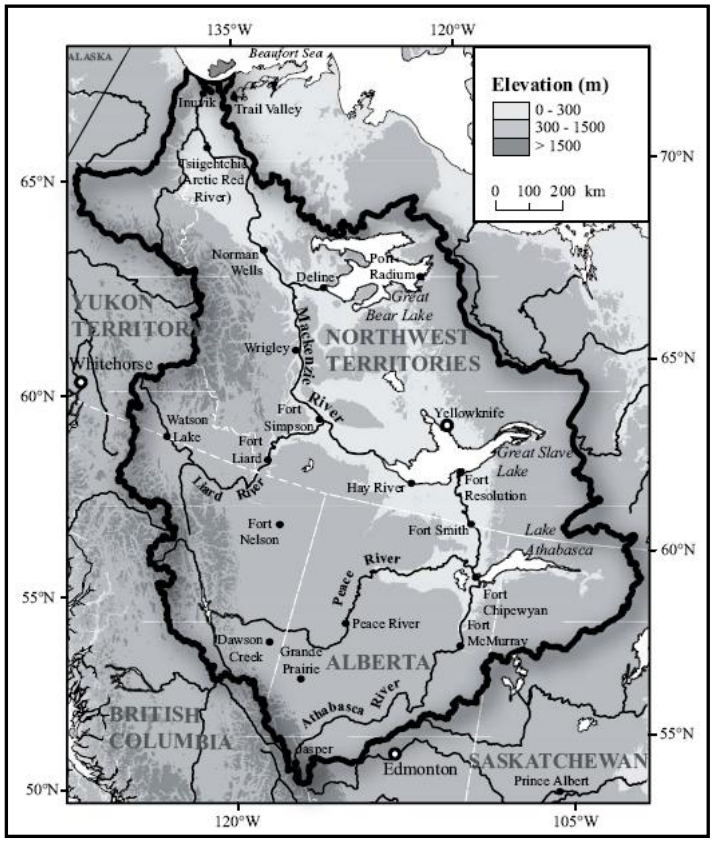

Figure 3.1: Map of the Mackenzie River basin and the locations of Great Bear Lake and Great Slave Lake (Rouse et al., 2008a; Woo et al., 2008).

3.1 Great Slave Lake

3.1.1 Physical characteristics

Great Slave Lake is part of the north-flowing river system in the Mackenzie Basin (Rouse et al., 2008a). The outflow of GSL into the Mackenzie River is more than eight times that from GBL as incoming freshwater from the south via the Slave River provides 82 percent of this water volume (Rouse et al., 2008a). GSL has a mean depth in the main basin of 41 m (maximum depth of 163 m) while the eastern arm of GSL is much deeper with a mean depth of 249 m and a maximum depth of 614 m (**Figure 3.2**) (Howell et al., 2009a).

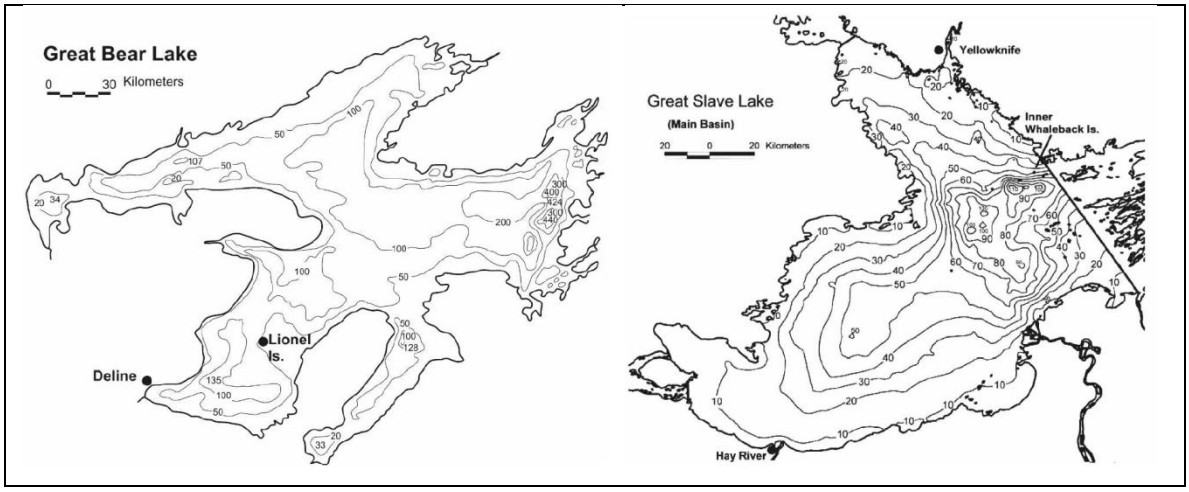

Figure 3.2: Bathymetry of Great Bear Lake (left) and Great Slave Lake with the location of Deline, Yellowknife, and Hay River (right). Depth contours are in meter (Rouse et al., 2008a).

3.1.2 Regional climate

The high spatiotemporal variability in near-surface air temperature and wind speed over GSL influences the surface water temperature and lake heat flux exchange (Rouse et al., 2008a; Schertzer et al., 2008). Annual and seasonal air temperature anomalies from the Yellowknife (1943-2009) and Hay River (1944-2009) weather stations, which are located on opposite sides of GSL, are shown in **Figures 3.3 and 3.4.** Over the last six and a half decades or so, annual air temperature in the region has significantly increased at a rate of 0.31 ^{o}C per decade or 2 °C over the full period at both stations. Annual snowfall (average of 17-18 cm over the same period) has also significantly increased by about 1.4 cm per decade or about 9 cm (1943-2009). Seasonally, in order of magnitude, winter (DJF) air temperature has increased more rapidly (4-5 ^{o}C), followed by spring (MAM) (about 2 ^{o}C) and then summer (JJA) (about 1 ^{o}C). Fall (SON) also shows an increase in temperature at the two stations (0.2-0.6 ^{o}C), but the trends are not significant. Placing the period of analysis of AMSR-E data (2002-2009) into the longer historical context, as illustrated in **Figures 3.3 and 3.4**, permits to see that winters and to a lesser extent springs have been becoming especially warmer over the last 30-40 years. Interestingly, the occurrence of "cold years" is also less frequent in winter and in fall since the mid-1990s.

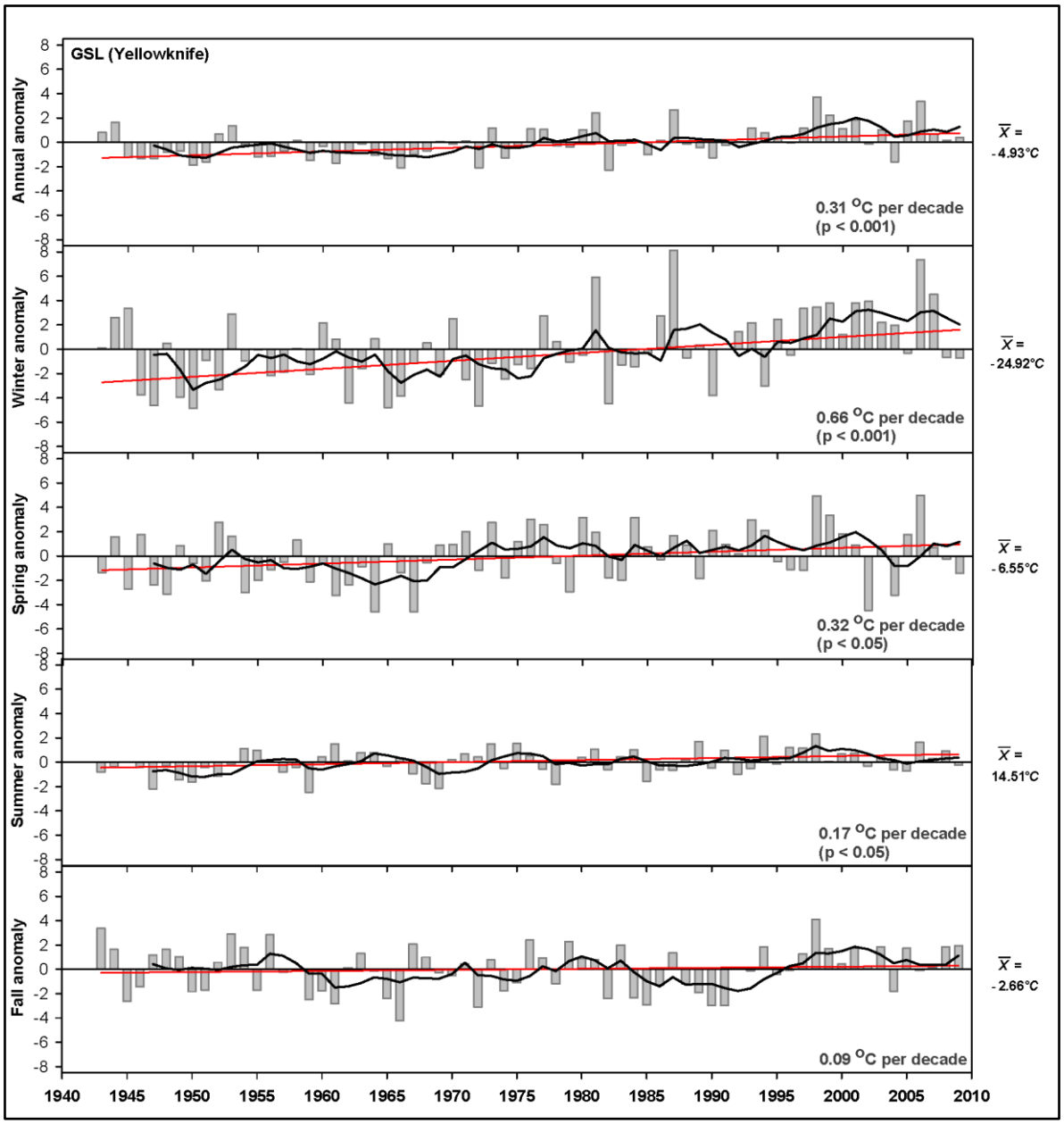

Figure 3.3: Annual and seasonal mean air temperature (°C) for winter (DJF), spring (MAM), summer (JJA), and autumn (SON) at Yellowknife meteorological station (1943-2009). Black line represents 5-year running mean. Mean air temperatures are provided as a reference on the right hand side of the graphs.

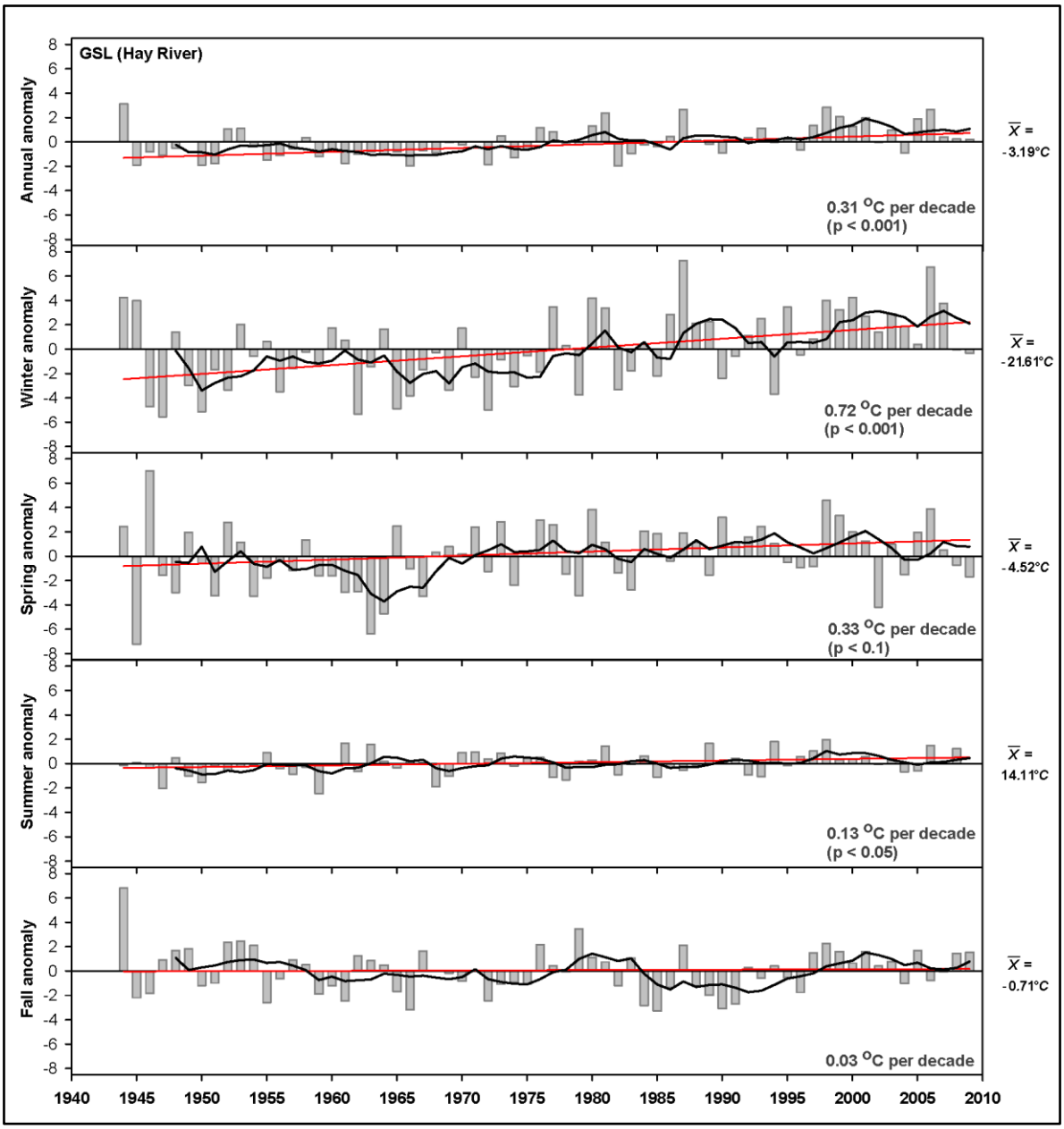

Figure 3.4: Annual and seasonal mean air temperature (°C) for winter (DJF), spring (MAM), summer (JJA), and autumn (SON) at Hay River meteorological station (1944-2009). Black line represents 5-year running mean. Mean air temperatures are provided as a reference on the right hand side of the graphs.

3.1.3 Ice cover conditions

GSL is ice-free from the beginning of June until mid- to late-December; however, ice conditions on the lake have been documented to vary significantly from year to year (Blanken et al., 2008). GSL generally reaches ice-free conditions by the end of June. This large lake experiences break-up dates close to a month in advance of GBL (Rouse et al., 2009c). The hydrological system of GSL causes distinct thermodynamics and hydrodynamic process, influencing the timing and duration of the freeze-up and break-up processes. The discharge of Slave River into GSL has an important influence on the ice break-up process by melting the ice faster than if there was no major freshwater inflow (left, **Figure 3.5**). Water circulation in the lake can also have an impact on the spatial variability of ice phenological events (right, **Figure 3.5**).

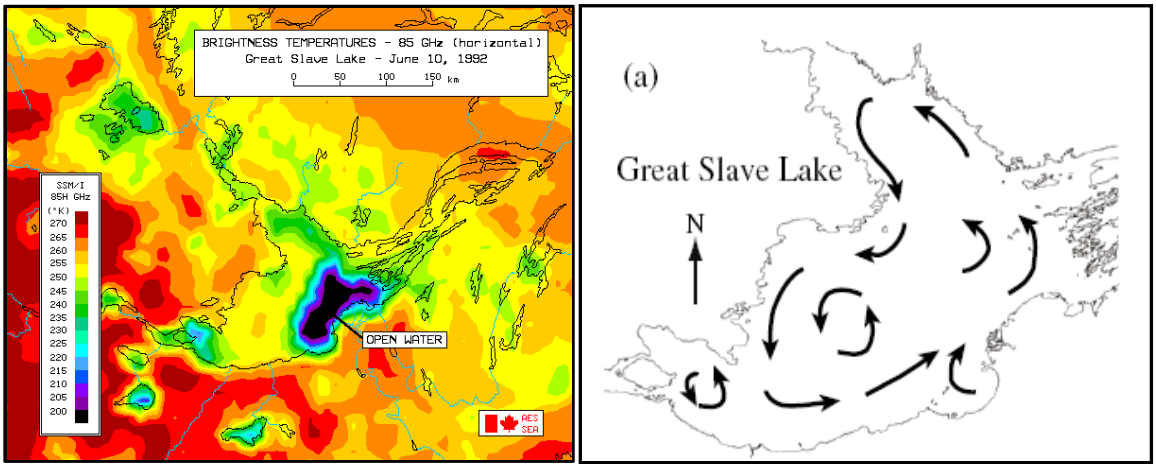

Figure 3.5: Great Slave Lake on June 10, 1992 (Image courtesy of Anne Walker at the CRYSYS Lake Ice Research Program) (left), and generalized dominant circulation pattern for the upper layer of Great Slave Lake based on ELCOM 3-D hydrodynamic model simulation (right) (Rouse et al., 2008d).

The Environment Canada (2010) ice cover database provides weekly ice thickness measurements (1958-2010) in Back Bay near Yellowknife and ice phenology dates (1956-1996) are available from the Canadian Ice Database (Lenormand et al., 2002), with the exception of some missing ice thickness (May 1996 to November 2002) and freeze-up

observations (1982-1984, 1993, 1995). According to Ménard et al. (2002), the average maximum in-situ ice thickness at 10 m depth in Back Bay (1960-1991) was 1.33 ± 0.19 m. Also, in-situ observations reveal that on average ice-on and ice-off dates in this bay occurred on Day of Year (DY) 302 and DY 152, respectively, during the period 1956-1996. As shown earlier in Chapter 2 (see **Figure 2.3**), the average (1988-2003) complete freeze-over (CFO) date detected by SSM/I 85 GHz in the main basin of GSL was reported to be DY 342 and water clear-of-ice (WCI) DY 168, which gives an open water duration of 174 days (Schertzer et al., 2008; Walker et al., 1999). In another study, from visual interpretation of 37 GHz SSM/I T_B time series (1979-2005), Rouse et al. (2008c) report average dates of CFO and WCI for this basin to be on DY 349 and DY 165.

3.2 Great Bear Lake

3.2.1 Physical characteristics

Great Bear Lake (GBL) is the largest lake of northern Canada. The northern extent of GBL is intersected by the Arctic Circle (66.5° N). GBL is affected by colder temperatures than its more southern counterpart, GSL (Rouse et al., 2008a). The lake has a mean depth of 76 m and a maximum depth of 446 m. It flows into the Mackenzie River via the Great Bear River (**Figure 3.2**) (Howell et al., 2009a). GBL has the characteristics of a polar lake: a single period of circulation at a temperature close to 4 °C in summer; high oxygen values at all times of the year with supersaturation in the summer surface waters and below the ice during winter; and a high oxygen content of the bottom waters in April (Johnson, 1975). Even though GBL has been described as cold monomictic with no vertical convective mixing, and thus, complete water turnover does not occur annually (Bursa et al., 1967), recent evidence indicates that this is not the case, at least in some parts of the lake (Rouse et al., 2008b). Unlike GSL, GBL is hydrologically isolated in its own relatively small drainage basin and all of its inflow and outflow derived from its immediate watershed (Rouse et al., 2008a).

3.2.2 Regional climate

The historical climate record of the GBL region is very short, since 1992 only. Therefore, in contrast to the GSL region, too few years are available to determine any air temperature trend and put 2002-2009 (AMSR-E) into a long historical context. Annual and seasonal air temperatures from winter to fall at the Deline (1992-2009) weather station, located on the southwest shore of GBL, are illustrated in **Figure 3.6.** The average annual temperature is about two degrees colder (at -6.0 °C) than at GSL and snowfall averages about the same (17-19 cm) in the two regions over the same period (1992-2009). The average winter air temperature at Deline (1992-2009) is -23.6 °C (-26.3 to -20.0 °C). Average spring and summer air temperatures (1992-2009) are -7.7 °C (-11.3 to 4.4 °C) and 11.6 °C (10.1 to 13.3 °C), respectively. Average fall temperature is -4.6 °C (-7.5 to -2.1 °C).

3.2.3 Ice cover conditions

Much less is known about ice cover conditions on GBL, compared to GSL. Ice-free conditions are only reached in general by the middle of July. Lake ice thickness has been reported to be in the order of 2 m by the end of winter in 1967 (Bursa et al., 1967). A recent study indicates that ice thickness reached only 1.37 m and 0.885 m on GBL in March 2004 and 2005, respectively (Woo et al., 2007). The CFO and WCI dates for main section of GBL were determined to occur on DY 330 and DY 194, respectively, through visual interpretation of 37 GHz SSM/I data from 1979-2005 (Rouse et al., 2008a).

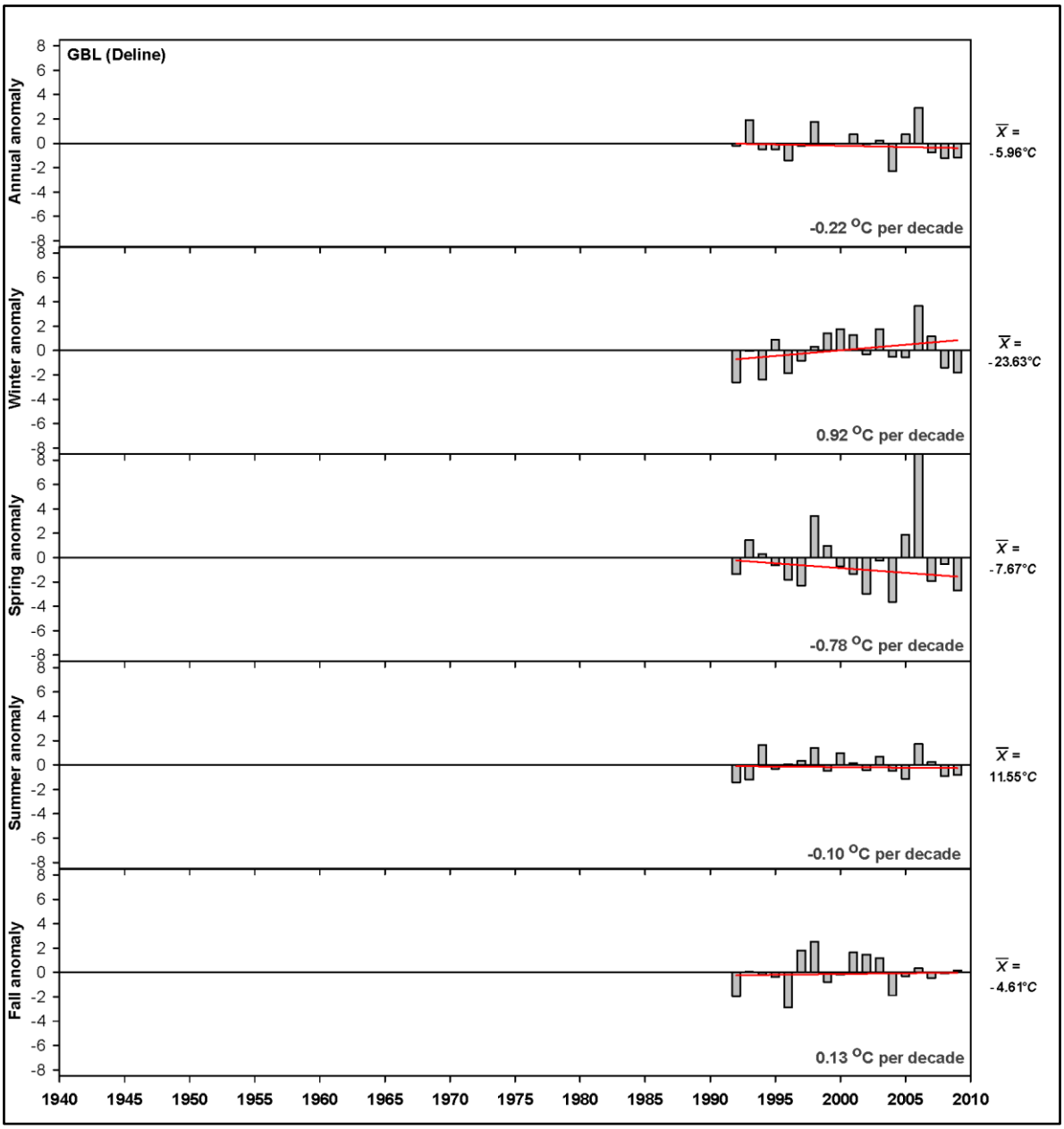

Figure 3.6: Annual and seasonal mean air temperature (°C) for winter (DJF), spring (MAM), summer (JJA), and autumn (SON) at Deline meteorological station (1992-2009). Mean air temperatures are provided as a reference on the right hand side of the graphs.

3.3 Summary

In this chapter, the physical characteristics, local/regional climate, and the ice cover conditions of GBL and GSL were reviewed. The different hydrological and bathymetric systems of two large lakes and their differing location lead to contrasting climate conditions and ice regimes. Situated at a more southern location, GSL presents a longer open-water period with higher summer temperature than GBL (Rouse et al., 2008a; Schertzer et al., 2008). In contrast to GBL, which is relatively isolated hydrologically, the inflow of freshwater from the Slave River influences the ice break-up process in GSL. Through the visual interpretation of SSM/I brightness temperature measurements (1979-2005), CFO and WCI dates for GBL have been reported to be three and four weeks later than those for GSL (Rouse et al., 2008a). Sub-zero winter temperatures provide subsequent ice growth and thickening for five to six months on the two lakes. Much less is known, however, about the seasonal evolution of ice thickness, mainly for GBL since no systematic measurements have been made on this lake in the past.

Given that air temperatures have been increasing significantly in the GSL region since the 1940s, particularly in the winter and spring seasons, it is expected that this has had an impact on ice cover phenology. Wintertime increases in both air temperature and snowfall also had a likely influence on ice thickness on GSL, though this remains to be investigated. The historical climate record of the GBL region is simply too short to draw any solid conclusion regarding the impact of climate on ice conditions for this lake, even more so because very few ice phenology observations exist for this lake. Since both GSL and GBL are very large and that no investments are foreseen in the establishment of in-situ observation sites other than the existing one in Back Bay (GSL), increase research activities must take place on the development of satellite-based retrieval algorithms in order to improve our understanding of ice conditions on GBL and GSL in relation to climate. This thesis contributes to this goal by developing and applying ice phenology and thickness algorithms on the two lakes using AMSR-E data for the period 2002-2009.

Chapter 4: Estimating Ice Phenology on large northern lakes from AMSR-E: algorithm development and application to Great Bear Lake and Great Slave Lake, Canada

In this chapter, time series of brightness temperatures (T_B) from the Advanced Microwave Scanning Radiometer–Earth Observing System (AMSR-E) are examined to determine ice phenology variables on the two largest lakes of northern Canada: Great Bear Lake (GBL) and Great Slave Lake (GSL). T_B measurements from the 18.7, 23.8, 36.5, and 89.0 GHz channels (H- and V- polarization) are compared to assess their potential for detecting freeze-onset/melt-onset and ice-on/ice-off dates on both lakes. The 18.7 GHz (H-pol) channel is found to be the most suitable for estimating these ice dates as well as the duration of the ice cover and ice-free seasons. A new algorithm is proposed using this channel and applied to map all ice phenology variables on GBL and GSL over seven ice seasons (2002-2009). Analysis of the spatio-temporal patterns of each variable at the pixel level reveals that: 1) both freeze-onset and ice-on dates occur on average about one week earlier on GBL than on GSL (Day of Year (DY) 318 and 333 for GBL; DY 328 and 343 for GSL); 2) the freeze-up process or freeze duration (freeze-onset to ice-on) takes a slightly longer amount of time on GBL than on GSL (about 1 week on average); 3) melt-onset and ice-off dates occur on average one week and approximately four weeks later, respectively, on GBL (DY 143 and 183 for GBL; DY 135 and 157 for GSL); 4) the break-up process or melt duration (melt-onset to ice-off) lasts on average about three weeks longer on GBL; and 5) ice cover duration estimated from each individual pixel is on average about three weeks longer on GBL compared to its more southern counterpart, GSL. A comparison of dates for several ice phenology variables derived from other satellite remote sensing products (e.g.

NOAA Interactive Multisensor Snow and Ice Mapping System (IMS), QuikSCAT, and Canadian Ice Service Database) show that, despite its relatively coarse spatial resolution, AMSR-E 18.7 GHz provides a viable means for monitoring of ice phenology on large northern lakes.

Key words: Lake ice, phenology, AMSR-E, Great Bear Lake, Great Slave Lake, Canada

4.1 Introduction

Lake ice cover is an important component of the terrestrial cryosphere for several months of the year in high-latitude regions (Duguay et al., 2003b). Lake ice is not only a sensitive indicator of climate variability and change, but it also plays a significant role in energy and water balance at local and regional scales. The presence of an ice cover alters lake-atmosphere exchanges (Duguay et al., 2006; Brown and Duguay, 2010). When energy movement occurs during temperature change, heat transfer (thermodynamics) influences ice thickening as well as the timing and duration of freeze-up and break-up processes, which is referred to as ice phenology (Jeffries and Morris, 2007). Lake ice phenology, which encompasses freeze-onset/melt-onset, ice-on/ice-off dates, and ice cover duration, is largely influenced by air temperature changes and is therefore a robust indicator of climate conditions (e.g. Bonsal et al., 2006; Duguay et al., 2006; Kouraev et al., 2007a; Latifovic et al., 2007; Schertzer et al., 2008; Howell et al., 2009).

The analysis of historical trends (1846-1995) in *in situ* observations of lake and river ice phenology has provided evidence of later freeze–up (ice-on) and earlier break-up (ice-off) dates at the northern hemispheric scale (Magnuson et al., 2000; Brown and Duguay, 2010). In Canada, from 1951 to 2000, trends towards earlier ice-off dates have been observed for many lakes, but ice-on dates have shown few significant trends over the same period (Duguay et al., 2006). The observed changes in Canada's lake ice cover have also been found to be influenced by large-scale atmospheric forcings (Bonsal et al., 2006). Canada's government-funded historical ground-based observational network has provided much of the evidence for the documented changes for most of the 20th century and for establishing

links with variations in atmospheric teleconnection indices, notably Pacific oscillation patterns such as Pacific North American Pattern and Pacific Decadal Oscillation. Unfortunately, the Canadian ground-based lake ice network has been eroded to the point where it can no longer provide the quantity of observations necessary for climate monitoring across the country. Satellite remote sensing is the most logical means for establishing a global observational network as the reduction in the ground-based lake ice network seen in Canada has been mimicked in many other countries of the Northern Hemisphere (IGOS, 2007).

From a satellite remote sensing perspective, dates associated with estimating the freeze-up process (i.e. onset of freeze until a complete sheet of ice is formed) in autumn and early winter are particularly difficult to determine using optical satellite sensors such as the Moderate Resolution Imaging Spectroradiometer (MODIS) and the Advanced Very High Resolution Radiometer (AVHRR) on high-latitude lakes due to long periods of obscuration by darkness and extensive cloud cover (Maslanik et al., 1987; Jeffries et al., 2005; Latifovic and Pouliot, 2007). QuikSCAT has been used successfully to derive and map freeze-onset, melt-onset and ice-off dates on Great Bear Lake (GBL) and Great Slave Lake (GSL) (Howell et al., 2009). Unfortunately, QuikSCAT data are no longer available for lake ice monitoring on large lakes since its nominal mission ended on November 23, 2009. Previous investigations have shown the utility of observing lake ice phenology variables through the visual interpretation of brightness temperature (T_B) changes from the Scanning Multichannel Microwave Radiometer (SMMR) at 37 GHz (Barry and Maslanik, 1993) and the Special Sensor Microwave/Imager (SSM/I) at 85 GHz (Walker et al., 1993, 2000) on GSL, but identifying spatial variability in these variables is difficult due to their coarse resolution (~25 km). In a recent study, SSM/I has been used in combination with radar altimetry to determine automatically ice phenology events on Lake Baikal (Kouraev et al., 2007a).

Measurements by the Advanced Microwave Scanning Radiometer–Earth Observing System (AMSR-E) that offer improved spatial resolution have yet to be assessed for monitoring ice

phenology. The objectives of this paper are to i) evaluate the utility of AMSR-E T_B measurements for estimating lake ice phenology, ii) develop a comprehensive algorithm for mapping lake ice phenology variables, and iii) apply the algorithm over both GBL and GSL to investigate the spatio-temporal variability of each lakes ice phonology from 2002 to 2009.

4.2 Background

4.2.1 Passive microwave radiometry of lake ice

The discrimination of ice cover characteristics from passive microwave T_B measurements requires a good knowledge of the radiometric properties of ice in nature (Kouraev et al., 2007a). In contrast to the high-loss characteristics of sea ice (due to salinity), one of the major microwave characteristics of pure freshwater ice is its low-loss transmission behavior (Ulaby et al., 1986). The brightness temperature (T_B) at passive microwave frequencies is defined as the product of the emissivity (ε) and physical temperature (T_{kin}) of the medium:

$$T_B = \varepsilon T_{kin} \quad \textbf{(4.1)}$$

Passive microwave systems can measure, regardless of cloud coverage and darkness, naturally emitted radiation through T_B. Since emissivity ranges between 0 and 1, the T_B is lower than the kinetic temperature of the medium. The large change in emissivity from open water (ε = 0.443-0.504 at 24 GHz) to ice covered conditions (ε = 0.858-0.908 at 24 GHz) (Hewison and English, 1999; Hewison, 2001) makes the determination of the timing of ice formation and decay on large, deep lakes, feasible from T_B measurements. The emissivity of ice, and therefore T_B, further increases from its initial formation as the effect of the radiometrically cold water under the ice cover decreases with ice thickening (Kang et al., 2010).

4.2.2 Definitions of ice phenology variables

The definitions of freeze-up and break-up are opposite: the former describes the time period between the beginning of ice formation and the formation of a complete sheet of ice, while the latter describes the time period between the onset of spring melt and the complete disappearance of ice from the lake surface. Since the algorithm presented herein operates on a pixel-by-pixel basis and is applied over entire lake surfaces, it is important to provide clear definitions of the ice phenology variables as they relate to individual pixels and over whole lakes (or lake sections) (**Table 4.1)**. At the level of the pixel, the freeze-up period encompasses freeze onset (FO), ice-on and freeze duration (FD), while the break-up period comprises melt onset (MO), ice off and melt duration (MD). The period between ice-on and ice-off covers an ice season and is referred to as ice cover duration (ICDp; p for pixel). At the lake or lake section level (third column of **Table 4.1**), complete freeze over (CFO), water clear of ice (WCI) and ice cover duration (ICDe; e for entire lake or lake sections as to avoid land contamination in some AMSR-E T_B measurements) are the terms used from here onward. CFO corresponds to the date when all pixels within the lake or lake section have become ice-covered (i.e. all flagged with having ice-on). WCI corresponds to the date when all pixels have become ice-free (i.e. all flagged with having ice-off). While ICDp is calculated for each individual pixel from dates of ice-on to ice-off, ICDe is determined as the number of days between CFO and WCI within an ice season.

Table 4.1: Definition of ice phenology variables at per pixel level and for entire lake or lake section.

	Pixel level	Entire lake or lake section
Freeze-up Period	**Freeze onset (FO)**: First day of the year on which the presence of ice is detected in a pixel and remains until ice-on **Ice-on**: Day of the year on which a pixel becomes totally ice-covered **Freeze duration (FD)**: number of days between freeze-onset and ice-on dates	**Complete freeze over (CFO)**: Day of the year when all pixels become totally ice-covered
Break-up period	**Melt onset (MO)**: First day of the year on which generalized spring melt begins in a pixel **Ice-off**: Day of the year on which a pixel becomes totally ice-free **Melt duration (MD)**: numbers of days between melt-onset and ice-off dates	**Water clear of ice (WCI)**: Day of the year when all pixels become totally ice-free
Ice season	**Ice cover duration (ICDp)**: number of days between ice-on and ice-off dates	**Ice cover duration (ICDe)**: number of days between CFO and WCI

4.3 Study area

GBL and GSL are two of the largest freshwater lakes in the world. Located in the Mackenzie River Basin they fall within two physiographic regions of Canada's Northwest Territories: the Precambrian Shield and the Interior Plains (**Figure 4.1**). The eastern parts of both lakes are situated in the Precambrian Shield. Its undulating topography with bedrock outcrops causes the formation of rounded hills and valleys. The high topography of the western Cordillera and low relief of the central and eastern parts of the Mackenzie Basin strongly influence the regional climate (e.g. atmospheric circulation pattern and the advective heat and moisture fluxes) (Woo et al., 2008). Most of GBL and the western/central parts of GSL are located in the flat-lying Interior Plains and underlain by thick glacial, fluvial, and lacustrine deposits; in addition, the Plains are dotted with numerous wetlands and lakes (Woo et al., 2008). GBL and GSL lie between 60° to 67° N and between 109° to 126° W (**Figure 4.1**), and, respectively, have surface areas of 31.3×10^3 km^2 and 28.6×10^3 km^2, and average depths of 76 m and 88 m (Rouse et al., 2008d;

Woo et al., 2008). The northern extent of GBL is influenced by colder temperatures than its more southern counterpart (Rouse et al., 2008a).

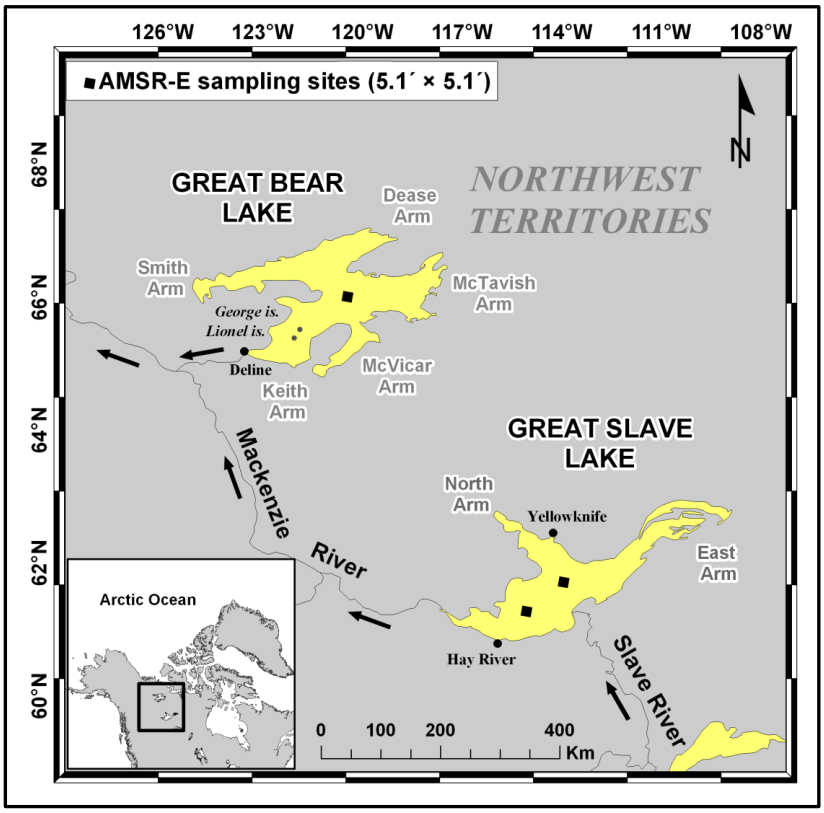

Figure 4.1: Map showing location of Great Bear Lake (GBL) and Great Slave Lake (GSL), and their meteorological stations (Deline, Yellowknife, and Hay River) within the Mackenzie River Basin. Solid squares represent 5.1´ × 5.1´ (9.48 km × 9.48 km) of sampling sites at 18.7 GHz for the development of the ice phenology algorithm. Arrows indicate river flow direction.

From 2002 to 2009, the period of analysis of this study, the average air temperature recorded at the Deline weather station (65° 12' N, 123° 26' W), near the western shore of GBL, ranged between -25.4 °C and -20.6 °C for winter (DJF) and from 10.0 °C to 12.1 °C for summer (JJA) with 20.2 cm of average annual snowfall (**Table 4.2**). For GBL, complete water turnover occurs at least in some parts of the lake and no break-up occurs until early July (Rouse et al., 2008d).

Table 4.2: Seasonal mean air temperature (°C) for winter (DJF), spring (MAM), summer (JJA) and autumn (SON), and annual snowfall (cm) recorded at Deline (GBL), Yellowknife and Hay River combined (GSL) meteorological stations (2002-2009). M indicates missing data. S.D. is standard deviation.

	DJF		MAM		JJA		SON		Annual temp		Annual snowfall (cm)	
	GBL	GSL	GBL	GSL	GBL	GSL	GBL	GSL	GBL	GSL	GBL	GSL
2002	-23.9	-21.5	-10.6	-9.5	11.1	14.2	-3.1	-1.3	-6.0	-4.0	14.6	15.5
2003	-22.1	-20.6	-8.2	-4.3	11.6	14.7	-3.8	-0.3	-6.1	-2.9	22.2	16.2
2004	-24.4	-21.0	-11.7	-7.6	10.4	13.8	-6.9	-2.9	-8.7	-5.1	16.1	16.9
2005	-24.7	-22.9	-6.0	-3.6	10.0	13.6	-5.4	0.0	-5.6	-2.1	25.7	24.1
2006	-20.6	-15.9	-7.8	-1.0	12.1	15.9	-4.9	-2.0	-5.5	-0.9	28.8	24.0
2007	-22.7	-18.7	-9.7	-4.7	11.2	14.6	-5.3	-1.6	-7.0	-3.3	17.0	19.7
2008	-25.0	-23.5	-8.2	-6.0	10.6	15.4	-4.7	0.0	-7.2	-3.9	16.7	26.9
2009	-25.4	-23.8	-10.4	-7.1	10.7	14.2	-4.5	0.1	-7.1	-3.7	M	22.2
Avg	-23.5	-21.8	-8.6	-4.9	11.4	14.5	-4.6	-1.6	-6.3	-3.4	20.2	20.7
S.D.	1.5	2.9	2.0	2.2	0.8	0.9	1.5	1.7	1.1	1.3	5.5	4.2

GSL is part of the north-flowing river system in the Mackenzie Basin (Rouse et al., 2008a). Situated at a more southern location, the mean air temperature in the GSL area is generally warmer than that of GBL, and therefore the GSL open-water period is about four to six weeks longer than it is at GBL (Rouse et al., 2008a; Schertzer et al., 2008). GSL is ice-free from the beginning of June until mid- to late-December; however, the ice conditions vary significantly from year to year on this lake (Blanken et al., 2008). The high spatiotemporal variability in air temperature and wind speed over GSL influences the surface water temperature and lake heat flux (Rouse et al., 2008a; Schertzer et al., 2008). From 2002 to 2009, the mean air temperature in winter ranged from -23.8 °C to -15.9 °C and between 13.6 °C and 15.9 °C in summer, with 20.7 cm of average annual snowfall (**Table 4.2**). Spring and autumn temperatures, which mark the beginning of the break-up and freeze-up periods, respectively, in the GSL region (-9.5 °C to -1.0 °C; -2.9 °C to 0.1 °C) are higher than near GBL (-11.7 °C to -6.0 °C; -6.9 °C to -3.1 °C) due to the latitudinal difference between the two lakes.

4.4 Data

Two data sets were used in this study. Primary data correspond to those utilized to examine the sensitivity of passive microwave T_B measurements at various frequencies and to develop the ice phenology algorithm. They consist of meteorological station (air temperature) and AMSR-E data. The secondary, auxiliary, data correspond to ice products or images from other sources. They are used for comparison with the AMSR-E derived ice phenology variables.

4.4.1 Primary data

4.4.1.1 AMSR-E

AMSR-E T_B data were obtained for the period 2002-2009. AMSR-E (fixed incident angle: 54.8 degree) is a conically-scanning, twelve-channel passive microwave radiometer system, measuring horizontally and vertically polarized microwave radiation from 6.9 GHz to 89.0 GHz (Kelly, 2009). The instantaneous field-of-view (IFOV) for each channel varies from 76 by 44 km at 6.9 GHz to 6 by 4 km at 89.0 GHz, and the along-track and cross-track sampling interval of each channel is 10 km (5 km sampling interval in 89.0 GHz). In this study, the AMSR-E/Aqua L2A global swath spatially raw brightness temperature product (AE_L2A) was used.

T_B at 18.7, 23.8, and 36.5 GHz AMSR-E observations for each day falling within a 5.1′ × 5.1′ grid for both descending and ascending overpasses were averaged over the areas of interest, within the central sections of GBL (66° N, 120° 30′ W) and GSL (61° 19.8′ N, 115° W and 61° 41.8′ N, 113° 49.5′ W) (**Figure 4.1**). The 6.9 GHz and 10.7 GHz channels were not considered, as they are more subject to land contamination from lakeshores due to their larger footprint. The divide-and-conquer method for a Delaunay triangulation and inverse distance weighted linear interpolation were applied to the L2A data because the T_Bs in ascending and descending modes did not have matching geographic positions over GBL

and GSL due to different orbit overpasses. The sampling intervals at all frequency bands are spaced every 10 km (5 km at 89.0 GHz) along and across track in AMSR-E L2A products (Kelly, 2009). Therefore, we chose 10 km grid spacing for the linear interpolation, except for 89 GHz, for which we chose a 5 km grid spacing.

4.4.1.2 Meteorological station data

Meteorological data from the National Climate Data and Information Archive of Environment Canada (http://climate.weatheroffice.ec.gc.ca/climateData/canada_e.html) were acquired from three stations located in the vicinity of GBL and GSL. The stations selected include Deline (YWJ, 65° 12' N, 123° 26' W) to provide climate information on GBL, and Yellowknife (YZF, 62° 27.6' N, 114° 26.4' W) and Hay River (YHY, 60° 50.4' N, 115° 46.8' W) to characterize the climate in the GSL area (**Figure 4.1**). Time series of maximum and mean air temperatures from 2002 to 2009 were used for comparison with AMSR-E T_B measurements as supporting data for the development of the ice phenology algorithm.

4.4.2 Auxiliary data

Auxiliary data used for comparison with AMSR-E derived ice phenology variables consisted of NOAA Interactive Multisensor Snow and Ice Mapping System (NOAA/IMS) ice products, weekly ice observations from the Canadian Ice Service (CIS) during freeze-up and break-up period, and MODIS images acquired during the break-up period (not examined during freeze-up due to polar darkness). FO, MO, and ice-off dates derived from the QuikSCAT Scatterometer Image Reconstruction eggs product at the pixel scale by Howell et al. (2009) are compared with the same ice phenology variables derived from AMSR-E for the period 2002-2006.

The NOAA/IMS (http://www.natice.noaa.gov/ims/) 24 km and 4 km resolution grid products (Helfrich et al., 2007) were also available for comparison. The IMS 4 km product is available since 2004. Ice-on and ice-off dates (binary value: ice vs open water) at the pixel level as well as CFO dates (all pixels coded as ice) and WCI dates (all pixels coded as

open water) on both GBL and GSL were derived for the period 2004-2009. The 4 km IMS product was used for comparison with AMSR-E derived ice phenology events.

CIS weekly observations of GBL and GSL ice cover were obtained from 2002-2009. Analysts at the CIS determine a single lake-wide ice fraction value in tenths ranging from 0 (open water) to 10 (complete ice cover) every Friday from the visual interpretation of NOAA AVHRR (1 km pixels) and Radarsat ScanSAR images (100 m pixels) compiled over a full week for many lakes across Canada, including GBL and GSL. CFO and WCI dates can be derived from this product with about a one-week accuracy. CFO was determined as the date when the ice fraction changes from 9 to 10 and remains at this value for the winter period, while WCI was determined as the date when the lake-ice fraction passes from 1 to 0. Lake-wide CFO and WCI dates were derived for all ice seasons corresponding to the AMSR-E (2002-2009) observations.

Finally MODIS quick-look images of GBL and GSL (2002-2009) were downloaded from the Geographic Information Network of Alaska (http://www.gina.alaska.edu) for general visual comparison with AMSR-E derived ice products during spring break-up. No suitable images were available during fall freeze-up due to long periods of extensive cloud cover and polar darkness. The MODIS quick-look images are provided as true-color composites (Bands 1, 4, 3 in RGB) - Band 1 (250-m, 620-670 nm), Band 4 (500-m, 545-565 nm), and Band 3 (500-m, 459-479 nm).

4.5 Ice phenology algorithm

4.5.1 Examination of T_B evolution during ice-cover and ice-free seasons

The development of a new algorithm for determining various ice phenology variables through ice seasons required the seasonal evolution of horizontally and vertically polarized T_B at different frequencies be examined first. The sensitivity of T_B at 18.7, 23.8, 36.5, and 89 GHz to ice phenology was examined by selecting one pixel located in the central section

of GBL (66° N, 120° 30´ W) and two in the main basin of GSL (61° 19.8´ N, 115° W and 61° 41.8´ N, 113° 49.5´ W) (see **Figure 4.1**). Air temperature data from the meteorological stations were used in support of the analysis of the temporal evolution of the AMSR-E T_B to detect ice phenology events during the freeze-up and break-up periods at the three sampling sites (pixels) that could then guide the development of the ice phenology algorithm. Although the temporal evolution was examined at the three sites and for all years (2002-2009), for sake of brevity, one site on GBL from 2003-2004 is used to illustrate the general sensitivity of T_B during the freeze-up and break-up periods (**Figure 4.2**). Changes in T_B are interpreted separately below for the freeze-up and the break-up periods.

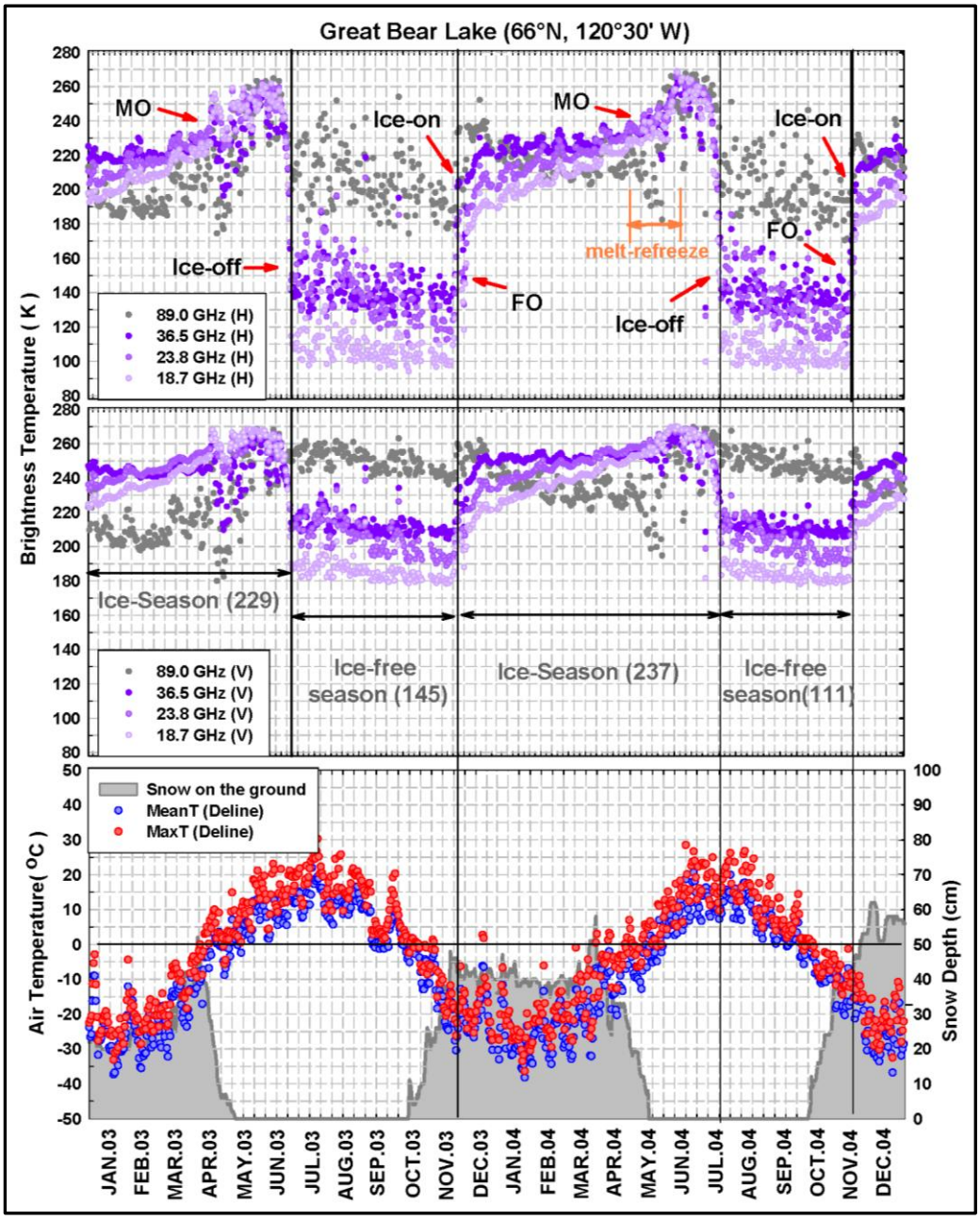

Figure 4.2: Temporal evolution of horizontal (top) and vertical (middle) polarized brightness temperature at 18.7 (light violet), 23.8 (middle violet), 36.5 (dark violet), 89.0 (dark grey) GHz (2003 – 2004) for sampling site on GBL (see Fig. 1). The time series of maximum (Max_T, red) and mean (Mean_T, blue) air temperatures obtained at Deline meteorological station is shown in the bottom panel of the figure, with snow depth as grey shaded area. Numbers after both "Ice Season" and "Ice-free Season" indicate number of days.

4.5.1.1 Freeze-up period

Using the sampling site on GBL as an example (see **Figure 4.1**), when surface air temperature falls below the freezing point (**Figure 4.2**), the expected increase in T_B with the onset of ice cover formation lags due to the large heat capacity causing delayed ice formation of GBL. This is also observed over GSL (not shown). As shown in **Figure 4.2**, it takes about four to six weeks for the central part of GBL to show the beginning of the freeze-up process. T_B then starts to increase rapidly in association with an increase in fractional ice coverage (FO to ice-on). The distinct increase of T_B is more strongly apparent at horizontal polarization (**Figure 4.2**, upper) for which T_B increases by approximately 70-80 K from open water (ice-free season) to ice-on conditions, compared to vertical polarization (**Figure 4.2**, middle) for each frequency.

From the ice-on date near mid-December to the onset of melt (MO), the increase in T_B is due to ice growth and thickening until lake ice reaches its maximum thickness around mid-April. An increase in T_B is expected during the ice growth season since thicker ice reduces the influence of the lower emissivity (radiometrically cold) liquid water below the ice (Kang et al., 2010). The slope (rate of change) of T_B with time is steeper at 18.7 GHz than at 23.8, 36.5 and 89 GHz during ice growth due to greater penetration depth at lower frequencies. The rate of increase in T_B with ice thickening slows down more quickly at the higher frequencies as the ice becomes thicker (**Figure 4.2**). The oscillating behavior of T_B at H-pol and V-pol during the ice growth period depends greatly on the imaginary part of the index of refraction of ice (Chang et al., 1997; Kang et al., 2010). Differences in T_B among different frequencies are negligible once the lake ice/snow on ice surface becomes wet during warm winter episodes and starting with MO.

4.5.1.2 Break-up period

Once the mean air temperature begins to exceed 0 °C, T_B increases rapidly as a result of the higher air temperature and increasing shortwave radiation absorption (decreasing albedo) at

the ice/snow surface signalling the start of MO. The wetter the snow cover becomes, the more the observed T_B also increases due to snow's high emissivity during the break-up period (Jeffries et al., 2005).As shown in **Figure 4.2**, during the break-up period on GBL, melt-refreeze events lead to fluctuations in T_B at 18.7-89 GHz along the general spring melt trajectory starting with MO. A similar pattern is noticeable from T_B values analyzed over GSL (not shown). The existence of clear ice causes a rapid break-up process, resulting in decreasing T_B. The snow or snow ice (if any), and finally black ice melt sequentially due to higher albedo of snow ice and more absorption of black ice; the H-pol and V-pol T_B drop rapidly until the ice-off date (**Figure 4.2**). The definition of black ice (or clear ice) and snow ice are described in Kang et al. (2010). During the middle of July, T_B, which is affected by the radiometrically cold (low emissivity) freshwater, significantly decreases by about 100-140 K from ice-covered to ice-free (open water) conditions.

4.5.2 Justification of choice of frequency and polarization for algorithm

Based on the overall examination of the evolution of T_B during the ice and ice-free seasons on GBL and GSL at different frequencies and polarizations, 18.7 GHz H-pol measurements appear to be the most suitable for the development of an ice phenology algorithm. Although H-pol is more sensitive than V-pol to wind-induced open water surface roughness, it also shows a larger rise in T_B from open water to ice cover during the later freeze-up and earlier break-up periods. Thus, it is easier to determine T_B thresholds (described in the section below) related to ice phenology variables at H-pol than at V-pol during those periods. Second, 89 GHz is known to be more sensitive to atmospheric contamination (Kelly, 2009) and is also strongly affected by open water surface roughness from wind, particularly at H-pol. This later effect is also apparent at 23.8 and 36.5 GHz. Occasionally high T_B values at 23.8 and 36.5 GHz during the open water season make it difficult to detect the timing of FO and ice-off dates. Although 89.0 GHz (3.5 × 5.9 km) from AMSR-E can be good for estimating sea ice concentration due to its finer spatial resolution, AMSR-E 18.7 GHz is better for defining ice phenology variables such as freeze-onset and melt-onset because this frequency has longer penetration depth, allowing less lake ice surface scattering. In

addition, brightness temperatures (T_B) at 89.0 GHz are much more sensitive to surface roughness induced by winds during the open water period compared to the lower frequency channels. As clearly shown in **Figure 4.2**, variations in T_B at 89 GHz are large during this period. This makes the estimation of FO and ice-off dates, in particular, difficult with the thresholding approach presented in this paper. Overall, 18.7 GHz H-pol shows less limitations for detecting a broader range of ice phenology variables (FO, ice-on, MO, and ice-off) than the other channels.

4.5.3 Determining thresholds for retrieval of ice phenology variables

A flowchart showing the processing steps for determining the ice phenology variables is given in **Figure 4.3**. Based on the analysis of T_B values at the three test sites on GBL/GSL over seven ice seasons, a suite of criteria (minimum and maximum thresholds, averages of preceding and succeeding days, and threshold value of number of days to the maximum T_B in the time series, DistM) was devised to detect FO, ice-on, MO, and ice-off dates.

4.5.3.1 Freeze-up period

The FO date is detected during the upturn of T_B from an open water surface. A maximum T_B threshold value of 180 K is high enough to avoid confusion with fluctuating T_B values influenced by wind-induced roughness of the open water surface. Then, in order to discriminate T_B under open water conditions from the starting point of FO, the average taken from the succeeding twenty days for each individual day of the time series is calculated. This average value must fall within the range of 110 K and 140 K. The last criterion consists of finding the maximum T_B value in the time series, which is reached late during the ice season. Once found, the number of days from each day to that of the maximum T_B (DistM in **Figure 4.3**) is calculated. DistM must be less than 250 days, in addition to falling within the threshold T_B values given above, for the algorithm to be able to detect FO. For detecting the ice-on date, first maximum and minimum threshold values of 195 K and 160 K are used. Then, as an extra criterion to distinguish between the FO date and ice-on date, the average T_B value of the 15 days preceding each individual day in the time series has to fall between 100 and 155 K. Lastly, DistM must be less than 220 days.

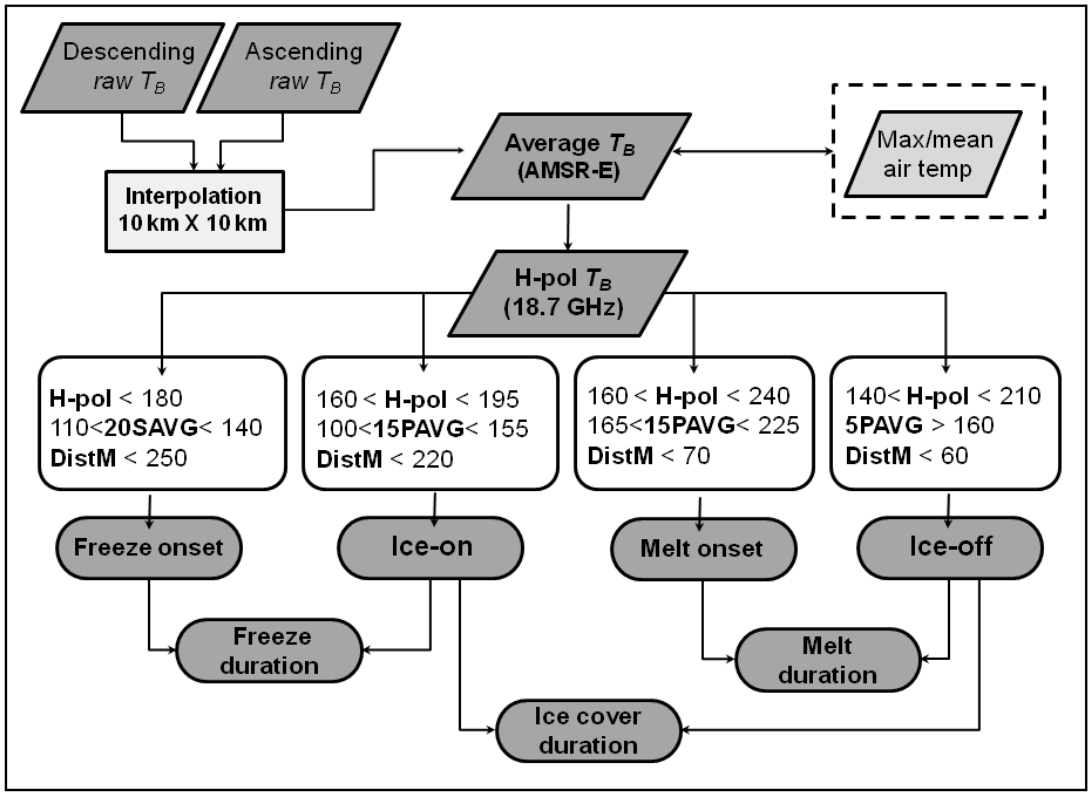

Figure 4.3: Flowchart of ice phenology algorithm based on AMSR-E 18.7 GHz horizontal polarization (H-pol) brightness temperature (T_B). All threshold values are explained in section 4.5.3.

4.5.3.2 Break-up period

For the determination of the MO date, maximum and minimum threshold values are set to 240 K and 160 K. Then, for discriminating the starting point of MO from other days during the ice growth/thickening season, the average T_B calculated from the previous fifteen days of each individual day in the time series must fall between 165 K and 225 K threshold and with a DistM of less than 70 days. The ice-off date is detected from a sharp drop in T_B from that of the melt period that starts with MO (**Figure 4.2**). For this last phenology variable, the maximum and minimum thresholds are set to 140 K and 210 K. To ensure discrimination of this first day of the ice-free season from those of later days, the average T_B value of the preceding five days is fixed to 160 K and with DistM less than 60 days.

4.6 Results and Discussion

4.6.1 Spatio-temporal variability of lake ice phenology variables

The algorithm described above was applied to all interpolated 10 km pixels on GBL and GSL for every day during the period 2002-2009 to produce maps of FO, ice-on, MO and ice-off dates, as well as freeze duration (FD), melt duration (MD), and ice cover duration (ICD) averaged over all years and for individual years (**Figures 4.4-4.17**). Recognizing that the relatively coarse spatial resolution of the product leads to a certain level of land contamination in T_B values along lakeshores and where a high concentration of islands exists (e.g. eastern arm of GSL), confidence regions were drawn on the two lakes with an outer buffer zone of 10 km. Average dates and duration of the ice phenology variables calculated from all pixels over the greatest extent as possible for the lakes as well as within the confidence regions are included in **Tables 4.3-4.5**. Interestingly, in these tables one can see that the standard deviations of ice phenology variables are almost always larger for GSL than for GBL, indicating that ice phenology processes are generally more variable spatially (i.e. between pixels) on GSL which is located at a more southern latitude.

4.6.1.1 Freeze-up period

Once water cools to the freezing point, ice begins to form first in shallow near shore areas. Freeze-up is influenced primarily by air temperature and to a lesser extent by wind, in addition to lake depth. On average, the date of FO occurs approximately one week earlier on GBL than on its southern counterpart, GSL (**Table 4.3**). For GBL, the latest FO date over the study period occurred during ice season 2008-2009 (Day of Year or DY 330, late November) followed by 2003-2004 (DY 322). The earliest FO date happened in 2004-2005 (DY 308, early November). For GSL, both the 2005-2006 and 2008-2009 ice seasons experienced the latest FO dates of DY 332 and 342, respectively. The earliest FO date occurred in 2006-2007 on DY 316, closely followed by 2004-2005 (DY 322). In addition to the effect of fall temperature in explaining earlier/later FO dates, an early ice break-up

(longer period of solar radiation absorption by water) and warmer summer of the preceding months can result in the late onset of freeze-up for the two large, deep, lakes that store a considerable amount of heat during the open water season (Brown and Duguay, 2010). The latter process may be the case for ice season 2008-2009. Noteworthy is the fact that, in contrast to GBL, GSL's timing of ice formation is somewhat influenced by river inflow from the Slave River in its southeast section (Howell et al., 2009). A slight delay in FO is noticeable during most years at its mouth (see **Figures 4.1 and 4.4**). GBL's ice regime is not affected by such inflow (**Figure 4.4**).

Table 4.3: Summary of ice phenology variables during the freeze-up period (average day of freeze-onset (FO) and ice-on, and number of days of freeze duration (FD)) for GBL and GSL (2002-2009). Values within confidence regions in bold. Standard deviation in parentheses.

Year	FO		Ice-On		FD	
	GBL	GSL	GBL	GSL	GBL	GSL
2002-03	311/**320** (14/**7**)	318/**331** (18/**4**)	328/**333** (11/**7**)	334/**345 (**17/**7**)	32/**28** (11/**5**)	31/**19** (17/**10**)
2003-04	313/**322** (11/**5**)	319/**329** (14/**5**)	332/**337** (8/**5**)	338/**345** (11/**5**)	31/**28** (7/**5**)	27/**15** (15/**7**)
2004-05	303/**308** (9/**4**)	313/**322** (13/**3**)	321/**323** (6/**4**)	331/**338** (12/**4**)	26/**22** (9/**3**)	24/**12** (13/**6**)
2005-06	309/**314** (9/**4**)	320/**332** (15/**4**)	326/**330** (8/**4**)	337/**344** (12/**4**)	28/**26** (11/**7**)	30/**27** (18/**20**)
2006-07	312/**317** (9/**3**)	310/**316** (9/**5**)	331/**335** (7/**3**)	328/**332** (8/**3**)	26/**24** (5/**2**)	24/**19** (9/**7**)
2007-08	311/**316** (8/**3**)	318/**326** (10/**4**)	329/**333** (8/**4**)	338/**343** (9/**4**)	27/**26** (4/**2**)	24/**16** (10/**6**)
2008-09	320/**330** (13/**6**)	330/**342** (15/**6**)	334/**340**(8/**4**)	344/**352** (12/**3**)	12/**10** (4/**3**)	15/**9** (8/**5**)
Average	311/**318** (11/**4**)	318/**328 (**11/**3**)	329/**333** (6/**4**)	336/**343** (9/**4**)	26/**23** (9/**3**)	25/**17** (11/**7**)

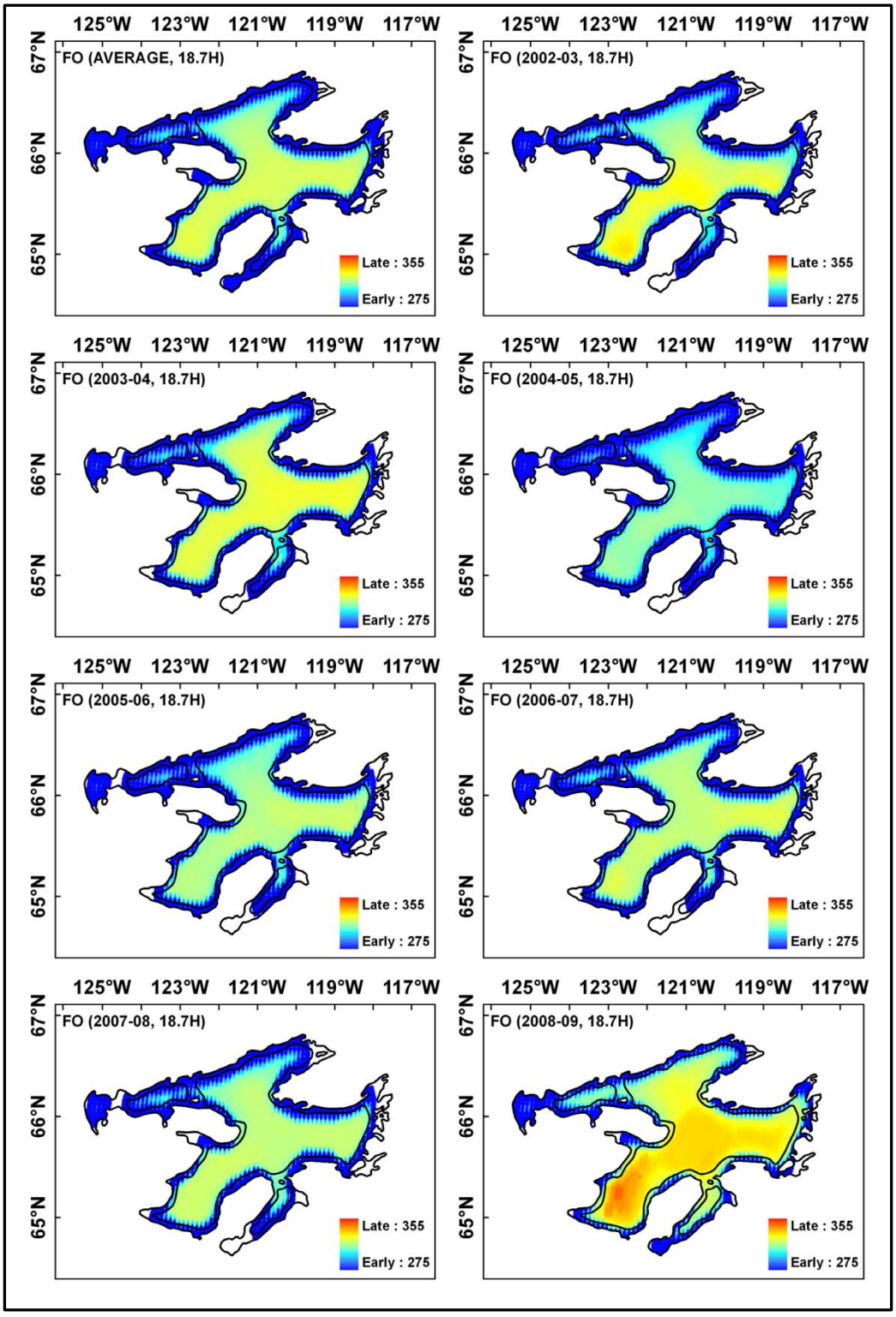

Figure 4.4: Freeze-onset (FO) over seven ice seasons (2002-2009) and average (top left panel) for GBL. Legend is day of year.

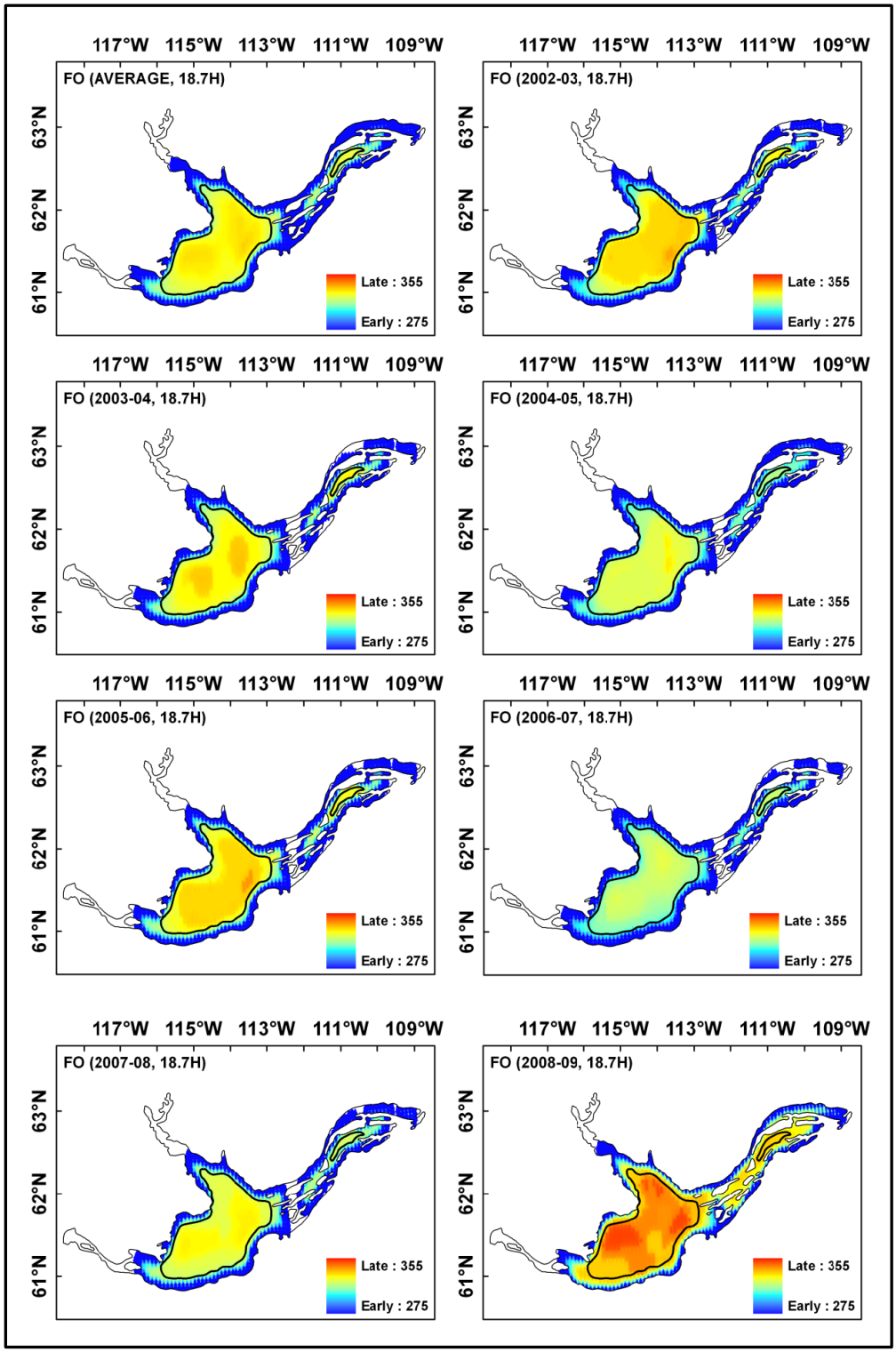

Figure 4.5: Freeze-onset (FO) over seven ice seasons (2002-2009) and average (top left panel) for GSL. Legend is day of year.

Similar to FO, ice-on occurs approximately one week later on GSL than on GBL. The average ice-on date occurs on DY 333 and 343 for GBL and GSL, respectively (**Table 4.3**). Schertzer et al. (2008) and Walker et al. (2000) estimated average CFO in the main basin of the GSL to occur on DY 342 for the period 1988-2003. Spatially, for GBL (**Figure 4.4** and **Table 4.3**), the ice-on dates take place in the Central Basin around early December and for GSL, the ice-on dates occur in mid-December. From FO to ice-on, it takes two to three weeks on both lakes. For GBL, the longest FD over the study period happened during ice season 2003-2004 (28 days), closely followed by 2005-2006 and 2007-2008 (26 days). The shortest FD occurred in 2008-2009 (10 days) (**Table 4.3**). For GSL, the longest FD took place during ice season 2005-2006 (27 days), while the shortest FD happened in 2008-2009 (9 days) (**Table 4.3**). FD in GBL usually takes about 1-2 weeks longer than that in GSL, likely due to the fact that water depths in the confidence region of GBL range from 50 and 200 m, while they vary between 20 m and 80 m in GSL; GBL therefore takes longer to lose its heat. Furthermore, FD mainly depends on air temperature variability after fall overturning which occurs at +4 ^{o}C.

Freezing Degree Days (FDD), calculated as the sum of mean daily air temperatures below 0 ^{o}C measured at a meteorological station, and given in the bottom left of **Figure 4.4** provide some indication of the effect of colder/warmer temperatures on FD. FDD calculated here between FO and ice-on date in each ice season. One should bear in mind, however, that heat storage during the preceding open water season will also have an impact on FD. After the overturning, however, the whole water column has the same temperature and FD will depend only on air temperature variability no matter what previous open water season was warmer or colder summer. Due to these, the relation between FDD and FD is not always consistent from year to year for the two lakes.

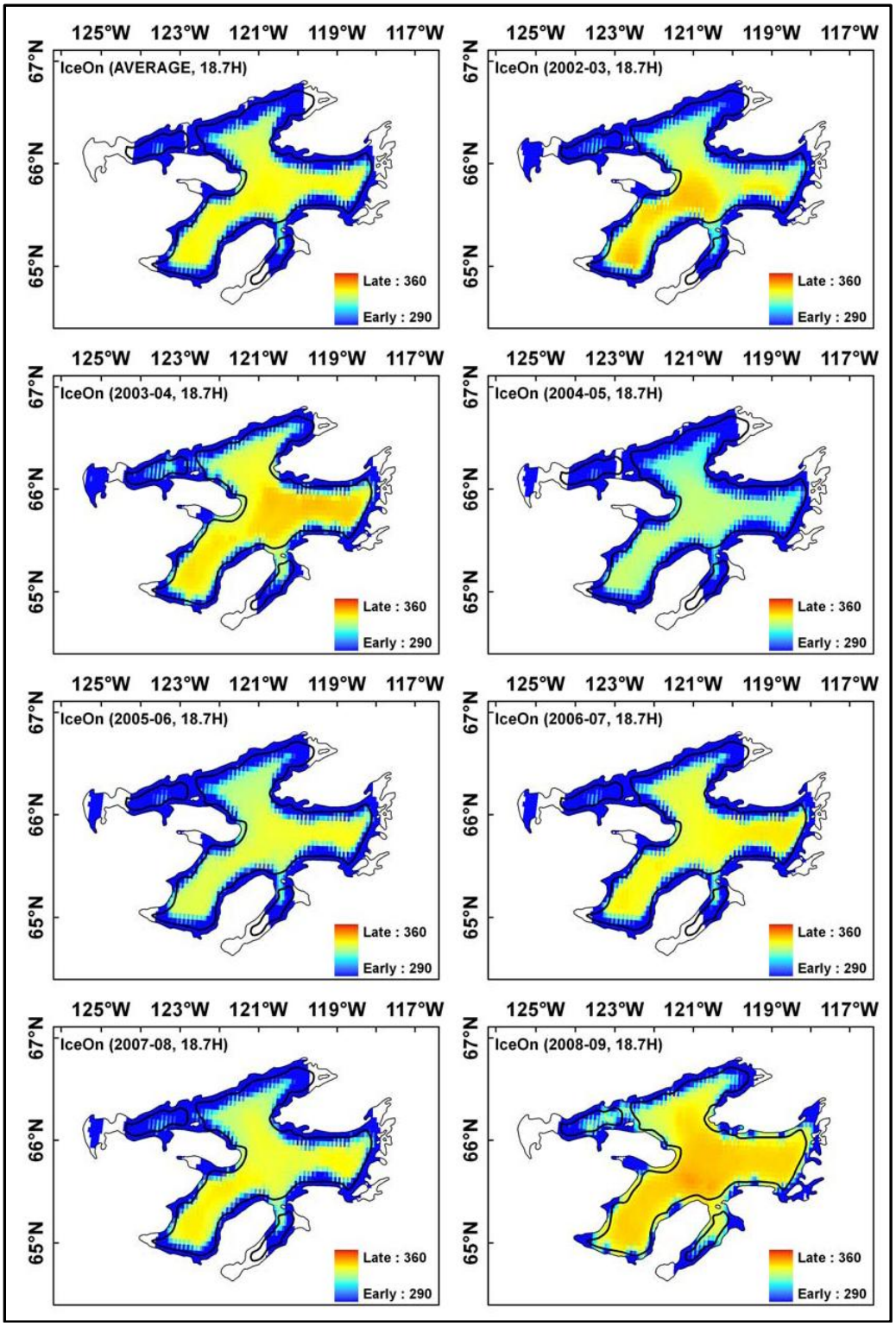

Figure 4.6: Ice-on over seven ice seasons (2002-2009) and average (top left panel) for GBL. Legend is day of year.

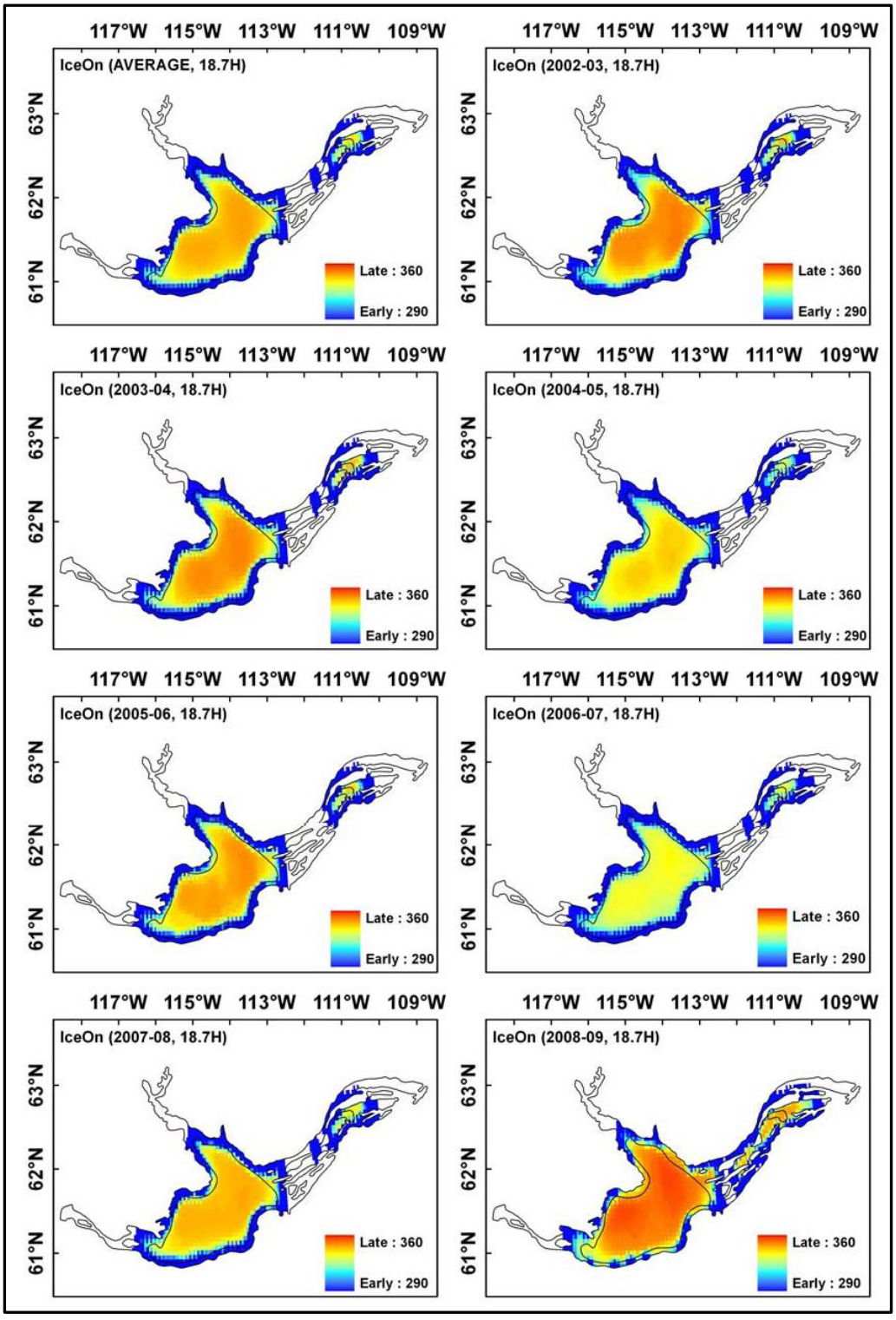

Figure 4.7: Ice-on over seven ice seasons (2002-2009) and average (top left panel) for GSL. Legend is day of year.

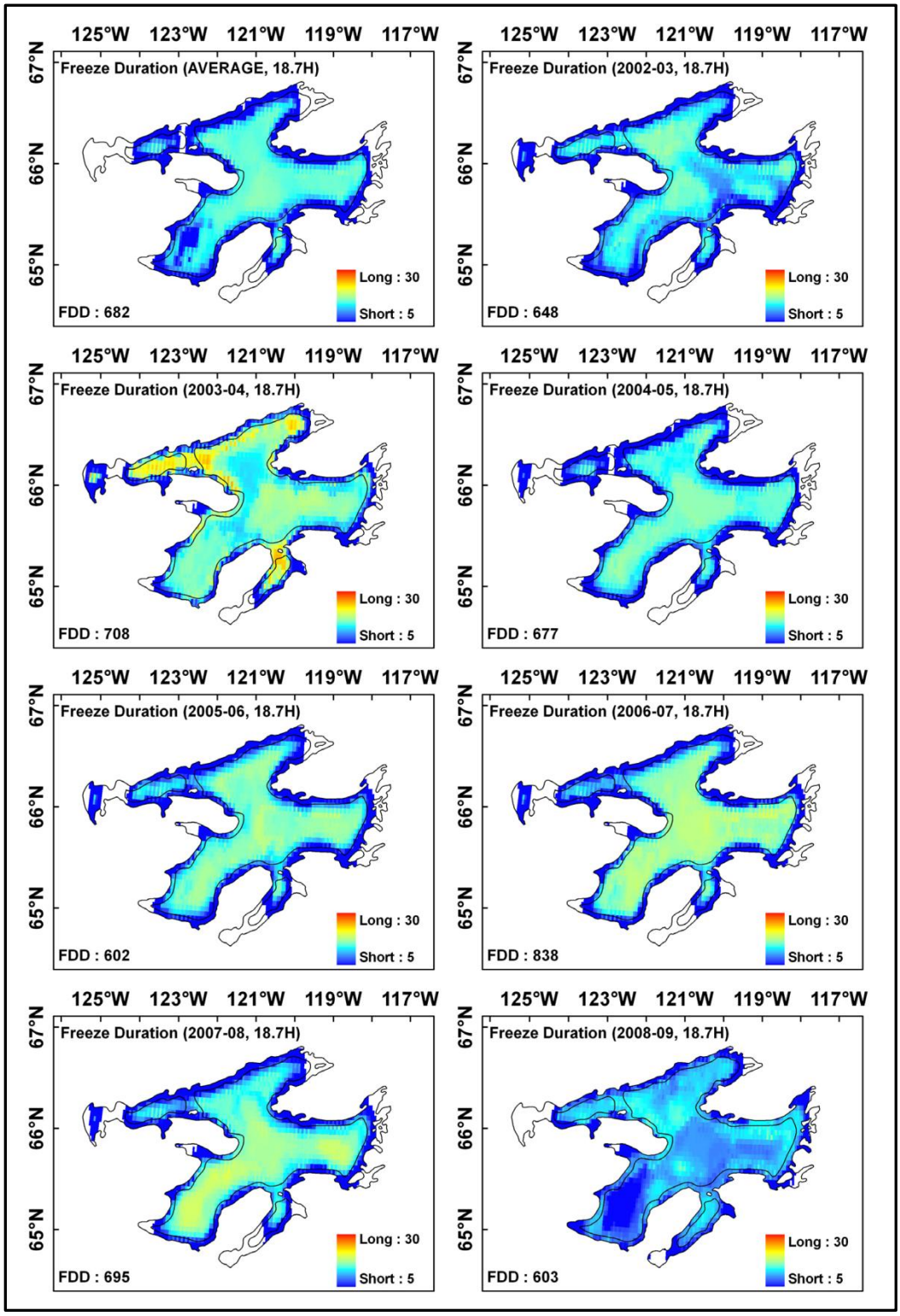

Figure 4.8: Freeze duration (FD) over seven ice seasons (2002-2009) and average (top left panel) for GBL. Legend is in number of days. Freezing Degree Days (FDD) in bottom left of each panel.

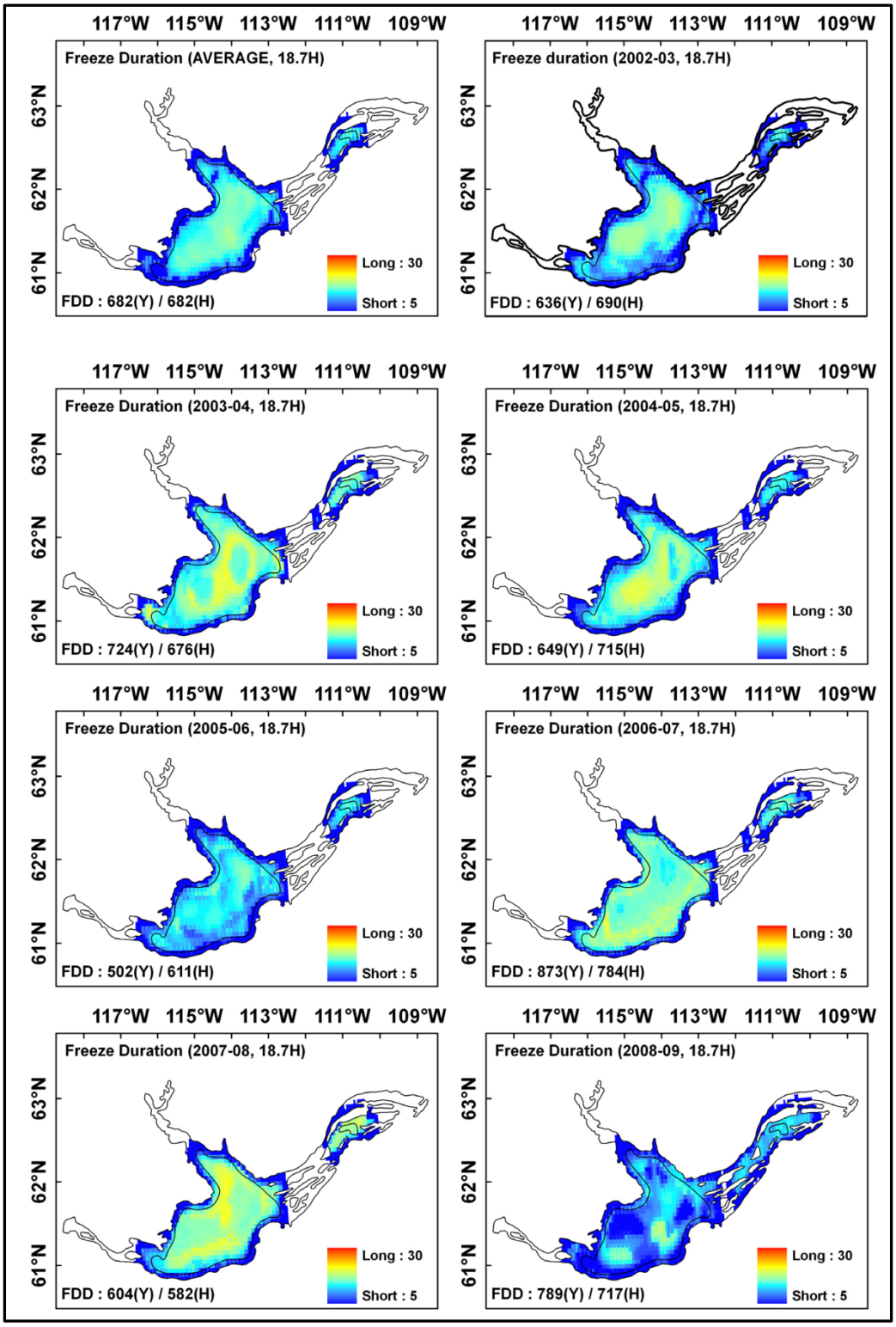

Figure 4.9: Freeze duration (FD) over seven ice seasons (2002-2009) and average (top left panel) for GSL. Legend is in number of days. Freezing Degree Days (FDD) in bottom left of each panel. Y: Yellowknife and H: Hay River.

4.6.1.2 Break-up period

The break-up process is primarily influenced by air temperature variability, causing earlier or later MO dates on the two lakes. The MO dates mark the beginning of melt of snow on the ice surface or the initiation of melt of ice in the case when a bare ice surface is encountered. Differences in the timing of MO between GBL and GSL can largely be explained due to spring air temperature differences (**Table 4.2**). MO dates occur approximately one week earlier on GSL than on GBL (**Table 4.4**). The average MO date occurs on DY 143 (end May) on GBL and DY 135 (mid May) on GBL (see **Figure 4.5**). For GBL, the earliest MO dates happened on DY 127 (2002-2003) and the latest MO dates occurred in 2003-2004 (DY 155, early June) (**Table 4.4**). For GSL, the earliest MO date occurred on DY 122 (early May) in 2005-2006 and the latest date took place in 2003-2004 (DY 150, early June). Earlier (later) MO dates appears to be related to warm (cool) spring air temperature (**Table 4.2**). The warmer average spring air temperature (-7.8 ^{o}C and -1.0 ^{o}C for GBL and GSL, respectively) caused earlier MO dates to occur in ice season 2005-2006, while the colder spring of ice season 2003-2004 (-11.7 ^{o}C and -7.6 ^{o}C for GBL and GSL, respectively) resulted in later MO dates.

Table 4.4: Summary of ice phenology variables during the break-up period (average day of melt-onset (MO) and ice-off, and number of days of melt duration (MD)) for GBL and GSL (2002-2009). Values within confidence regions in bold. Standard deviation in parentheses.

Year	MO		Ice-Off		MD	
	GBL	GSL	GBL	GSL	GBL	GSL
2002-03	133/**127** (14/**12**)	132/**137** (14/**5**)	193/**183** (14/**7**)	172/**157** (19/**2**)	61/**55** (15/**12**)	41/**19** (21/**4**)
2003-04	156/**155** (3/**2**)	147/**150** (16/**6**)	203/**198** (7/**4**)	186/**169** (20/**4**)	47/**43** (7/**4**)	39/**19** (19/**7**)
2004-05	133/**132** (11/**7**)	124/**131** (21/**17**)	193/**186** (11/4)	168/**155** (19/**4**)	60/**54** (13/**9**)	44/**24** (20/**17**)
2005-06	129/**128** (7/**4**)	119/**122** (9/**5**)	182/**169** (16/**5**)	161/**140** (21/**6**)	53/**41** (16/**7**)	42/**17** (22/**7**)
2006-07	142/**141** (10/**6**)	124/**129** (17/**6**)	197/**187** (12/**6**)	166/**153** (19/**5**)	55/**46** (13/**10**)	42/**24** (18/**6**)
2007-08	149/**152** (9/**9**)	133/**135** (16/**10**)	187/**183** (10/**4**)	170/**156** (20/**2**)	38/**31** (13/**8**)	37/**20** (20/**9**)
2008-09	167/**168** (8/**7**)	135/**137** (18/**14**)	200/**197** (6/**3**)	177/**167** (16/**3**)	33/**28** (10/**8**)	42/**30** (16/**12**)
Average	144/**143** (6/**3**)	131/**134** (12/**5**)	194/**186** (9/**3**)	171/**157** (17/**3**)	50/**43** (10/**5**)	41/**22** (17/**4**)

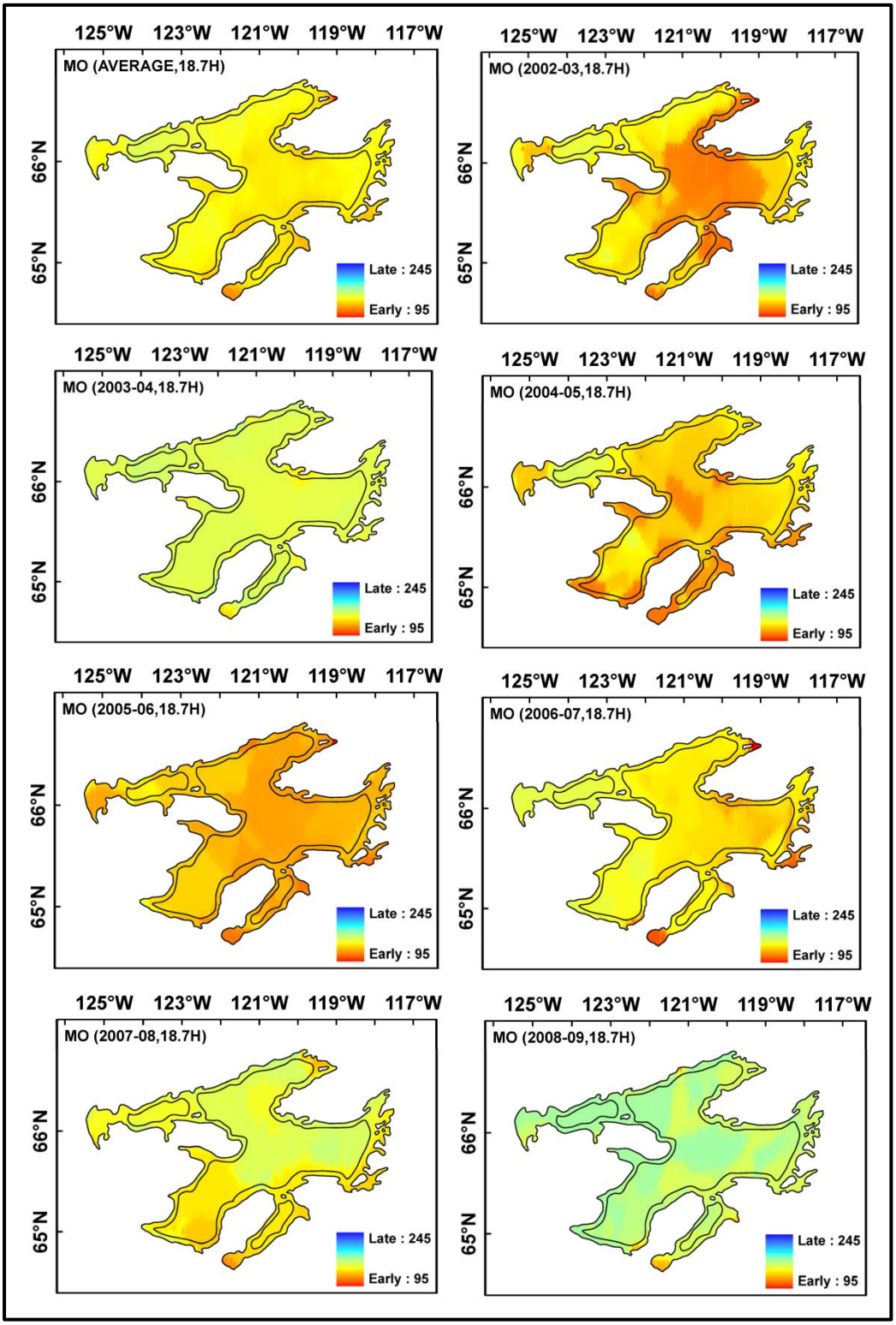

Figure 4.10: Melt-onset (MO) over seven ice seasons (2002-2009) and average (top left panel) for GBL. Legend is day of year.

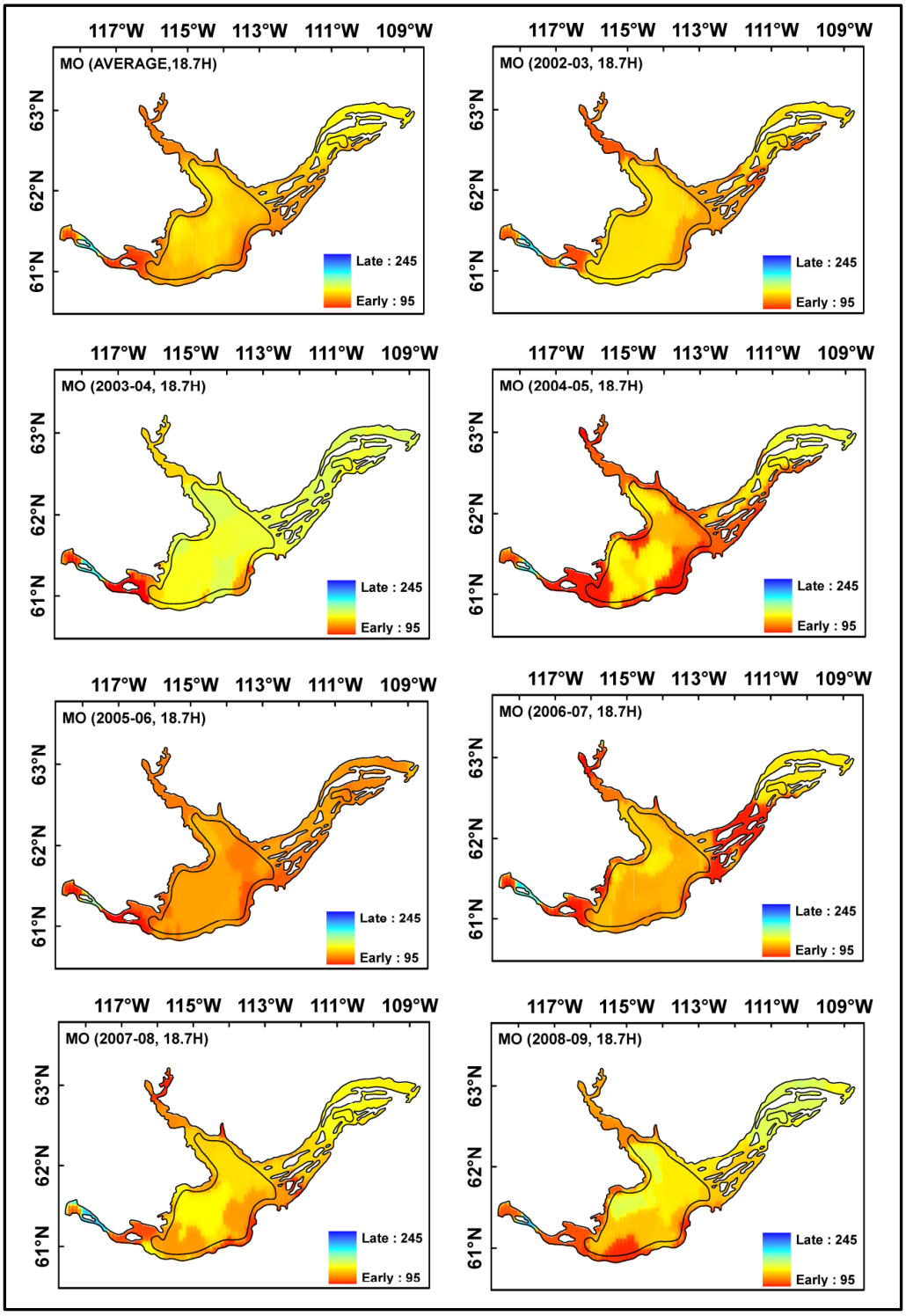

Figure 4.11: Melt-onset (MO) over seven ice seasons (2002-2009) and average (top left panel) for GSL. Legend is day of year.

In contrast to MO, the average ice-off dates on GSL are about four weeks earlier (DY 157 – early June) than on GBL (DY 183 – early July) (see **Figures 4.12 and 13**). For GBL, the latest ice-off date occurred during ice season 2003-2004 on DY 198 (mid July). The earliest ice-off date occurred in 2005-2006 on DY 169 (mid June) (**Table 4.4**). For GSL, the 2003-2004 ice season experienced the latest ice-off dates of DY 169 (mid June). The earliest ice-off date for this lake happened in 2005-2006 on DY 140 (mid May) (**Table 4.4**). Early ice-off dates lengthen the open water season during the high solar period in spring/summer, resulting in a longer period of solar radiation absorption by the lakes and, subsequently, higher lake temperatures in late summer/early fall due to larger heat storage. Looking at specific ice cover seasons, the colder spring/early summer climate conditions of 2004 and 2009 contributed to later break-up, while the warmest conditions of 2006 influenced earlier break-up (**Table 4.4**). On GSL, ice-off dates are earlier in the majority of years at the mouth of the Slave River which brings warmer water as this river flows from the south into the lake (see **Figure 4.5**). For GBL, however, ice-off dates are not influenced by similar river inflow such that melt generally proceeds gradually from the more southern (warmer) to the northern sections of the lake. Unlike MO, the larger difference in ice-off dates between the two lakes (about four weeks) can be explained by a combination of thicker ice and colder spring/early summer conditions at GBL which, as a result, requires a greater number of days above 0 ^{o}C to completely melt the ice.

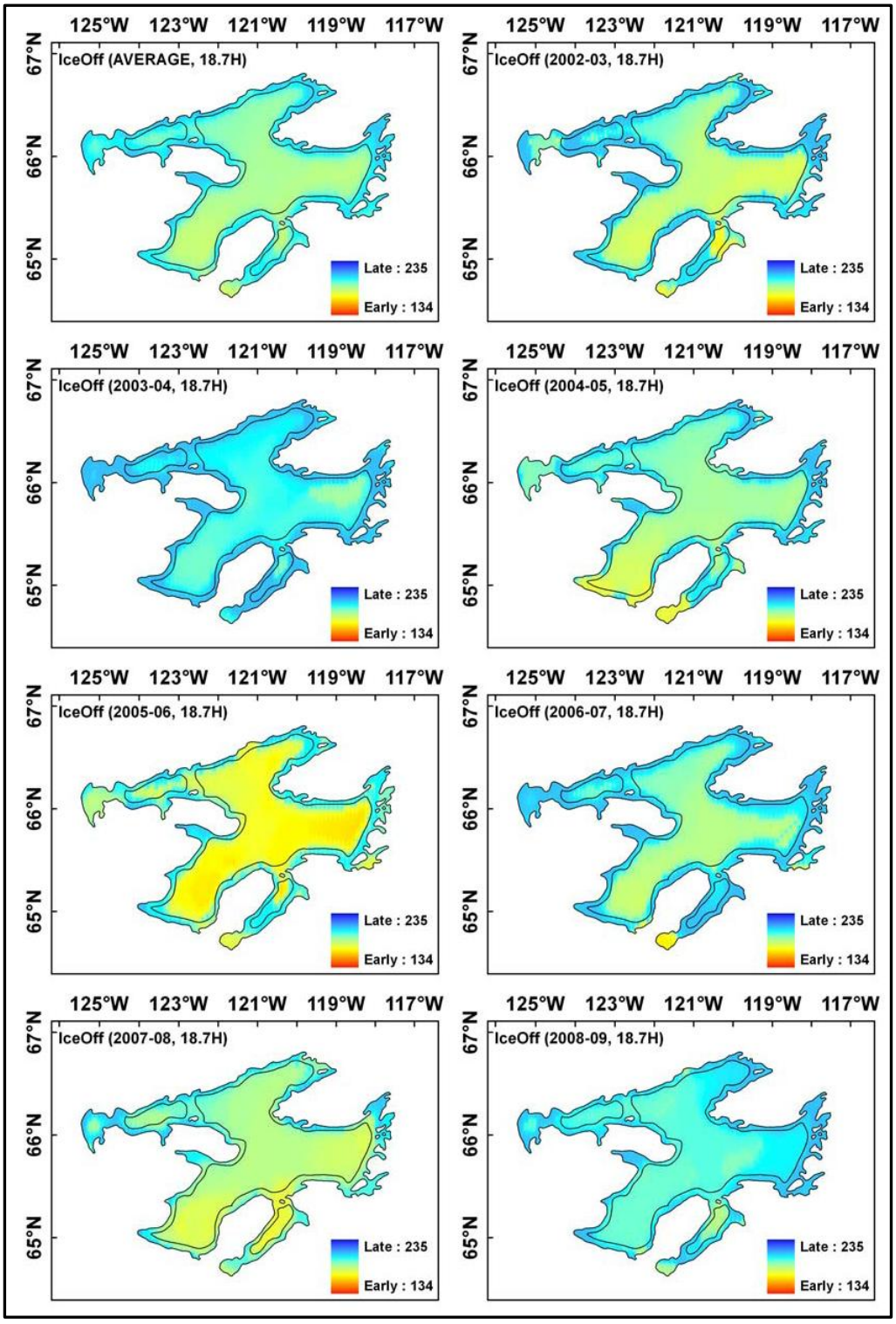

Figure 4.12: Ice-off over seven ice seasons (2002-2009) and average (top left panel) for GBL. Legend is day of year.

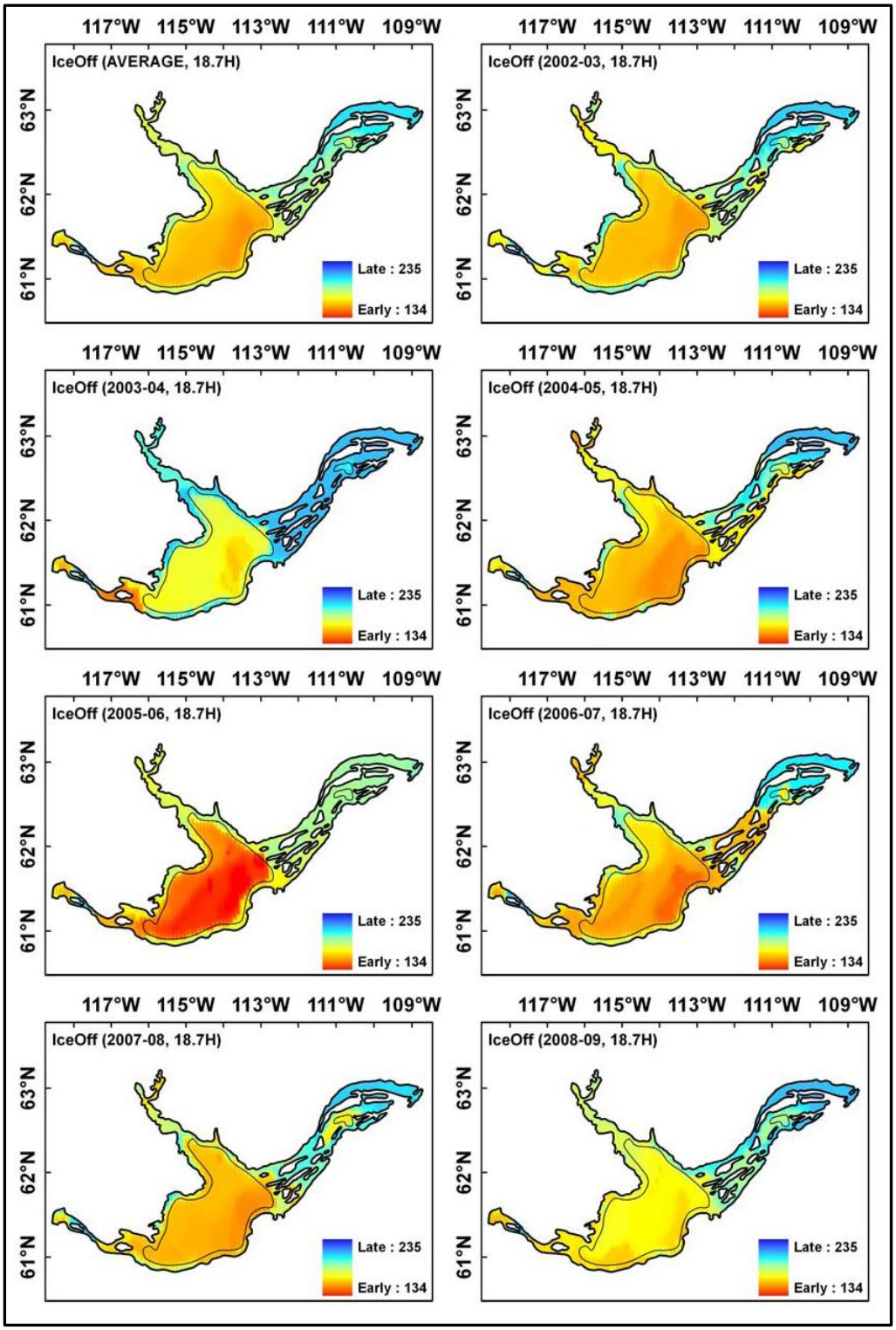

Figure 4.13: Ice-off over seven ice seasons (2002-2009) and average (top left panel) for GSL. Legend is day of year.

The average melt duration (MD), which encompasses the period from MO to ice-off, takes two to five weeks longer on GBL than on GSL **Table 4.4.** For GBL, the longest MD was 55 days in 2002-2003 but was only 28 days in 2008-2009 (**Table 4.4**). For GSL, the longest MD lasted 30 days in 2008-2009, whereas the shortest MD took 17 days in 2005-2006 (**Table 4.4**). The length of the MD is mainly controlled by the combination of end-of-winter maximum ice thicknesses and spring/early summer temperatures. In general, the thinner the ice is before melt begins and the warmer the temperature conditions are between MO and ice-off, the shorter the MD lasts. One exception is the central basin of GSL, where MD is also influenced by the inflow of water from Slave River which helps to accelerate the break-up process in this lake. Melting Degree Days (MDD), calculated as the sum of mean daily air temperatures above 0 ^{o}C at a meteorological station from MO until ice-off, provide some indication of the effect of colder/warmer temperatures in spring/early summer on MD for each ice season (see bottom left corner of **Figures 4.14 and 4.15**). Visually, a relation appears to exist between long/short MD and low/high MDD for GBL. Such a relation does not seem to be present for GSL, likely as a result of the inflow of water from Slave River.

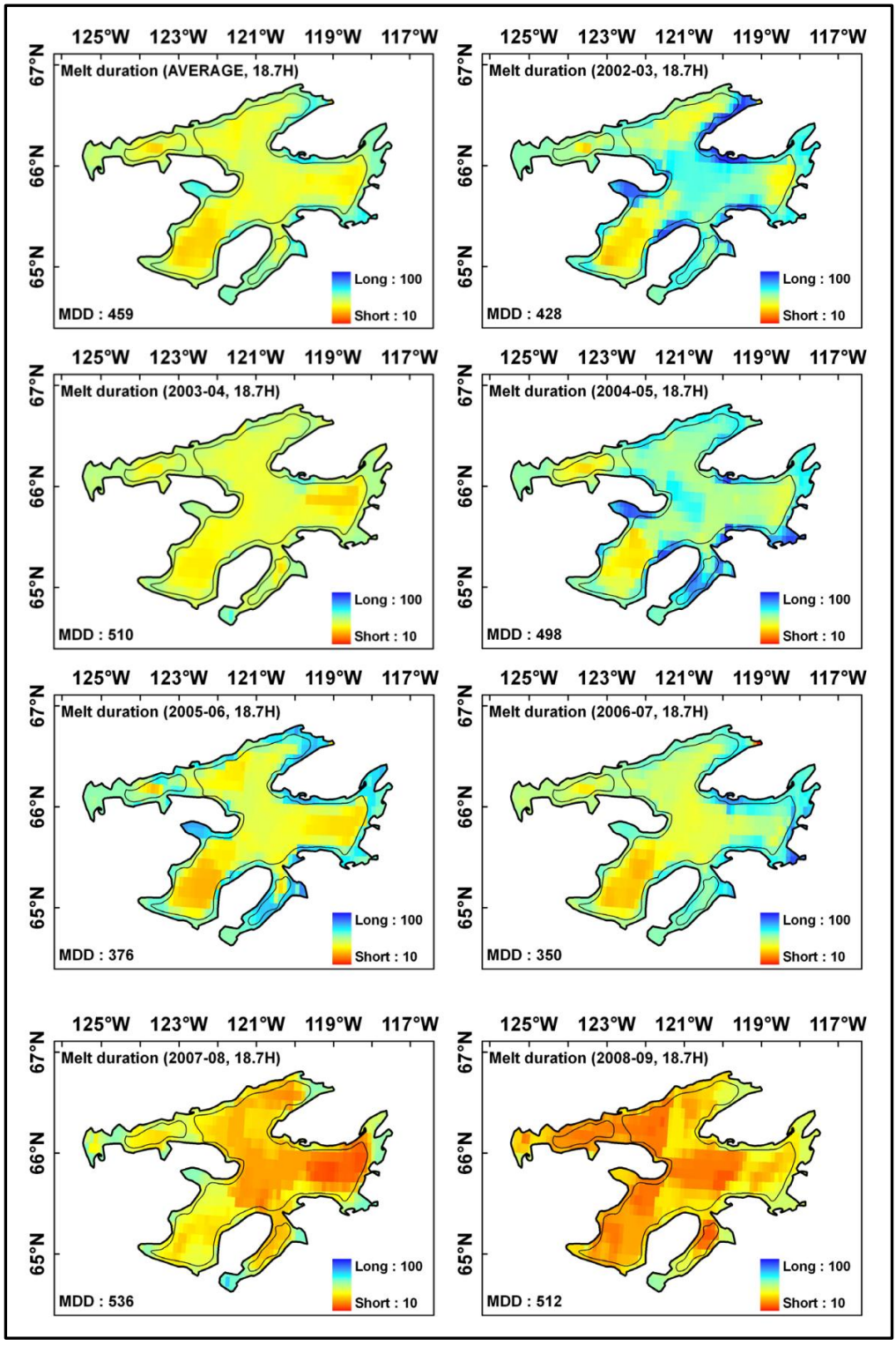

Figure 4.14: Melt duration (MD) over seven ice seasons (2002-2009) and average (top left panel) for GBL. Legend is in number of days. Melting Degree Days (MDD) in bottom left of each panel.

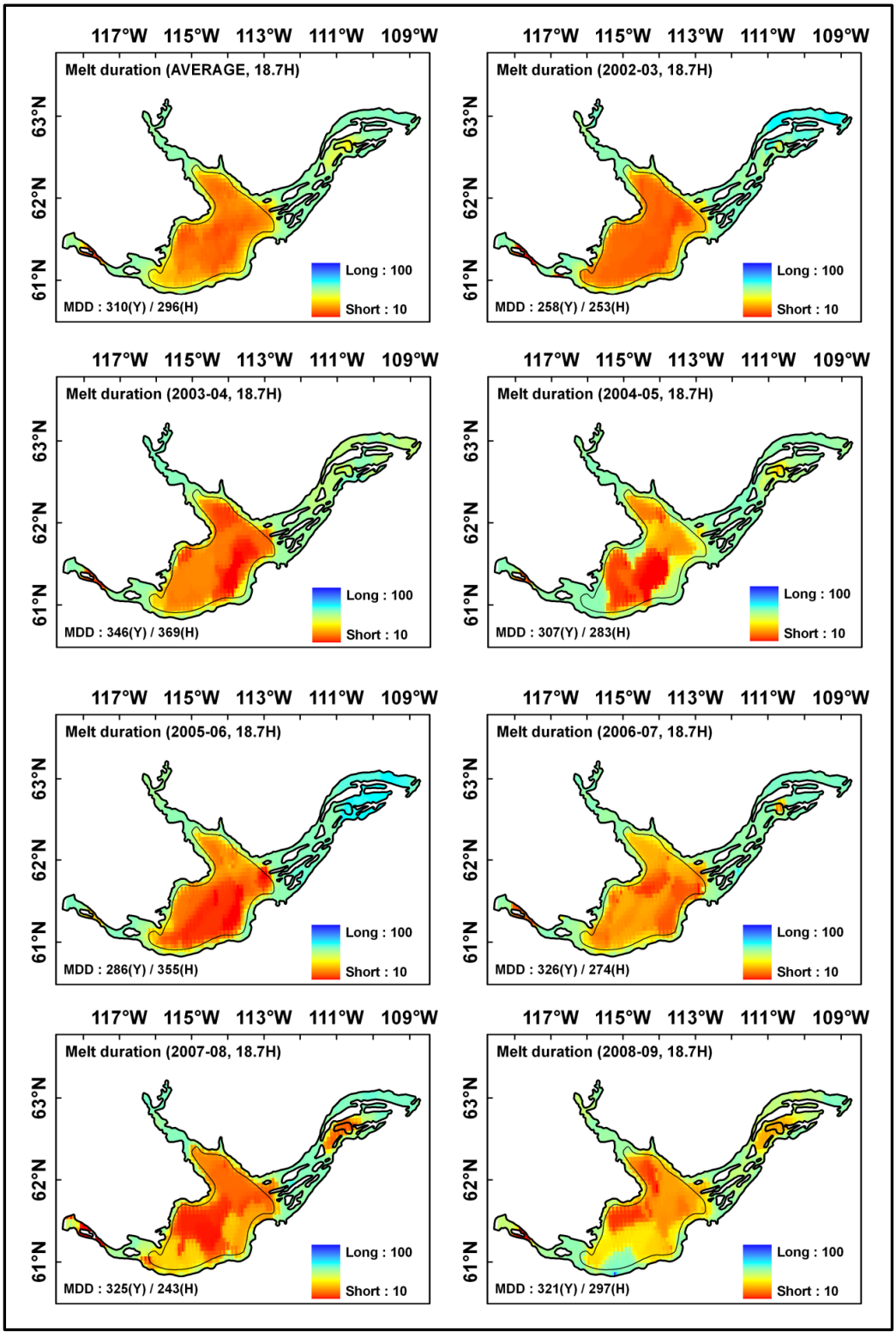

Figure 4.15: Melt duration (MD) over seven ice seasons (2002-2009) and average (top left panel) for GSL. Legend is in number of days. Melting Degree Days (MDD) in bottom left of each panel. Y: Yellowknife and H: Hay River.

4.6.1.3 Ice cover duration

The average ice cover duration (ICD), which is calculated as the number of days between ice-on and ice-off dates, is one week shorter for GSL than for GBL over the full period of analysis (DY 218 and 211 on average, respectively). However, the length of the ICD can differ by as much as four to five weeks between the two lakes in some years. For GBL, the longest ICD was 229 days in 2004-2005, while the shortest lasted 203 days (2005-2006). For GSL, the longest ICD lasted 223 days (2003-2004), while the shortest was 193 days (2007-2008) (**Table 4.5**). In GBL's Smith Arm and Dease Arm (northern section of lake), lake ice stays longer than in the other arms, up until the middle (or end) of July, particularly during the two cold winter seasons of 2003-2004 and 2008-2009 (**Figure 4.16**). For GSL, shorter ICD occurs at the mouth of Slave River and near Yellowknife compared to the east arm of the lake (**Figure 4.17**). ICD is influenced by river inflow from Slave River for the full period of study (2002-2009), as it has a particularly large influence on ice-off dates (see **Figure 4.13**).

Table 4.5: Summary of ice cover duration (ICDp) and open water season (OWS) (average number of days) for GBL and GSL (2002-2009). Values within confidence regions in bold. Standard deviation in parentheses. Note that OWS was not calculated for 2009 since it requires ice-on date to be known for fall freeze-up period 2009, which was not determined in this study.

Year	ICDp		Year	OWS	
	GBL	GSL		GBL	GSL
2002-03	224/**215** (19/**11**)	195/**220** (28/**29**)	2003	123/**116**(23/**22**)	151/**172** (28/**5**)
2003-04	233/**226** (12/**7**)	203/**223 (**22/**22)**	2004	102/**97**(13/**13**)	130/**154** (28/**6**)
2004-05	232/**229** (10/**7**)	195/**218 (**20/**22)**	2005	119/**112**(16/**16**)	155/**176** (27/**6**)
2005-06	210/**203** (15/**7**)	176/**201 (**26/**26)**	2006	136/**132**(21/**21**)	156/**177** (26/**7**)
2006-07	225/**217** (14/**8**)	195/**214** (17/**21**)	2007	117/**113** (17/**16**)	155/**172** (24/**7**)
2007-08	219/**215** (10/**6**)	184/**193** (12/**14**)	2008	134/**125** (20/**20**)	162/**186** (30/**6**)
2008-09	230/**223** (11/**5**)	193/**208** (18/**19**)			
Average	225/**218** (9/**6**)	192/**211** (16/**18**)	Average	122/**116** (15/**14**)	152/**173** (32/**5**)

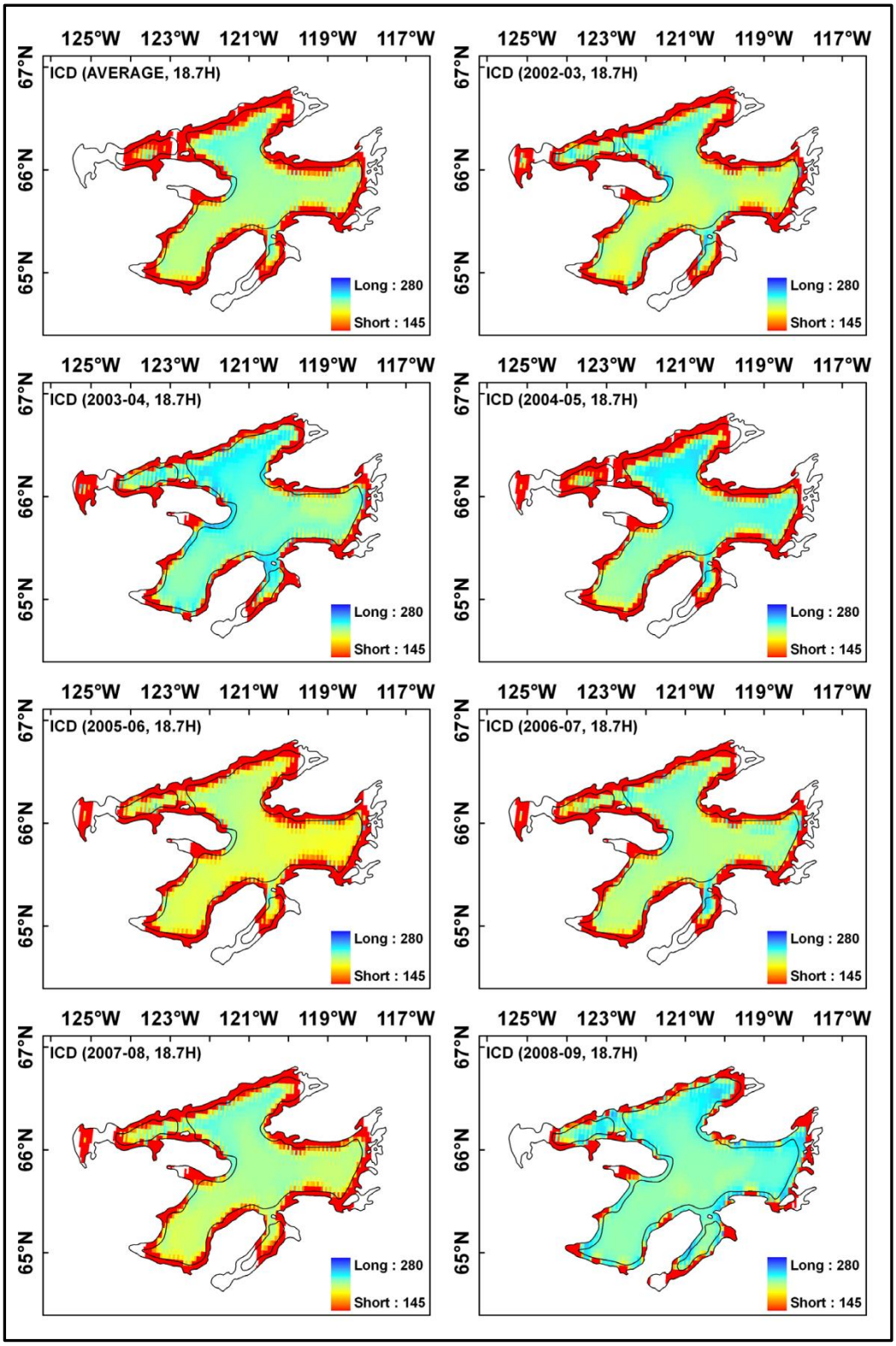

Figure 4.16: Ice cover duration (ICD) over seven ice seasons (2002-2009) and average (top left panel) for GBL. Legend is in number of days.

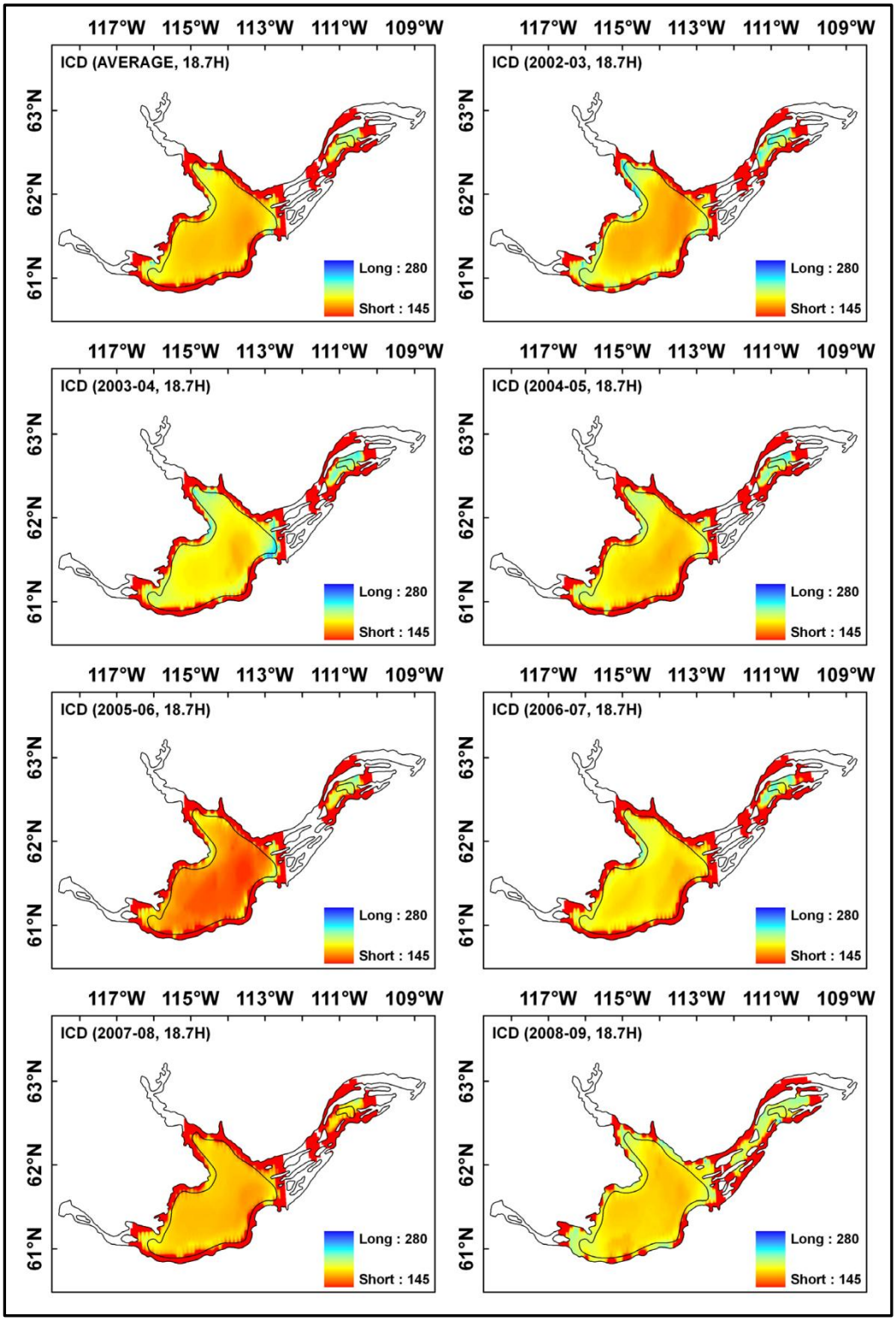

Figure 4.17: Ice cover duration (ICD) over seven ice seasons (2002-2009) and average (top left panel) for GSL. Legend is in number of days.

4.6.2 Comparison of AMSR-E ice phenology variables with other satellite-derived ice products

While the AMSR-E retrieval algorithm captures well the spatial patterns and seasonal evolution of ice cover on GBL and GSL over several ice seasons, estimated dates of the various ice phenology variables should be compared to those determined from other approaches and with different satellite sensors whenever possible, as to provide at least a qualitative assessment of the level of agreement with existing products. A detailed quantification of uncertainty (biases) of the various ice products is, however, beyond the scope of this paper. This is a topic that merits investigation in a follow-up study encompassing a larger number of lakes.

4.6.2.1 Comparison with other pixel-based products

Tables 4.6-4.8 present summary statistics of ice phenology variables estimated at the pixel level from AMSR-E T_B (2002-2009) against those obtained with daily QuikSCAT (2002-2006; Howell et al., 2009a) and NOAA/IMS products (2004-2009). Values in these tables are the averages and standard deviations calculated from all pixels over the complete lakes and their main basin (confidence regions). IMS ice variables consist of ice-on/ice-off dates and ICDp, while QuikSCAT-derived variables are comprised of FO/MO/ice-off dates and ICDp calculated from FO to ice-off dates. The complex nature of the freeze-up process has been reported to make the distinction between FO and ice-on dates difficult from analysis of the temporal evolution of backscatter (σ°) from QuikSCAT (Howell et al., 2009a). This can be explained by the fact that QuikSCAT-derived ice phenology variables are influenced by deformation features such as ice rafts, wind-roughened water in cracks, and ridge formation during the freeze-up period, acting to increase σ°. However, time series of AMSR-E T_B at 18.7 GHz (H-pol) can differentiate FO from ice-on dates (see **Figure 4.2**) as T_B is largely controlled by changes in emissivity progressively from the radiometrically cold open water to the warmer ice-covered lake surface, and not as much by lake ice surface roughness, during the freeze-up period.

FO dates as determined from AMSR-E are about one week earlier on average (7-11 days for GBL; 1-8 days for GSL) than those derived with QuikSCAT when considering the two lakes over the five years available for comparison (**Table 4.6**). AMSR-E T_B may be more sensitive to within-pixel fractional presence of ice and less to wind-induced surface roughness over open water areas than σ° from QuikSCAT. Regarding ice-on dates, AMSR-E (from DY 323 to 352) and IMS (from DY 319 to 338) show a difference of about one week on average, with AMSR-E detecting ice-on later. In fact, and as illustrated in **Figures 4.18-4.19**, NOAA/IMS ice-on patterns follow AMSR-E FO more closely than ice-on. Interestingly, IMS ice-on remains the same between DY 324 and DY 335 on GSL (**Figure 4.19**) while FO evolves over the same period in AMSR-E. This indicates that extensive cloud cover during this period may have been a limiting factor in determining the presence of ice and open water on GSL by ice analysts who largely rely on the use of optical satellite data in preparing the IMS product.

Table 4.6: Comparison of ice phenology variables for freeze-up period (FO and Ice-On) daily-derived from AMSR-E (AME), QuikSCAT (QUT) and NOAA/IMS (IMS) products for GBL and GSL (2002-2009). Values within confidence regions in bold. Standard deviation in parentheses.

Pixel Level	FO				Ice-On			
	GBL		GSL		GBL		GSL	
YEAR	AME	QUT	AME	QUT	AME	IMS	AME	IMS
0203	311/**320** (14/**7**)	**330** **(8)**	318/**331** (18/**4**)	**335** **(8)**	328/**333** (11/**7**)		334/**345** **(**17/**7**)	
0304	313/**322** (11/**5**)	**309** **(9)**	319/**329** (14/**5**)	**332** **(8)**	332/**337** (8/**5**)		338/**345** (11/**5**)	
0405	303/**308** (9/**4**)	**314** **(6)**	313/**322** (13/**3**)	**325** **(8)**	321/**323** (6/**4**)	316/**322** (9/**8**)	331/**338** (12/**4**)	315/**319** (9/**8**)
0506	309/**314** (9/**4**)	**321** **(9)**	320/**332** (15/**4**)	**333** **(6)**	326/**330** (8/**4**)	319/**322** (11/**10**)	337/**344** (12/**4**)	327/**330** (10/**10**)
0607	312/**317** (9/**3**)	**325** **(6)**	310/**316** (9/**5**)	**324** **(5)**	331/**335** (7/**3**)	327/**332** (14/**7**)	328/**332** (8/**3**)	327/**331** (10/**9**)
0708	311/**316** (8/**3**)		318/**326** (10/**4**)		329/**333** (8/**4**)	325/**329** (13/**9**)	338/**343** (9/**4**)	328/**338** (16/**15**)
0809	320/**330** (13/**6**)		330/**342** (15/**6**)		334/ **340** (8/**4**)	323/**329** (12/**12**)	344/**352** (12/**3**)	328/**338** (14/**11**)
AVG	311/**318** (11/**4**)		318/**328** **(**11/**3**)		329/**333** (6/**4**)	322/**327** (12/**9**)	336/**343** (9/**4**)	325/**331** (12/**11**)

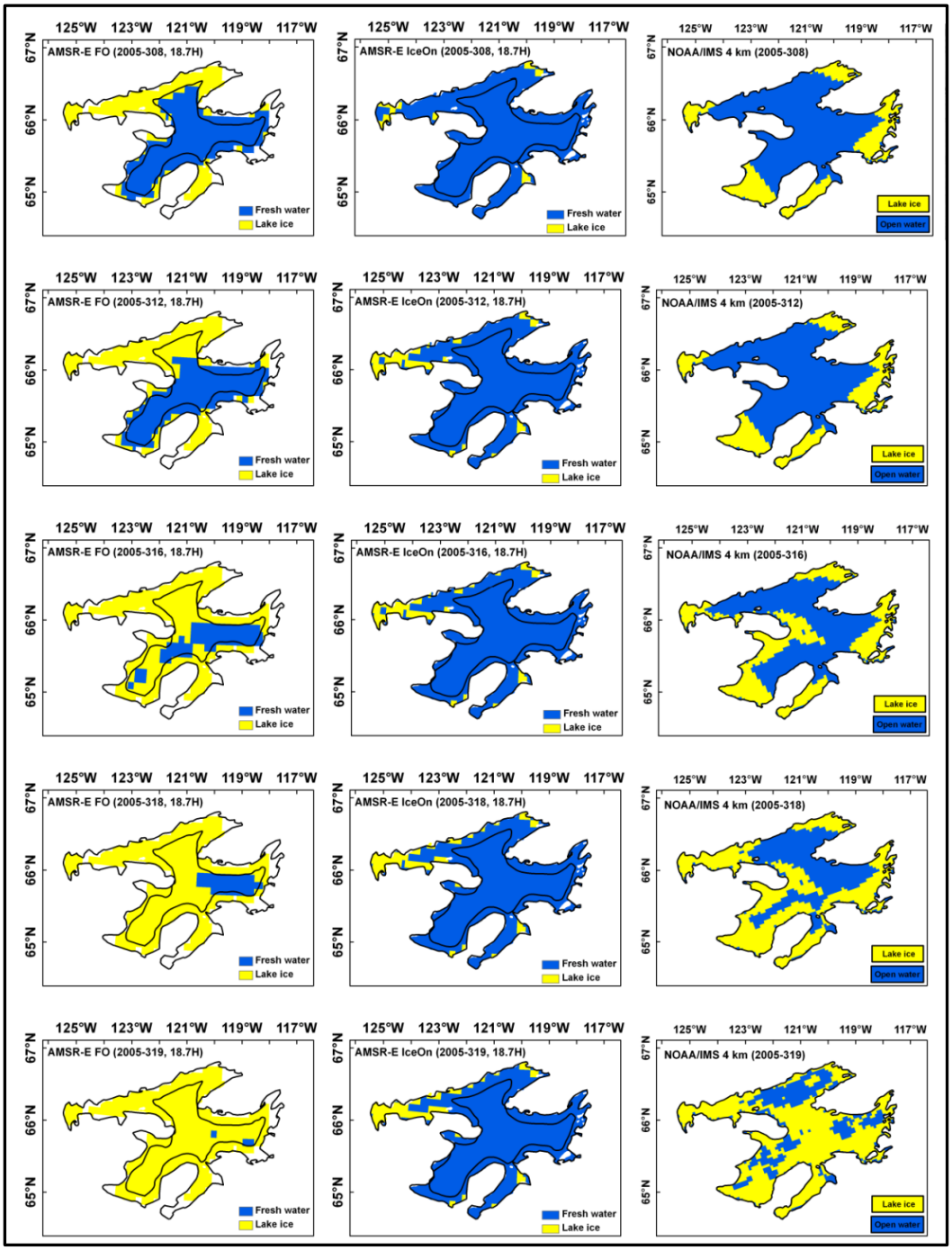

Figure 4.18: Comparison of AMSR-E freeze-onset (left), ice-on (center), and NOAA/IMS ice-on (right) (day of year) during the freeze-up period of ice season 2005-2006 on GBL.

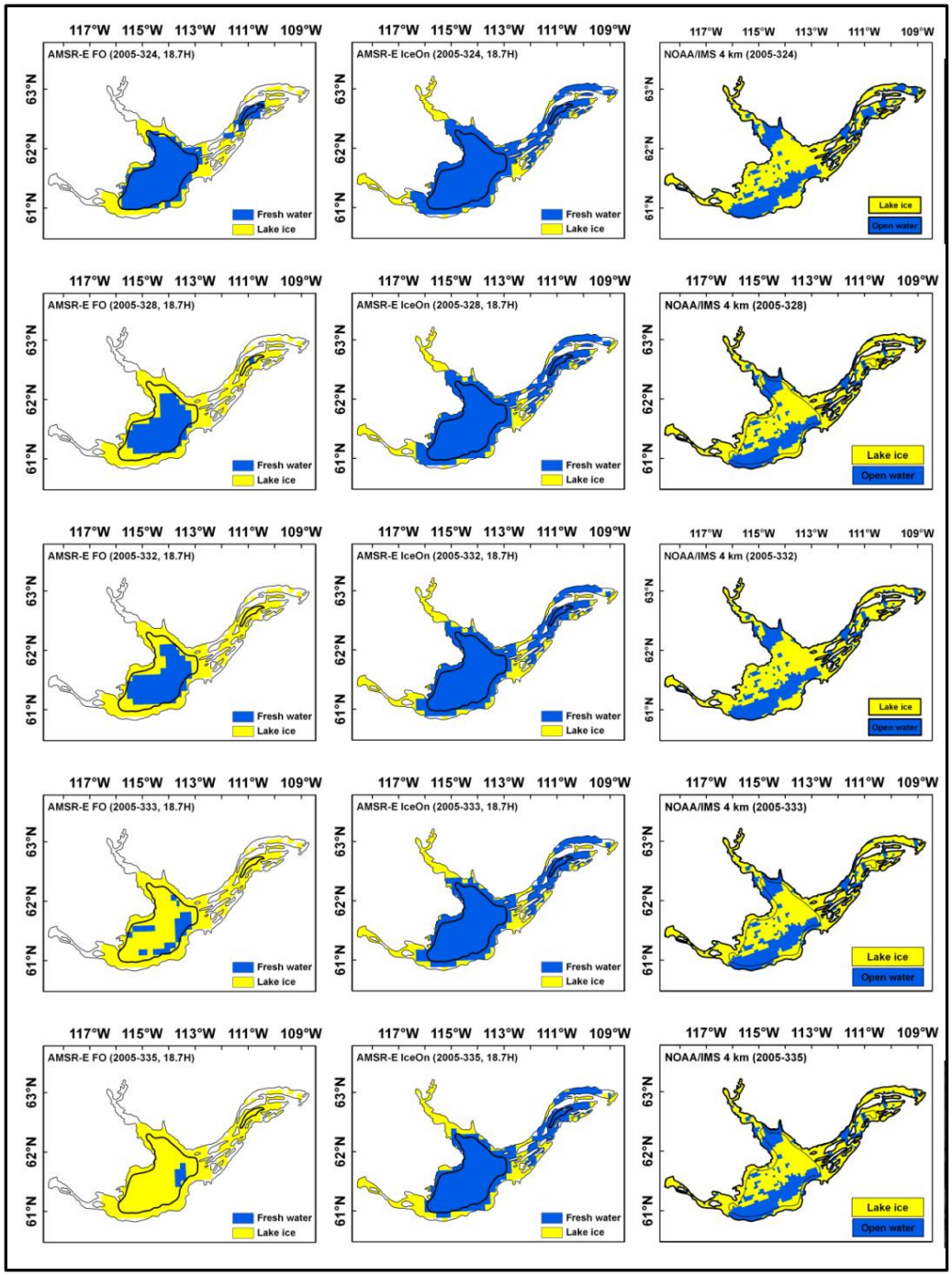

Figure 4.19: Comparison of AMSR-E freeze-onset (left), ice-on (center), and NOAA/IMS ice-on (right) (day of year) during the freeze-up period of ice season 2005-2006 on GSL.

The difference in MO dates is very variable between AMSR-E and QuikSCAT, ranging anywhere between a single day to four weeks (**Table 4.7**). During the break-up period, σ° seems more sensitive to initial surface melt than T_B with QuikSCAT providing in all but one case earlier MO. AMSR-E (from DY 140 to 198) and QuikSCAT ice-off dates (from DY 151 to 205) show similar inter-annual variability with a difference of about one week (**Table 4.7**). Average ice-off dates are also quite similar between AMSR-E and IMS with a difference of approximately five days. They also follow the same variability (later and earlier dates) between years. Although the number of years in this comparison between products is somewhat limited, these initial results suggest that ice-on is the most consistent ice phenology variable across products examined. This point is further supported by the similar spatial patterns in ice-on/ice-off determined from AMSR-E, IMS, and MODIS imagery over the break-up period of ice season 2005-2006 (**Figures 4.20 and 4.21**).

Table 4.7: Comparison of ice phenology variables for break-up period (MO and Ice-Off) daily-derived from AMSR-E (AME), QuikSCAT (QUT) and NOAA/IMS (IMS) products for GBL and GSL (2002-2009). Values within confidence regions in bold. Standard deviation in parentheses.

Pixel Level	MO				Ice-Off					
	GBL		GSL		GBL			GSL		
YEAR	AME	QUT	AME	QUT	AME	QUT	IMS	AME	QUT	IMS
0203	133/**127** (14/**12**)	**117** **(8)**	132/**137** (14/**5**)	**112** **(5)**	193/**183** (14/7)	**189** **(6)**		172/**157** (19/**2**)	**163** **(6)**	
0304	156/**155** (3/**2**)	**149** **(2)**	147/**150** (16/**6**)	**143** **(8)**	203/**198** (7/**4**)	**205** **(3)**	202/**204** (8/**6**)	186/**169** (20/**4**)	**178** **(5)**	176/**174** (17/**14**)
0405	133/**132** (11/**7**)	**152** **(14)**	124/**131** (21/**17**)	**100** **(1)**	193/**186** (11/4)	**193** **(5)**	188/**188** (12/**7**)	168/**155** (19/**4**)	**164** **(7)**	166/**160** (12/**10**)
0506	129/**128** (7/**4**)	**127** **(10)**	119/**122** (9/**5**)	**118** **(16)**	182/**169** (16/**5**)	**174** **(5)**	171/**172** (12/**10**)	161/**140** (21/**6**)	**151** **(11)**	148/**145** (13/**10**)
0607	142/**141** (10/**6**)		124/**129** (17/**6**)		197/**187** (12/**6**)		187/**187** (13/**9**)	166/**153** (19/**5**)		159/**158** (14/**6**)
0708	149/**152** (9/**9**)		133/**135** (16/**10**)		187/**183** (10/**4**)		185/**188** (9/**7**)	170/**156** (20/**2**)		161/**159** (13/**5**)
0809	167/**168** (8/**7**)		135/**137** (18/**14**)		200/**197** (6/**3**)		198/**200** (12/**5**)	177/**167** (16/**3**)		175/**174** (19/**7**)
AVG	144/**143** (6/**3**)		131/**134** (12/**5**)		194/**186** (9/**3**)		189/**190** (11/**7**)	171/**157** (17/**3**)		164/**162** (15/**9**)

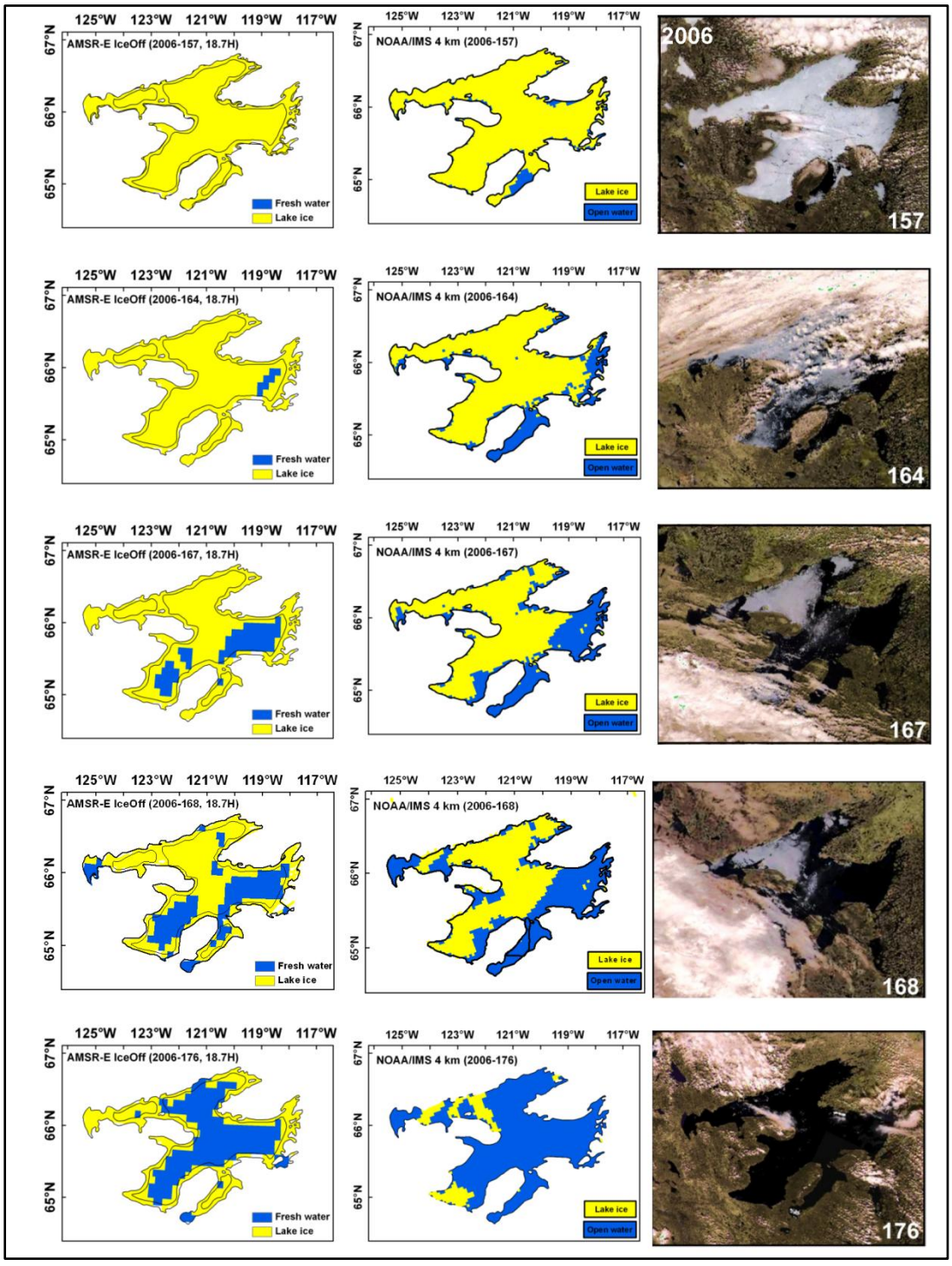

Figure 4.20: Comparison of AMSR-E (left) and NOAA/IMS (center) ice-off, and MODIS/Terra image (right) acquired on the same day during the break-up period of ice season 2005-2006 on GBL.

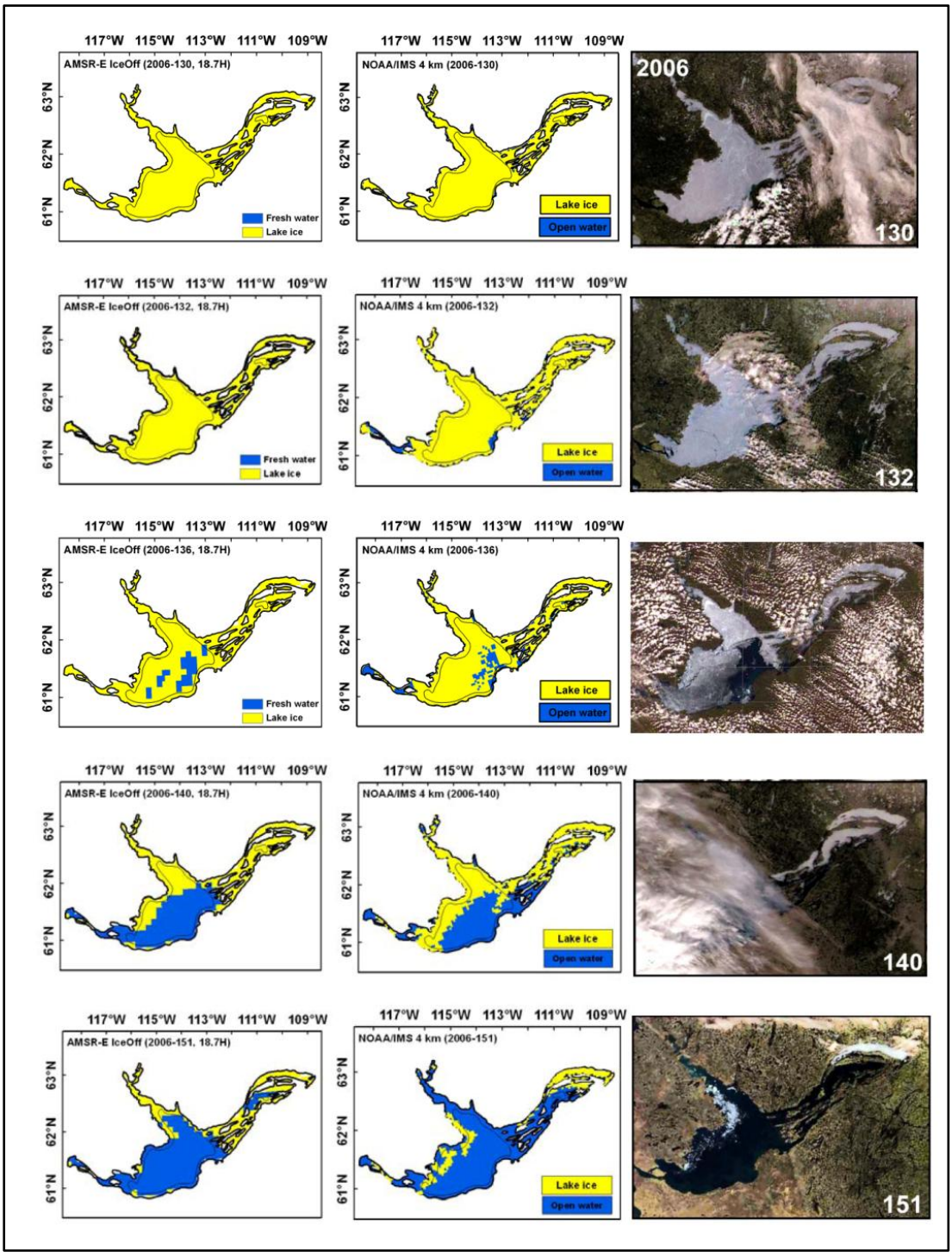

Figure 4.21: Comparison of AMSR-E (left) and NOAA/IMS (center) ice-off, and MODIS/Terra image (right) acquired on the same day during the break-up period of ice season 2005-2006 on GSL.

AMSR-E ICDp differs by one week on average from IMS (**Table 4.8**). Ice cover is estimated to remain longer with IMS when examining the full extent of GBL and GSL. This is expected since IMS is a finer resolution product (4 km) that can resolve ice in areas of the lakes where AMSR-E suffers from land contamination (along lake shore and areas with small islands as in the east arm of GSL). When considering only the main basin sections of GBL and GSL (confidence regions), AMSR-E ICDp estimates are slightly shorter for GBL and longer for GSL than IMS (**Table 4.8**). Since ICDp is calculated from ice-on to ice-off dates such differences between the two products are possible. As indicated earlier, ice-on dates from IMS tend to fall between FO and ice-on dates from AMSR-E, but closer to FO. Differences in ICDp tend to be larger between AMSR-E and QuikSCAT estimates over two lakes, the main reason being that ICDp from QuikSCAT was calculated from FO, instead of ice-on to ice-off dates by Howell et al. (2009a). This makes the comparison a bit more tentative than with the IMS product.

Table 4.8: Comparison of daily-derived ICDp from AMSR-E (AME), QuikSCAT (QUT) and NOAA/IMS (IMS) products for GBL and GSL (2002-2009). Values within confidence regions in bold. Standard deviation in parentheses. Note that QUT* indicates that ICDp was calculated from FO to ice-off since ice-on was not determined in Howell et al. (2009).

Pixel Level	ICDp					
	GBL			GSL		
YEAR	AME	QUT*	IMS	AME	QUT*	IMS
0203	224/**215** (19/**11**)	**224** **(13)**		195/**220** (28/**29**)	**193** **(12)**	
0304	233/**226** (12/**7**)	**260** **(11)**		203/**223** **(**22/**22)**	**211** **(12)**	
0405	232/**229** (10/**7**)	**245** **(9)**	238/**232** (11/**7.5**)	195/**218** **(**20/**22)**	**205** **(14)**	217/**207** (11/9)
0506	210/**203** (15/**7**)	**218** **(13)**	217/**216** (12/**10**)	176/**201** **(**26/**26)**	**183** **(16)**	186/**181** (12/10)
0607	225/**217** (14/**8**)		225/**221** (14/**8**)	195/**214** (17/**21**)		197/**193** (12/7.5)
0708	219/**215** (10/**6**)		225/**225** (11/**8**)	184/**193** (12/**14**)		198/**187** (15/10)
0809	230/**223** (11/**5**)		241/**237** (12/**8.5**)	193/**208** (18/**19**)		213/**202** (17/9)
AVG	225/**218** (9/**6**)		229/**226** (12/**8.3**)	192/**211** (16/**18**)		202/**194** (13/9.6)

4.6.2.2 Lake-wide comparison

Table 4.9 shows summary statistics of CFO, WCI and ICDe estimated with AMSR-E compared to those determined from NOAA/IMS and by CIS. CFO corresponds to the date when all pixels within a lake or lake section become totally ice-covered (i.e. 100% ice fraction), while WCI is the date when all pixels become ice-free (i.e. 100% open water). ICDe is calculated as the number of days between CFO and WCI. In **Table 4.9**, CFO/WCI/ICDe estimates from IMS and CIS are for the entire extent of GBL and GSL. Acknowledging that estimates of the same variables are derived at a coarser spatial resolution with AMSR-E, estimates are provided for both the entire lake surfaces and main basins only (confidence regions) of GBL and GSL. Also noteworthy is the fact that CIS is a weekly product, unlike the IMS and AMSR-E products that are derived daily. Therefore, some of the differences between estimated dates may be attributed to the temporal resolution of the products. AMSR-E/CFO (from DY 330 to 356) dates compare well with CIS/CFO (from DY 324 to 354) and IMS/CFO (from DY 326 to 348), as do AMSR-E/WCI (from DY 158 to 210) with IMS/WCI (from DY 175 to 209) and CIS/WCI (from DY 165 to 219). Overall, these results are very encouraging since CFO/WCI/ICDe estimated with the new automated AMSR-E ice phenology retrieval algorithm are within about one week of those determined by ice analysts (IMS and CIS) through visual interpretation of imagery from various sources (optical and SAR). Some of the variability in estimates between years (earlier/later dates) should, however, be examined more closely in a follow-up study.

Table 4.9: Comparison of ice phenology variables (CFO, WCI, and ICDe) daily derived from AMSR-E (AME) and NOAA/IMS (IMS) products, as well as weekly-derived from Canada Ice Service (CIS) product for GBL and GSL (2002-2009). Values within confidence regions in bold. Standard deviation in parentheses.

Entire Lake	CFO						WCI						ICDe					
	GBL			GSL			GBL			GSL			GBL			GSL		
YEAR	AME	IMS	CIS	AME	IMS	CIS	AME	IMS	CIS	AME	IMS	CIS	AME	IMS	CIS	AME	IMS	CIS
0203	346 /**346**		354	351 /**351**		354	210/ **210**		199	210 /**160**		178	229/ **229**		203	224 /**174**		182
0304	344 /**344**		339	350 /**350**		346	210 /**210**	208	219	210 /**194**	202	198	231 /**231**		238	225 /**209**		210
0405	330 /**330**	326	324	344 /**344**	326	338	210 /**210**	209	203	210 /**166**	186	196	246 /**246**	249	237	232 /**188**	226	216
0506	336 /**336**	334	336	349 /**349**	340	343	210 /**202**	187	188	207 /**168**	183	165	239 /**231**	218	210	223 /**184**	208	182
0607	339 /**339**	336	335	337 /**337**	337	335	210 /**208**	202	201	210 /**164**	175	187	236 /**234**	231	224	238 /**192**	203	210
0708	339 /**339**	345	341	346 /**346**	342	341	210 /**193**	195	200	210 /**158**	189	200	236 /**219**	215	217	230 /**178**	212	217
0809	348 /**348**	331	333	356 /**356**	348	347	210 /**204**	208	212	210 /**172**	199	191	228 /**222**	243	237	219 /**181**	217	202
AVG	340 /**340** (6/**6**)	334 (7)	337 (9)	348 /**347** (6/**6**)	339 (8)	343 (6)	210 /**203** (0/**6**)	202 (9)	203 (10)	210 /**164** (1/**11**)	189 (10)	188 (13)	234 /**230** (6/**9**)	231 (15)	224 (14)	227 /**187** (6/**12**)	213 (9)	203 (15)

4.7 Conclusion

The 18.7 GHz (H-pol) was found to be the most suitable AMSR-E channel for estimating ice phenology dates. It is less sensitive than the other frequencies examined to wind effects over open water and H-pol is better than V-pol for discriminating open water from ice. As a result, an ice phenology retrieval algorithm which makes use of AMSR-E 18.7 GHz H-pol T_B data was developed and applied to map the evolution of freeze-onset/melt-onset and ice-on/ice-off dates, as well as melt/freeze/ice cover duration on GBL and GSL over seven ice seasons (2002-2009). Through this, much was learned about the temporal and spatial evolution of ice cover within and between the two large lakes in relation to regional climate, latitudinal position, spring and summer temperature (for break-up), lake depth and, in the case of GSL, the influence of water inflow from Slave River. In addition, freeze duration is mainly dependent on air temperature variability after fall overturning. Results revealed that during the freeze-up period both freeze-onset and ice-on dates occur about one week earlier, and freeze duration lasts approximately one week longer on GBL than on GSL. During the break-up period, melt-onset and ice-off dates happen on average one week and

approximately four weeks later, respectively, on GBL. Located in a colder climate region, melt duration lasts about three weeks longer on this lake compared to its southern counterpart. The net effect is that ice cover duration is usually three to four weeks longer, depending on the ice season, on GBL compared to GSL. These results add to our knowledge of ice phenology on the two lakes which had not been fully documented and contrasted in previous investigations.

Results from an initial comparison between AMSR-E estimated ice phenology variables and those estimated by QuikSCAT, as well as those obtained from NOAA IMS and CIS show that relatively coarse resolution AMSR-E 18.7 GHz H-pol T_B data are suitable for monitoring of ice phenology on the two lakes, at least in their main basins in a consistent manner. The ice phenology algorithm described in this paper may be applicable to other large lakes of the Northern Hemisphere and also to longer time series of passive microwave satellite data from SMMR-SSM/I (circa 32-year historical record). Furthermore, there is likely the potential to estimate ice concentration during freeze-up and break-up from AMSR-E measurements. These are three lines of research that we are actively pursuing.

Chapter 5: Sensitivity of AMSR-E Brightness Temperatures to the Seasonal Evolution of Lake Ice Thickness

In this chapter, the sensitivity of brightness temperature (T_B) at 6.9, 10.7, and 18.7 GHz from Advanced Microwave Scanning Radiometer–Earth Observing System (AMSR-E) observations was investigated over five winter seasons (2002-2007) on Great Bear Lake (GBL) and Great Slave Lake (GSL), Northwest Territories, Canada. The T_B measurements were compared to ice thicknesses obtained with a previously validated thermodynamic lake ice model. Lake ice thickness was found to explain much of the increase of T_B at 10.7 and 18.7 GHz. T_B acquired at 18.7 GHz (V-pol) and 10.7 GHz (H-pol) showed the strongest relation with simulated lake ice thickness over the period of study ($R^2 > 0.90$). A comparison of the seasonal evolution of T_B for a cold winter (2003-2004) and a warm winter (2005-2006) revealed that the relationship between T_B and ice growth was stronger in the cold winter (2003-2004). Overall, this chapter shows the high sensitivity of T_B to ice growth and thus the potential of AMSR-E mid-frequency channels to estimate ice thickness on large northern lakes.

5.1 Introduction

Lake ice grows steadily between the end of the freeze-up period and the onset of the break-up period as a result of the thermodynamics of freezing water and dynamic ice motion on the surface. Lake ice thickens as a result of two fundamental formation processes i) black ice (congelation ice) is created by the heat transfer of freezing water at the ice-water interface, and ii) snow ice is created by the freezing of slush at the snow-ice interface.

Negative temperature gradients in the ice and snow (for black ice) and snow alone (for snow ice) cause conductive heat flow through the insulating ice layer into the subzero

atmosphere (Jeffries et al., 2006). In thermodynamic thickening, this conductive heat flow controls the ice growth rate and the ice thickness (Jeffries et al., 2006), and the ice thickens downward as a result of heat loss at the top of the ice/snow cover.

The timing of ice formation and decay, ice cover duration, and ice growth play an important role in the surface energy/water budget as well as greenhouse gas budgets at regional scales where lakes occupy a significant fraction of the landscape. In particular, total conductive heat loss resulting from wintertime ice growth has been shown to play a significant role in the energy balance of the lake-rich area of the North Slope of Alaska, and areas occupied by large, deep, lakes (e.g. Great Slave Lake) relative to other lakes in their immediate surrounding (Jeffries et al., 2005, 2006). In addition to their role in regional climate, mid-to high latitude lakes are also sensitive indicators of changing climate conditions. Recent studies using ice phenological observations from a historical Canadian database have shown the sensitivity of lake ice cover during the second half of the 20th century to climate warming as well as to large-scale atmospheric teleconnection patterns (Bonsal et al., 2006). Unfortunately, Canada's historical ground-based observational network which has provided much of the evidence for the documented changes and links to atmospheric forcings, and which included weekly/bi-weekly ice thickness measurements, has almost totally disappeared over the last two decades (Lenormand et al., 2002). Satellite remote sensing, particularly those sensors operating at microwave frequencies, provides a potential means for obtaining frequent ice thickness estimates from space.

A few studies have shown the potential of spaceborne passive microwave radiometry, alone or in combination with radar altimetry, for the retrieval of information regarding lake ice phenology such as ice-on and ice-off dates, and ice cover duration (Kouraev et al., 2007ab; Walker et al., 1993). There has also been some demonstration of the utility of brightness temperature (T_B) from passive microwave airborne radiometers to estimate ice thickness (Hall et al., 1981, 1993; Chang et al., 1997). In particular, a previous study by Hall et al. (1981) showed, though with only four days of airborne/field measurements during an entire winter period, a strong positive relationship between T_B at low frequency (5-6 GHz) and

lake ice thickness. The availability of frequent (twice-daily) T_B measurements from the Advanced Microwave Scanning Radiometer – Earth Observation System (EOS) (AMSR-E) satellite sensor provides an opportunity to more thoroughly examine the strength of this relationship.

In this Chapter 4, we present the first results of its kind on the sensitivity of AMSR-E T_B to estimate the seasonal evolution of ice thickness from two large lakes in northern Canada, Great Bear Lake (GBL) and Great Slave Lake (GSL). The two lakes have the advantage of being big enough to permit the examination of the sensitivity of the low and medium frequency channels (6.9-18.7 GHz) of AMSR-E to ice thickness within homogenous satellite footprints (76, 49, and 28 km, respectively; see **Figure 5.1**) over these two lakes, thus eliminating the possible effect of land contamination.

5.2 Data and method

GBL and GSL are located in the Mackenzie River Basin (MRB; **Figure 5.1**) and rank among the ten largest freshwater lakes in the world. GBL and GSL lie between 60° and 67° N and 109° to 126° W (**Figure 5.1**), with surface areas (average depths) of 31,153 km^2 (76 m) and 28,450 km^2 (88 m), respectively (Rouse et al., 2008a). A summary of January and July temperature and snow precipitation measured at coastal weather stations is provided in **Table 5.1** for the 2002 to 2007 period of analysis described in this chapter. The mean air temperature in the GSL area is generally warmer than that of GBL, and therefore, GSL has an open-water season about four to six weeks longer than GBL (Schertzer et al., 2008). The lake is ice-free from the beginning of June until mid- to late-December, and lake ice conditions on this lake have been reported to exhibit greater inter-annual variability than on GBL (Blanken et al., 2008).

Table 5.1: Mean temperature (°C) in January (July), and total annual snowfall (cm), recorded at Deline (Great Bear Lake), Yellowknife and Hay River (Great Slave Lake) meteorological stations

Year	Great Bear Lake (Deline)		Great Slave Lake (Yellowknife)		Great Slave Lake (Hay River)	
	Mean Temp Jan (July)	Total Snow	Mean Temp Jan (July)	Total Snow	Mean Temp Jan (July)	Total Snow
2002	-24.3 (12.7)	116.4	-25.3 (16.4)	130.2	-21.5 (15.6)	131.6
2003	-26.5 (14.2)	177.7	-26.0 (17.8)	137.0	-21.3 (17.0)	137.2
2004	-28.3 (12.0)	145.3	-29.4 (17.5)	160.2	-25.4 (16.6)	144.7
2005	-24.8 (11.0)	205.4	-26.4 (15.8)	192.1	-22.6 (15.7)	169.4
2006	-27.4 (13.6)	172.8	-22.0 (16.7)	176.6	-19.6 (15.9)	182.9
2007	-22.0 (14.0)	164.9	-21.4 (18.7)	207.3	-17.9 (18.0)	146.2
AVG	-25.5 (12.9)	163.8	-25.1 (17.1)	167.2	-22.1(16.4)	152.0

The evolution of T_B (horizontal and vertical polarizations; 55^o incidence angle) derived from AMSR-E/Aqua level 2A global swath spatially-resampled brightness temperatures product (AE_L2A) was compared to ice thickness obtained with the Canadian Lake Ice Model (CLIMo) (Duguay et al., 2003b) for the period 2002-2007 at both GBL and GSL, since insufficient ground-based measurements are available for a suitable comparison. The one-dimensional thermodynamic lake ice model has been shown to provide good estimates of ice thickness on a daily basis as well as the freeze-up and break-up dates on shallow lakes near Fairbanks (Alaska), and Churchill (Manitoba) (Duguay et al., 2003b), and on large lakes such as GSL (Ménard et al., 2002). T_B data was acquired from the AMSR-E sensor for both descending and ascending overpasses. To examine the sensitivity of T_B at 6.9, 10.7, and 18.7 GHz (horizontal and vertical polarizations) to ice thickness, all AMSR-E observations for each day falling within a 5.1´ × 5.1´ grid overlapping area between descending and ascending modes in AMSR-E were averaged over the areas of interest, within the central sections of GBL (66° N, 120° 30´ W) and GSL (61° 19.8' N, 115° W and 61° 41.8' N, 113° 49.5' W) (**Figure 5.1**).

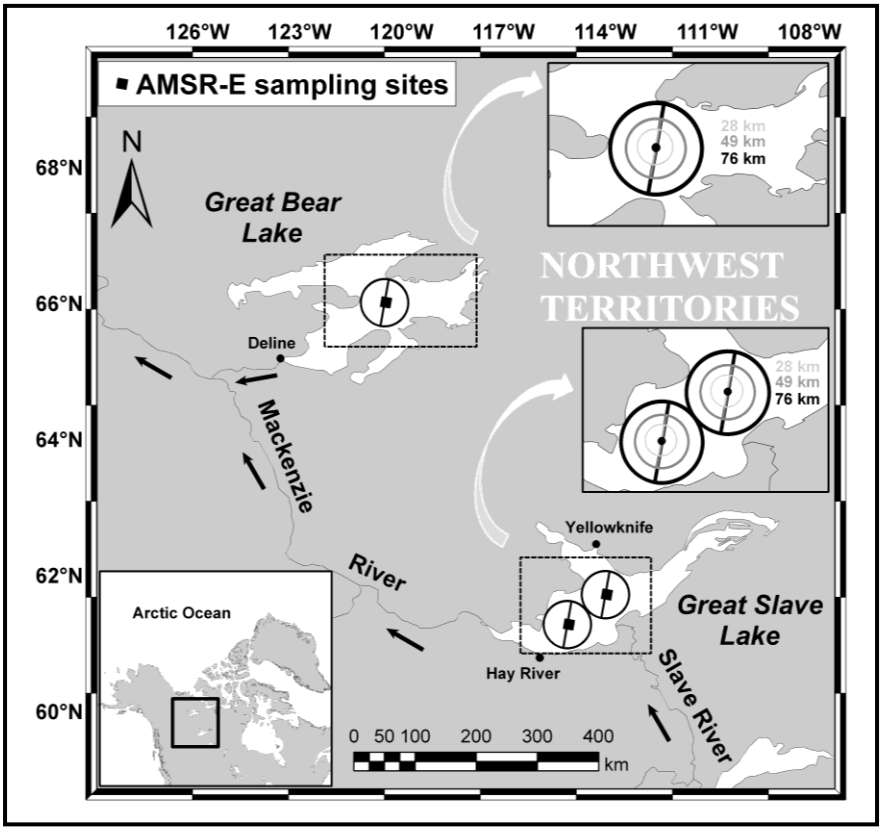

Figure 5.1: Map showing location of Great Bear Lake and Great Slave Lake, and nearby meteorological stations (Deline, Yellowknife, and Hay River) within the Mackenzie River Basin. Solid black squares represent 5.1′ × 5.1′ of sampling area on both GBL and GSL. Black, dark-grey, and bright-grey open circles indicate the diameter of different footprints at 6.9 GHz (black, 76 km), 10.65 GHz (dark grey, 49 km), and 18.7 GHz (bright grey, 28 km), respectively.

During the data collection, any T_B that was recorded when the maximum daily air temperatures were above 0 °C for more than four consecutive days at the nearby meteorological stations, was excluded to eliminate days possibly influenced by surface melt, which affect T_B values. During surface melt events T_B values are not representative of the seasonal evolution of ice thickness.

To examine the relation between T_B and ice thickness, daily ice thicknesses were simulated from CLIMo on both lakes by performing a simulation over the period 2002-2007. The model was forced with mean daily air temperature, wind speed, relative humidity, cloud cover, and snowfall measurements available from the Deline (65° 12' N, 123° 26' W)

meteorological station for GBL, and using station data from Yellowknife (62° 27.6' N, 114° 26.4' W) and Hay River (60° 50.4' N, 115° 46.8' W) for GSL (see **Figure 5.1**). For simulating ice thickness on GBL and GSL with CLIMo, a 40-m mean mixing depth and 25 (%) snow scenario were selected because previous research indicates that GSL has a 40-m mixing layer depth at the onset of ice formation (Schertzer et al., 2008) which is also likely similar over GBL. The scenario of 25 % snow cover over lake ice, which corresponds to 25% of the snow depth measured at the closest meteorological station, was applied to provide a more realistic representation of snow accumulation on the ice surface of the lakes, as snow is strongly redistributed by winds on these lakes during the course of a typical winter season (Duguay et al., 2003b). This scenario has been shown to provide good estimates of ice thickness with CLIMo in a previous investigation on GSL (Ménard et al., 2002).

Simple linear regression was applied to determine the frequencies and polarizations (significance at $p < 0.05$) most sensitive to ice thickness over the five winter seasons (2002-2007). The coefficient of determination (R^2) was also calculated to quantify the variability of T_B explained by seasonal ice thickening.

5.3 Results and Discussion

5.3.1 General Evolution of T_B From Initial Ice Formation to Melt

Lake ice formation, growth, and decay on GBL and GSL encompass fall freeze-up; a long winter period of ice growth and thickening; a short period of ice melting and thinning, and eventually, spring break-up and the complete disappearance of the ice cover. Ice growth (thickening) is influenced mainly by air temperature and the presence of snow on the ice surface. At the frequencies examined in this study, the effect of the atmosphere can largely be ignored such that variations in T_B are determined by emissivity and physical temperature changes of the medium. In addition to the properties of the medium under investigation, emissivity, and thus T_B, also vary with frequency and polarization (the incidence angle being fixed at 55^o for AMSR-E).

As shown in **Figure 5.2**, using the footprint centered on GBL as an example, when air temperature drops below 0 °C and solar radiation decreases, the expected change of T_B in response to lake ice formation is delayed due to the heat capacity in large lakes. Four to six weeks after air temperature started to decrease below 0 °C, the T_B over the lake starts to increase due to the increase in ice fraction. From the first appearance of ice, it takes three to five weeks for complete freeze over (CFO) to occur (i.e. full sheet of ice to form within the footprint of interest). This process is more strongly apparent at H-polarization (top graphic of **Figure 5.2**) where T_B increases by about 70 K from open water to CFO conditions. Ice then starts to thicken (mid-December on GBL; late-December on GSL, not shown) and reaches its maximum thickness (thick grey curve in bottom graphic of **Figure 5.2**) just before the beginning of melt-onset (MO), when the mean air temperature starts to exceed 0 °C. When this temperature is reached, T_B increases rapidly due to the higher air temperature and increasing shortwave flux absorption on the lake ice/snow surface from melt. During this period, melt/refreeze (day/night) events cause fluctuations in T_B along the general springmelt trajectory (from MO onward). A similar process occurs over GSL (not shown).

5.3.2 Relation Between T_B and Lake Ice Thickness

For freshwater ice with few scatterers (e.g. trapped air bubbles created during freezing), the emissivity is predominately affected by the ice/air interface, the ice/water interface, and the ice thickness. Early studies have shown that a uniform bubble-free slab of lake ice emits microwave radiation in a quantity proportional to its thickness (Hall et al., 1981; 1993, Chang et al., 1997). The depth of emission in freshwater ice is well known to decrease with increasing frequency. Also, the temperature dependence of the imaginary part of the dielectric constant causes the depth of emission to decrease with increasing temperature. For example, for ice without impurities, depth of emissions at 6.6/10.7/18/37 GHz have been reported to be in the order of 19/8/2.8/0.7 m at -8.15 ^{o}C and 34/12/4.5/0.9 m at -43.15 ^{o}C (Surdyk et al., 2002). Given this, the low to mid-frequency channels available on the AMSR-E platform (6.9, 10.7, 18.7 GHz) possess depth of emissions sufficient to interact with ice and water mediums, and to show the influence of increasing ice thickness on T_B.

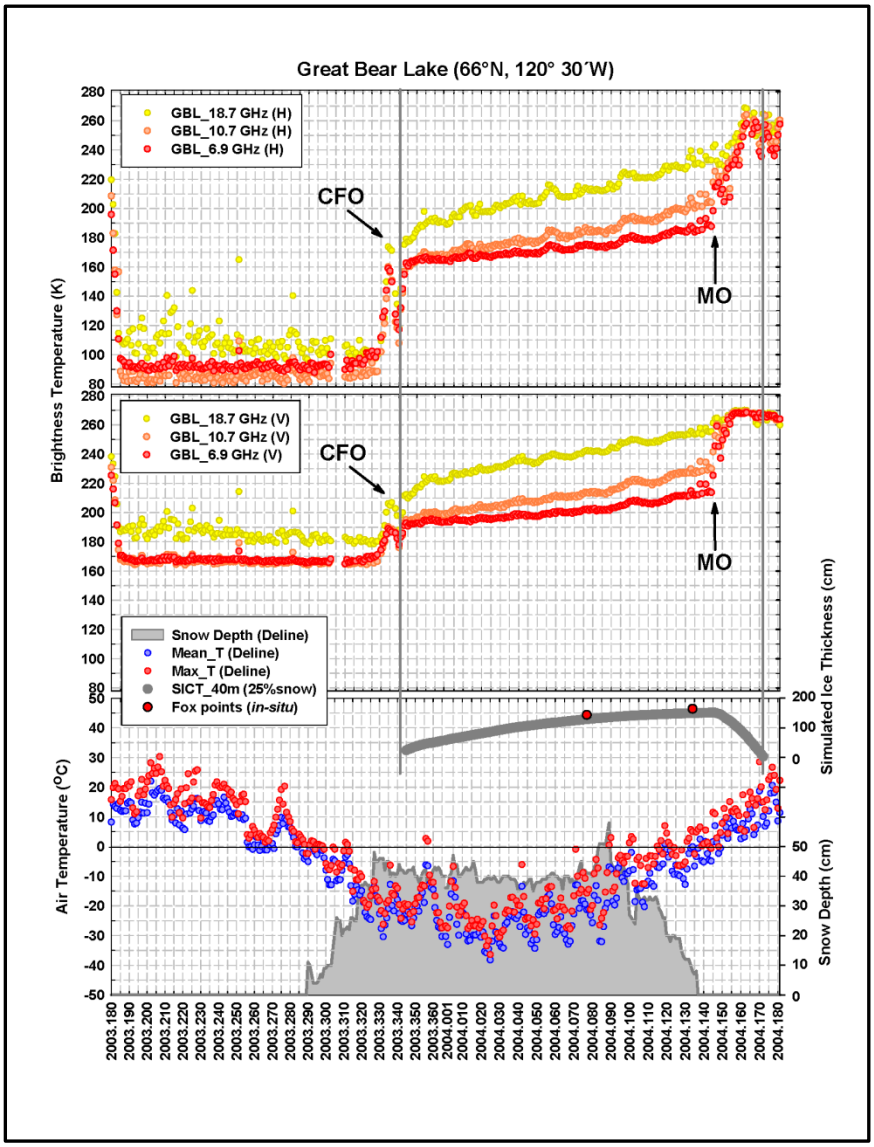

Figure 5.2: The time series of horizontal (top) and vertical (middle) polarizations brightness temperatures at 6.9, 10.7, and 18.7 GHz on GBL from the 2003-2004 winter period. The time series of maximum (Max_T, red) and mean (Mean_T, blue) air temperatures obtained at Deline is shown at the bottom of the figure, with snow depth (grey). Simulated ice thicknesses in the winter of 2003-2004 obtained with CLIMo (details given in the text) are represented by the thick grey curve. The two red circles overlaid on the ice thickness curve correspond to in-situ measurements made during field visits on GBL (65°15' N, 122°51.5 'W).

Over the winter ice growth period, between CFO and MO in as shown in **Figure 5.2**, T_B increases as expected since thicker ice reduces the influence of the lower emissivity (radiometrically cold) liquid water below the ice and emits its own microwave energy.

(Lemmetyinen et al., 2009). In previous study (Hewison et al., 1999), the near-nadir mid-winter emissivity of lake ice was estimated to be around 0.9 at 18.0 GHz near Pudäsjarvi, Finland, which is much higher than that of open water (0.4-0.5). As shown in **Figure 5.2**, between CFO and MO, T_B is about 20-30 K higher at vertical polarization compared to horizontal polarization at all frequencies. T_B values are smaller by about 20-30 K at the lower frequencies (6.9-10.7 GHz) in contrast to the higher 18.7 GHz frequency over the full extent of the ice growth season. Since 18.7 GHz has a shorter depth of emission than 10.7 GHz and 6.9 GHz, it is affected by the underlying radiometrically cold water only in the early period of winter.

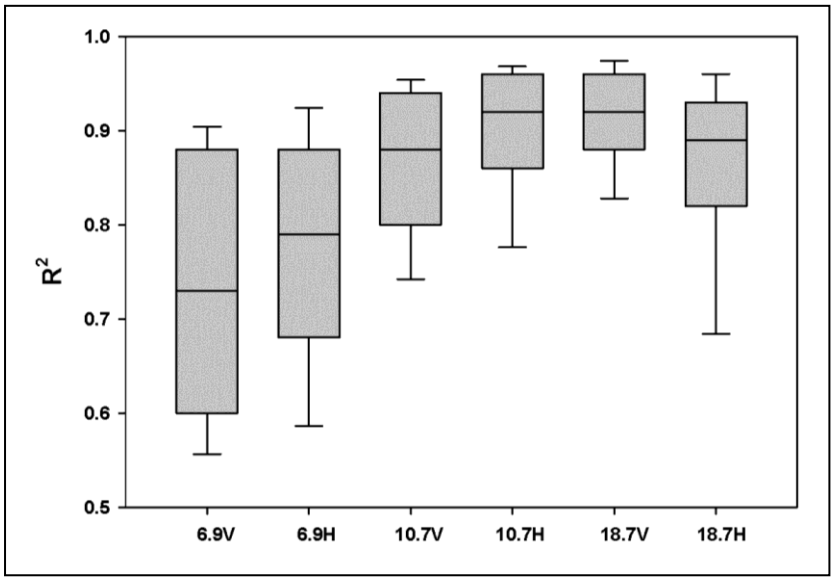

Figure 5.3: Boxplots of R^2 values between simulated ice thickness (with 40 m mixing depth and 25 percent snow cover scenario) and brightness temperature at 6.9, 10.7, and 18.7 GHz from the sampled AMSR-E footprints showed in Figure 5.1 (averaged over five winter seasons, 2002-2007), showing the median (center line), the first and third quartiles ranges (the box), and the maximum and minimum limits (whiskers).

The temperature-vulnerable absorption length of ice causes a wavy pattern in the time series of T_B for both lakes, as depicted in **Figure 5.2 and Figure 5.3**. These oscillating characteristics of T_B depend greatly on the imaginary part of the index of refraction of ice.

This is more noticeable during the warmer winter season (2005-2006), which experienced greater air temperature variability during the course of the ice growth season.

5.3.2.1 Strength of Relation over Full Study Period (2002-2007)

The statistics summarized in **Table 5.2** (average 2002-2007) and the box plots presented in **Figure 5.3** clearly reveal the strong relation between ice simulated thickness and T_B for all three frequencies examined herein. When all three sites and years are grouped together, the strongest relation is found at the 10.7 and 18.7 GHz frequencies with over 90% of the variations in T_B explained by variations in ice thickness. The R2 values are slightly higher at the vertical polarization for 18.7 GHz and at horizontal polarization for the 10.7 GHz frequency. Contrary to the results obtained by Hall et al. (1981) with airborne measurements, the relation between T_B and ice thickness is weaker, though still significant ($p < 0.05$), at the lower frequency (6.9 GHz).

Two factors may explain this discrepancy. First, the footprint at 6.9 GHz (75 km × 43 km) is larger than that of 10.7 GHz and even more than at 18.7 GHz (27 km × 16 km), hence encompassing a larger area on GBL and GSL. The lake ice model provides a single value of ice thickness over the large footprint on any day, while T_B values from AMSR-E are influenced by the spatial variability in ice thickness which is known to vary across lakes. Therefore, the larger footprint at 6.9 GHz may include a greater range of ice thicknesses than given by the ice model. A second factor that may also explain the lower R^2 values at 6.9 GHz is that the footprints of the three sites may somewhat be influenced by land contamination, although every effort was made to exclude such an effect. Nonetheless, the strong relations found at 10.7 and 18.7 GHz are very promising for future investigations on the estimation of lake ice thickness from AMSR-E.

5.3.2.2 Cold Winter (2003-2004) Versus Warm Winter (2005-2006)

Although a strong relation was found to exist between T_B and ice thickness when data from all sites and years are grouped together, it is also worth examining how this relation differs,

if at all, when comparing a cold winter with a warm winter. **Table 5.2** and **Figure 5.4** reveal that inter-annual variability of climate affects ice growth and thus both the strength of the relation between T_B and ice thickness, and to a lesser extent the slope of the relation between the two variables. Three specific observations can be drawn from **Table 5.2** regarding the R^2 values. First, the strength of the relation is weaker (i.e. smaller R^2 values) for the warmer winter compared to the colder winter. This is particularly evident with January 2004 and January 2006 temperatures at GSL sites (**Table 5.1**) where T_B values exhibit greater inter-seasonal variability in winter 2005-2006 compared to 2003-2004 (**Figure 5.4**) due to larger fluctuations in air temperature during ice growth.

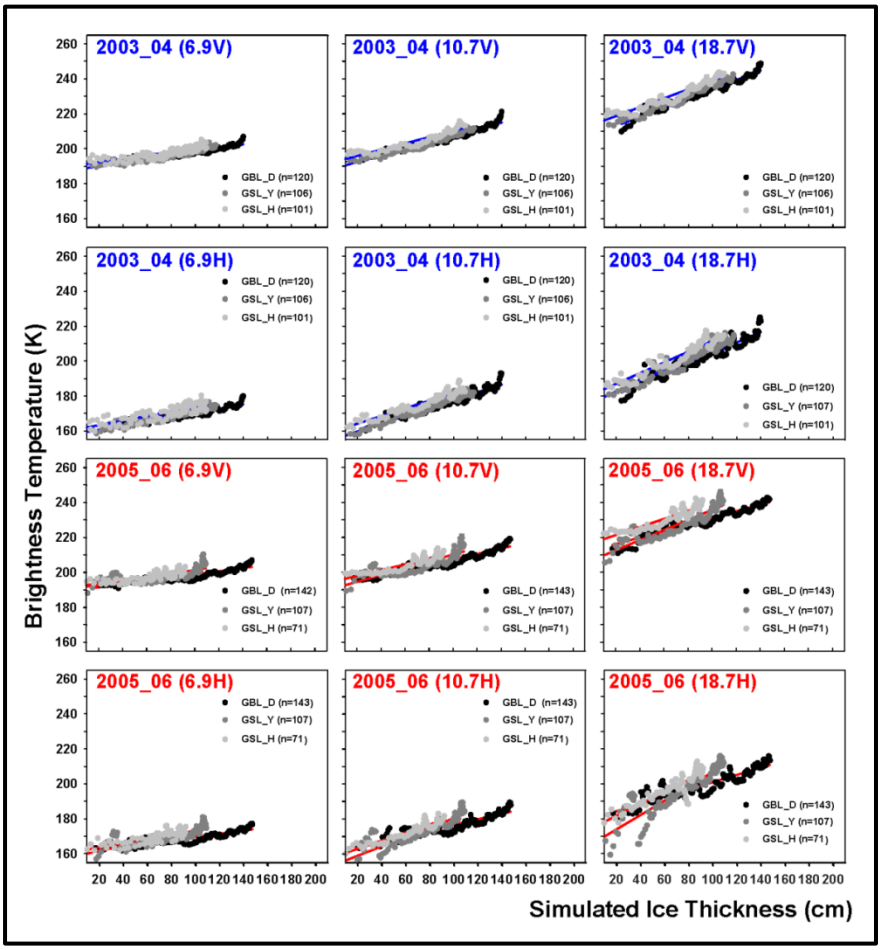

Figure 5.4: Linear regression plots between simulated lake ice thickness and brightness temperature at 6.9, 10.7, and 18.7 GHz for GBL_D (Deline), GSL_Y (Yellowknife) and GSL_H (Hay River) for a cold winter (2003-2004) and a warm winter (2005-2006). Values (n) in brackets indicate the number of paired ice-thickness and T_B observations.

Second, the strength of the relation is always stronger at V-polarization for the 18 GHz channel, regardless of site, while at 10.7 and 6.9 GHz the strongest R^2 values are obtained at either V- or H-polarization depending on site and season (cold versus warm winter). This effect is the subject of ongoing investigation. Third, the regression slopes shown in **Table 5.2** provide useful information regarding the rate of change of T_B with ice thickness (K cm^{-1}). Steeper slopes are found at H-polarization for all three frequencies. Also, as frequency increases from 6.9 to 18.7 GHz, the slopes become steeper. For example, the slope at GBL_D (2003-2004) is 0.26 K cm^{-1} at 18.7(V) GHz and 0.10 K cm^{-1} at 6.9(V) GHz. Given the strong proportion of the variations in T_B explained by ice thickness growth, this relation could potentially be inverted to determine winter ice growth rates (cm K^{-1}) and thus estimate ice thickness on these large lakes.

Table 5.2: Coefficient of determination (R^2) and regression slope of relation between T_B and ice thickness for a cold winter (2003-2004), a warm winter (2005-2006), and average conditions (2002-2007) for sampling FOOTPRINTS AT GBL_D (Deline), GSL_Y (Yellowknife) and GSL_H (Hay River). Regression slopes (K cm^{-1}) are in brackets

Year		6.9 H	6.9V	10.7H	10.7V	18.7H	18.7V
2003_04	GBL_D	0.86 (0.12)	0.89 (0.10)	0.92 (0.21)	0.95 (0.19)	0.91 (0.30)	0.96 (0.26)
	GSL_Y	0.88 (0.14)	0.88 (0.11)	0.96 (0.23)	0.96 (0.19)	0.93 (0.31)	0.97 (0.27)
	GSL_H	0.68 (0.13)	0.71 (0.10)	0.92 (0.22)	0.89 (0.18)	0.91 (0.31)	0.93 (0.25)
2005_06	GBL_D	0.78 (0.09)	0.80 (0.09)	0.84 (0.16)	0.89 (0.16)	0.85 (0.21)	0.90 (0.19)
	GSL_Y	0.65 (0.15)	0.52 (0.10)	0.78 (0.27)	0.70 (0.19)	0.82 (0.41)	0.84 (0.29)
	GSL_H	0.61 (0.12)	0.58 (0.09)	0.89 (0.23)	0.77 (0.16)	0.81 (0.35)	0.81 (0.23)
Average (2002-2007)		0.78 (0.13)	0.74 (0.10)	0.90 (0.22)	0.87 (0.17)	0.86 (0.29)	0.91 (0.23)

5.4 Conclusions

This study has revealed the strong sensitivity of T_B from the low and middle frequency channels (6.9 - 18.7 GHz) of AMSR-E to the seasonal evolution of ice thickness on two large northern lakes. Using data from five winter seasons (2002 - 2007), it was found that

T_B at the 10.7 and 18.7 GHz frequencies were highly correlated with ice thickness; R^2 values were in the order of 0.9 when data from both lakes and for all years were pooled together. Some differences in the strength of the relation were observed when comparing T_B and ice thickness estimates from a cold versus a warm winter. The strength of the relation between T_B at the 10.7 and 18.7 GHz frequencies and ice thickness was higher for the colder winter, when less inter-seasonal variability in air temperature was observed at meteorological stations located in the vicinity of the lake sites.

The results presented in this paper are consistent with results from earlier work based on airborne passive microwave measurements coincident with limited ice thickness observations (4-6 measurement campaigns during a full winter from Walden Reservoir, north-central Colorado), which also found a strong relation between T_B and ice thickness at frequencies between about 5 to 22 GHz (Hall et al., 1981; 1993, Chang et al., 1997). However, these previous studies showed the higher sensitivity of T_B at 5 GHz (R^2=0.98) to ice thickness, compared to the 18.7 GHz (R^2=0.67). In contrast, using daily AMSR-E T_B measurements at similar frequencies, the present study shows a stronger relation with ice thickness at 18 GHz frequency (R^2= 0.86-0.91) and 10 GHz (R^2= 0.87-0.90) than at 6 GHz (R^2= 0.74-0.78). These results indicate that T_B measurements obtained from AMSR-E offer a high potential for estimating ice thickness on large northern lakes on a regular basis.

Chapter 6: Estimation of ice thickness on large northern lakes from AMSR-E brightness temperature measurements

In this chapter, an ice thickness retrieval algorithm utilizing data from the Advanced Microwave Scanning Radiometer – Earth Observing System (AMSR-E) was developed and applied to Great Bear Lake (GBL) and Great Slave Lake (GSL) for the period 2002-2009. The temporal evolution of vertically polarized AMSR-E brightness temperature (T_B) at 18.7 GHz was explored to estimate ice thickness between the late freeze-up (ice-on) and early break-up (melt-onset) periods. The sensitivity of AMSR-E T_B at H and V polarizations to the seasonal evolution of ice thickness was examined statistically and with forward simulations of T_B using the most recent version of the Helsinki University of Technology (HUT) model which incorporates a freshwater ice layer. The stronger relation found between T_B at 18.7 GHz V-pol and ice growth was exploited for the development of a regression-based ice thickness retrieval algorithm. Simple linear regression equations, one that combines both GBL and GSL (global equation) and two other specific to each lake (regional equations), allow for the estimation of ice thickness on a monthly basis from January to April. Estimated late-winter ice thicknesses on GBL were determined to be on average 5-15 cm thicker than on GSL with the exception of ice season 2005-2006 when it was estimated to be 10 cm thicker on GSL. For both lakes the 2004-2005 and 2008-2009 ice seasons experienced the thickest end-of-winter ice thicknesses, ranging from 146 to 150 cm on GBL and GSL. The thinnest end-of-winter ice thicknesses were on average 134 cm on GBL (2005-2006) and 140 cm on GSL (2007-2008). Variability in air temperature, snowfall and subsequent redistribution by wind, and lake depth explain ice thickness variations within and between lakes over the seven winter seasons analyzed. Estimated ice thicknesses from AMSR-E compare well with coincident *in situ* measurements collected on GBL and GSL over a limited number of ice seasons and sites within the large passive microwave footprints (MBE = 8 cm and RMSE = 19 cm).

Key words: Ice thickness, AMSR-E, brightness temperature, Great Bear Lake, Great Slave Lake, Arctic, Canada

6.1 Introduction

Lake ice cover is a sensitive indicator of climate variability and change (Brown et al., 2010; Duguay et al., 2006). It is also important for studying the role of lakes in high-latitude weather and climate as the presence/absence of seasonal floating ice has an effect on heat and energy transfers across the lake-atmosphere interface (Brown et al., 2010; Kheyrollah Pour et al., 2012). Ice growth/thickening occurs between the onset of ice formation and melt-onset in response to energy loss through conductive heat flow to the atmosphere above from the freshwater under the lake ice to the ice/snow boundary (Jeffries and Morris, 2006). Monitoring and modeling of ice thickness therefore provides insight into the thermodynamics of lake ice at northern latitudes in response to climate. Measurements of ice thickness are also important to northern communities that depend on winter ice roads for the transportation of goods, access to resources, and for recreational purposes. A reduction in both the duration of ice cover and its thickness with climate warming will create problems of accessibility to food by reducing the reliability of traditional hunting ice-based routes and safety of ice-based travel.

The variability and change of ice thickness has been studied using historical ground-based observations and numerical one-dimensional (1-D) thermodynamic models (Ashton, 2011; Brown et al., 2011; Duguay et al., 2003; Gough et al., 2004; Ménard et al., 2002; Morris et al., 2005; Vuglinsky et al., 2002; Zaier et al., 2010). However, ground-based measurements present limited area (point) coverage and lake ice models usually provide 1-D estimates of ice thickness for a single lake depth at a time. Both methods do not represent the spatial distribution of ice thickness over an entire lake surface. In addition, ground-based observational networks that have provided historical evidence for changes in ice phenology (freeze-up and break-up dates, and ice duration) and thickness during the second half of the 20th century have been diminished to the point where they can no longer provide the quality

of observations necessary for climate monitoring (Duguay et al., in press). Satellite remote sensing is the most logical alternative for lake ice observing (Duguay et al., 2011; Kang et al., 2012).

Previous active microwave remote sensing studies using altimetry and scatterometry have focused on monitoring the temporal evolution of seasonal ice cover from initial ice formation through the decay period on large lakes (Howell et al., 2009; Kouraev et al., 2007). Other studies have suggested that C-band synthetic aperture radar (SAR) could be used to determine ice thickness in northern shallow lakes when combined with optical data that can provide estimates of lake depth (Duguay et al., 2002; Duguay and Lafleur, 2003). Furthermore, the potential to estimate lake ice thickness from passive microwave brightness temperature (T_B) measurements obtained at low frequencies (1-10 GHz) has been demonstrated with a limited number of airborne radiometric measurements coincident with ground-based ice thickness observations (Swift et al., 1980; Hall et al., 1981, 1993; Chang et al., 1997). More recently, Kang et al. (2010) have shown in a preliminary manner that the temporal evolution of T_B measurements from the Advanced Microwave Scanning Radiometer–Earth Observing System (AMSR-E) 10.7 GHz and 18.7 GHz frequency channels during the ice growth season on Great Bear Lake (GBL) and Great Slave Lake (GSL), Canada, is strongly correlated with ice thickness as estimated with a numerical lake ice model (Duguay et al., 2003). There is a need to examine more closely the strength of the relation between ice thickness and passive microwave T_B measurements, and how it can be further exploited to estimate ice thickness and map its spatiotemporal evolution on large northern lakes such as GBL and GSL.

The primary objective of this research was to develop an ice thickness retrieval algorithm from AMSR-E T_B measurements and subsequently map the spatiotemporal variability of ice thickness on GBL and GSL. In this paper, we first examine the sensitivity of T_B to the seasonal evolution of ice thickness through a statistical comparison with estimates obtained from the Canadian Lake Ice Model (CLIMo; Duguay et al., 2003), and with forward

simulations of T_B using the most recent version of the Helsinki University of Technology (HUT) emission model, which incorporates a freshwater ice layer. Three linear regression equations using AMSR-E T_B data, one for each GBL and GSL and one that combines both lakes, are then developed and validated against independent ice thickness estimates from CLIMo and a limited number of ground-based measurements. The three regression equations are then applied to produce monthly ice thickness maps of GBL and GSL, and to analyze intra- and inter-lake variability in thickness for the period 2002-2009. The paper concludes with a summary of key findings and suggestions where future enhancements are needed.

6.2 Study Area

GBL and GSL are the largest freshwater lakes of northern Canada (**Figure 6.1**), lying between 60° to 67° N and between 109° to 126° W. Surface areas range from 31,000 km^2 and 28,000 km^2 and average depths from 76 m and 88 m for GBL and GSL, respectively (**Figure 6.2**) (Kang et al., 2010, 2012). The different hydrological systems and energy balance of GBL and GSL result in distinctive thermodynamics, hydrodynamic, and surface climatic cycles (Rouse et al., 2008a). These lakes are known to have large seasonal lags in temperature and fluxes compared to other contiguous land cover in their adjacent regions (León et al., 2007). No complete disappearance of ice occurs until the middle (end) of July on GBL. Situated at a more southern location, GSL is generally influenced by warmer mean air temperature and a longer open-water period by about three to four weeks compared to GBL (Kang et al., 2012). GSL is ice-free from the beginning of June until mid- to late-December, and lake ice conditions on this lake have been reported to exhibit larger inter-annual variability than those on GBL (Blanken et al., 2008; Kang et al., 2010). In contrast to GBL, the discharge from the Slave River contributes to earlier ice break-up on GSL.

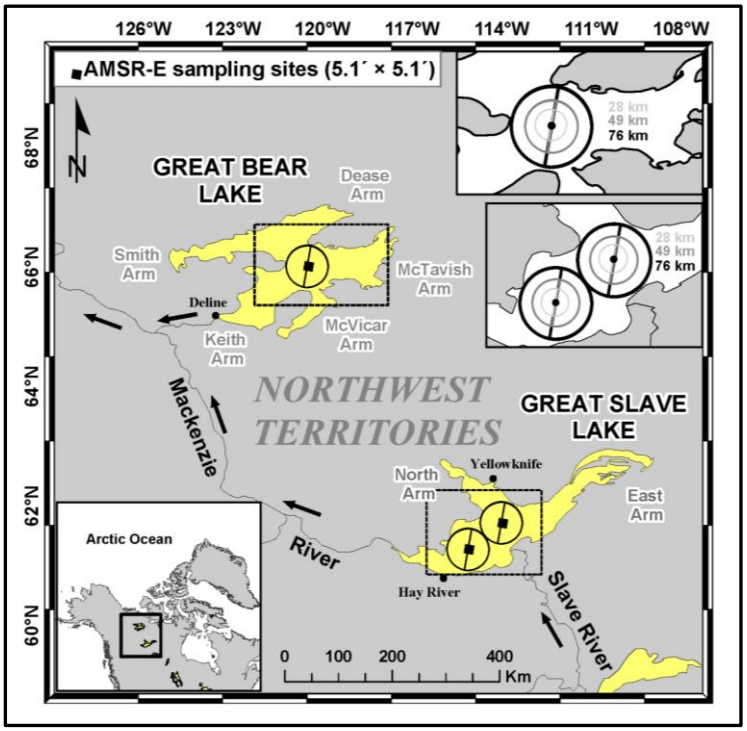

Figure 6.1: Map showing location of Great Bear Lake and Great Slave Lake, and nearby meteorological stations (Deline, Yellowknife, and Hay River) within the Mackenzie River Basin. Solid black squares represent 5.1´ × 5.1´ of sampling area on both GBL and GSL. Black, dark-grey, and bright-grey open circles indicate the diameter of different footprints at 6.9 GHz (black, 76 km), 10.65 GHz (dark grey, 49 km), and 18.7 GHz (bright grey, 28 km), respectively.

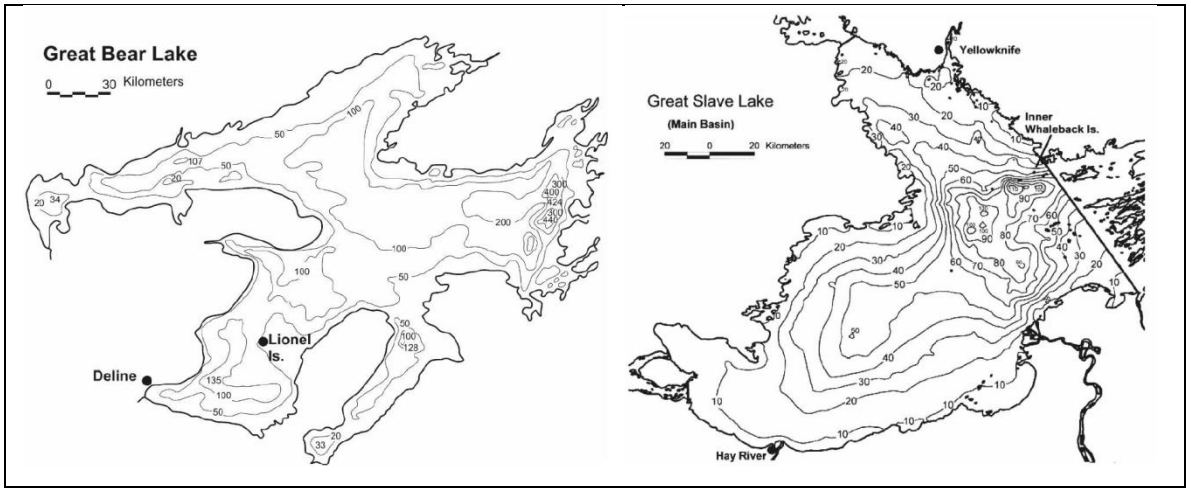

Figure 6.2: Bathymetry of Great Bear Lake (left) and Great Slave Lake (right) with the location of Deline, Yellowknife, and Hay River. Lake depth contours are in meter (Rouse et al., 2008a).

For the period of analysis (2002-2009), the average annual air temperature recorded at the Deline weather station, near the western shore of GBL, was -6.3 °C with 18.1 cm of average annual snowfall while the average annual air temperature and snowfall, which are recorded at the lakeshore of GSL (at Yellowknife and Hay River), were -3.4 °C and 17.7 cm, respectively (**Table 6.1**). In situ ice thickness measurements are very limited on GBL and GSL, particularly over the period of this study. For GBL values of 137 cm and 89 cm have been reported in March 2004 and 2005, respectively (Woo et al., 2007). A few additional ice thickness observations with precise geographical locations have been recorded on both GBL and GSL. These are described in a later section and were used as one source for the validation of the ice thickness retrieval algorithm from passive microwave satellite data.

Table 6.1: Seasonal mean air temperature (°C) for winter (December, January, and February; DJF), spring (March, April, and May; MAM), summer (June, July, and August; JJA), autumn (September, October, and November; SON), and annual snowfall (cm) recorded at Deline (Great Bear Lake), Yellowknife and Hay River (Great Slave Lake) meteorological stations (2002-2009). M is missing snowfall data.

	DJF		MAM		JJA		SON		Annual temp		Annual snowfall (cm)	
	GBL	GSL	GBL	GSL	GBL	GSL	GBL	GSL	GBL	GSL	GBL	GSL
2002	-23.9	-21.5	-10.6	-9.5	11.1	14.2	-3.1	-1.3	-6.0	-4.0	14.55	15.46
2003	-22.1	-20.6	-8.2	-4.3	11.6	14.7	-3.8	-0.3	-6.1	-2.9	22.21	16.18
2004	-24.4	-21.0	-11.7	-7.6	10.4	13.8	-6.9	-2.9	-8.7	-5.1	16.14	16.94
2005	-24.7	-22.9	-6.0	-3.6	10.0	13.6	-5.4	0.0	-5.6	-2.1	25.68	24.11
2006	-20.6	-15.9	-7.8	-1.0	12.1	15.9	-4.9	-2.0	-5.5	-0.9	28.80	23.97
2007	-22.7	-18.7	-9.7	-4.7	11.2	14.6	-5.3	-1.6	-7.0	-3.3	16.99	19.74
2008	-25.0	-23.5	-8.2	-6.0	10.6	15.4	-4.7	0.0	-7.2	-3.9	16.73	26.89
2009	-25.4	-23.8	-10.4	-7.1	10.7	14.2	-4.5	0.1	-7.1	-3.7	M	22.23
Avg	-23.5	-21.8	-8.6	-4.9	11.4	14.5	-4.6	-1.6	-6.3	-3.4	18.1	17.7
STD	1.5	2.9	2.0	2.2	0.8	0.9	1.5	1.7	1.1	1.3	5.4	3.7

6.3 Data and methods

Data from three sources and two models were used in this research. The data comprised AMSR-E T_B measurements, meteorological station data, and *in situ* ice thickness measurements. Models consisted of the 1-D thermodynamic lake ice model, CLIMo

(Duguay et al., 2003), and the most recent version of the HUT emission model (Lemmetyinen et al., 2010). The data and models, and their intended use, as well as the approach to estimate ice thickness from AMSR-E and its evaluation are described next.

6.3.1 Data

6.3.1.1 AMSR-E data

AMSR-E T_B data were obtained for the period of 2002-2009. AMSR-E (fixed incident angle: 54.8 degree) is a conically-scanning, twelve-channel passive microwave radiometer system, measuring horizontally and vertically polarized microwave radiation from 6.9 GHz to 89.0 GHz (Kang et al., 2011). The instantaneous field-of-view (IFOV) for each channel varies from 76 by 44 km at 6.9 GHz to 6 by 4 km at 89.0 GHz, and the sampling interval of each channel is 10 km (5 km sampling interval in 89.0 GHz). In this study, the AMSR-E/Aqua L2A global swath spatially raw brightness temperature product (AE_L2A) was used. AMSR-E T_B measurements for each day falling within a 5.1′ × 5.1′ (9.48 km × 9.48 km) grid using both descending and ascending overpasses were averaged over the areas of interest, within the central sections of GBL (66° N, 120° 30′ W) and GSL (61° 19.8′ N, 115° W and 61° 41.8′ N, 113° 49.5′ W) (**Figure 6.1**). The divide-and-conquer method of the Delaunay triangulation and the inverse distance weighted (IDW) linear interpolation were applied to the L2A T_B data because the T_B measurements in ascending and descending modes did not match the exact same position over GBL and GSL due to different orbit overpasses of AMSR-E. Since the sampling intervals at the frequencies of interest to estimate ice thickness (6.9 to 18.7 GHz; Kang et al., 2010) are spaced every 10 km along and across a track in AMSR-E L2A products, we chose 10 km grid spacing for the linear interpolation.

6.3.1.2 Meteorological station data

Meteorological data from the National Climate Data and Information Archive of Environment Canada (http://climate.weatheroffice.ec.gc.ca/climateData/canada_e.html) were acquired from three stations located in the vicinity of GBL and GSL. The stations selected include Deline (YWJ, 65° 12' N, 123° 26' W) to provide climate information on GBL, and Yellowknife (YZF, 62° 27.6' N, 114° 26.4' W) and Hay River (YHY, 60° 50.4' N, 115° 46.8' W) to characterize the climate in the GSL area. Time series of maximum and mean daily air temperatures for seven winter seasons (from 2002-2009) were used for determining ice-on and melt-onset dates with AMSR-E T_B at 18.7 GHz measurements, as described in Kang et al. (2012). Daily mean values of air temperature, relative humidity, wind speed, cloud cover and snow depth from the meteorological stations were also utilized as forcing data for CLIMo ice thickness simulations (described in 3.2.1). In addition, some of this data was used in the HUT model forward simulations (described in 3.2.2).

6.3.1.3 Ice thickness measurements

The Canadian Ice Service (CIS) provides near weekly *in situ* ice thickness measurements (1952-2010) for Back Bay, GSL, near Yellowknife (Environment Canada, 2010; Lenormand et al., 2002), with the exception of a few years without reported observations (May 1996 to November 2002). According to Ménard et al. (2002), the average maximum ice thickness in Back Bay was 1.33 ± 0.19 m (1960-1991). CIS ice thickness measurements for the period 2002-2009 were compared with AMSR-E ice thickness estimates retrieved from the regressions equation developed in section 3.3. A more limited number of ice thickness measurements (11 in total) made on GBL during winters 2003-2004 and 2006-2007 were also available for the evaluation of ice thickness equations.

6.3.2 Model simulations

6.3.2.1 Thermodynamic lake ice model simulations

Lake ice thickness simulations were performed with CLIMo (Duguay et al., 2003) for two purposes: 1) to assess the sensitivity of AMSR-E T_B data to the seasonal evolution of ice thickness through forward simulations with the HUT model using CLIMo output as forcing data and 2) to develop and evaluate the ice thickness retrieval algorithm (regression equations) from AMSR-E T_B observations. Ground-based measurements of lake ice thickness are sparse. Therefore, we used independent estimations of ice thickness from CLIMo (details given in 3.3) to evaluate the AMSR-E lake ice thickness regression equations. Ice models like CLIMo present a viable alternative in providing independent estimations of ice when well validated over specific sites. Such is the case for the Back Bay and Hay River sites on GSL, and to a more limited extent near Deline on GBL (e.g. Ménard et al., 2002; Kheyrollah Pour et al., 2012). Similar independent model estimations of ice thickness have recently been used for the evaluation of a thin sea ice thickness retrieval algorithm from SMOS brightness temperatures (Kaleschke et al., 2012).

Daily ice thicknesses were simulated with CLIMo on both GBL and GSL using mean daily air temperature, wind speed, relative humidity, cloud cover, and snow depth measurements from the Deline, Yellowknife, and Hay River meteorological stations as forcing data over the period 2002-2009. CLIMo is based on the 1-D unsteady heat conduction equation with penetrating solar radiation (Duguay et al., 2003; Brown et al., 2011). The surface energy budget can then be derived by the following:

$$F_0 = F_{lW} - \varepsilon\sigma T_s^4\,(0,t) + (1-\alpha)(1-I_0)F_{SW} + F_{lat} + F_{sens} \qquad \textbf{(6.1)}$$

where F_0 (Wm^{-2}) is the net downward heat flux absorbed at the surface, ε is the surface emissivity, σ is the Stefan-Boltzmann constant (5.67×10^{-8} Wm^{-2} K^{-4}), T_s is surface temperature, F_{lw} (Wm^{-2}) is the downwelling longwave radiative energy flux, F_{lat} (Wm^{-2}) and F_{sens} (Wm^{-2}) are the downward latent heat flux and sensible heat flux, respectively

(Brown et al., 2011; Ménard et al., 2002). Growth at the ice underside is determined by the difference between the conductive heat flux into the ice and the heat flux out of the upper surface of the mixed layer (Brown et al., 2011). In order to provide a more realistic representation of the depth of the mixed layer just before the beginning of ice formation and of snow accumulation on the surface of ice cover due to the redistribution of snow by winds, a mean mixed layer depth of 40 m and 25 % snow scenario were selected for simulations over the AMSR-E footprints shown in **Figure 6.1** (Kang et al., 2010). CLIMo has previously been shown to provide good estimates of ice thickness on a daily basis, as well as the timing of freeze-up and break-up dates on lakes of various depths (Brown and Duguay, 2011a,b; Duguay et al., 2003; Ménard et al., 2002).

6.3.2.2 Helsinki University of Technology (HUT) model forward simulations

Kang et al. (2010) recently showed a strong statistical relation between ice thickness simulated with CLIMo and AMSR-E T_B on a daily basis, particularly at 18.7 GHz V-pol. In **Figure 6.3**, the site on GBL (2003-2004) is used to illustrate the general sensitivity of T_B during the period of ice growth/thickening. This figure shows the evolution of T_B at 6.9, 10.7, and 18.7 GHz and two polarizations (H-pol and V-pol) for the same time period (top and middle panels) and the time series of maximum/mean air temperatures and snow depth from the Deline meteorological station, and simulated ice thickness from CLIMo (bottom panel). From the ice-on date near mid-December to the onset of melt (MO) in May, the increase in T_B is due to ice growth until it reaches its maximum thickness around mid-April. An increase in T_B is expected during the ice growth season since thicker ice reduces the influence of the lower emissivity of liquid water (radiometrically cold) below the ice cover (Kang et al., 2010). The oscillating behavior of T_B at H-pol and V-pol during the ice growth period depends greatly on the (temperature-dependent) imaginary part of the index of refraction of ice (Chang et al., 1997; Kang et al., 2010).

Emission models such as HUT allow for forward simulations of T_B at frequencies and polarizations (H and V) that can be compared to that of passive microwave sensors. The newest version of the HUT model (Lemmetyinen et al., 2010; 2011) was used to further

demonstrate the sensitivity of AMSR-E T_B at 18.7 GHz to ice growth/thickening and to seasonal air temperature variability on GBL and GSL.

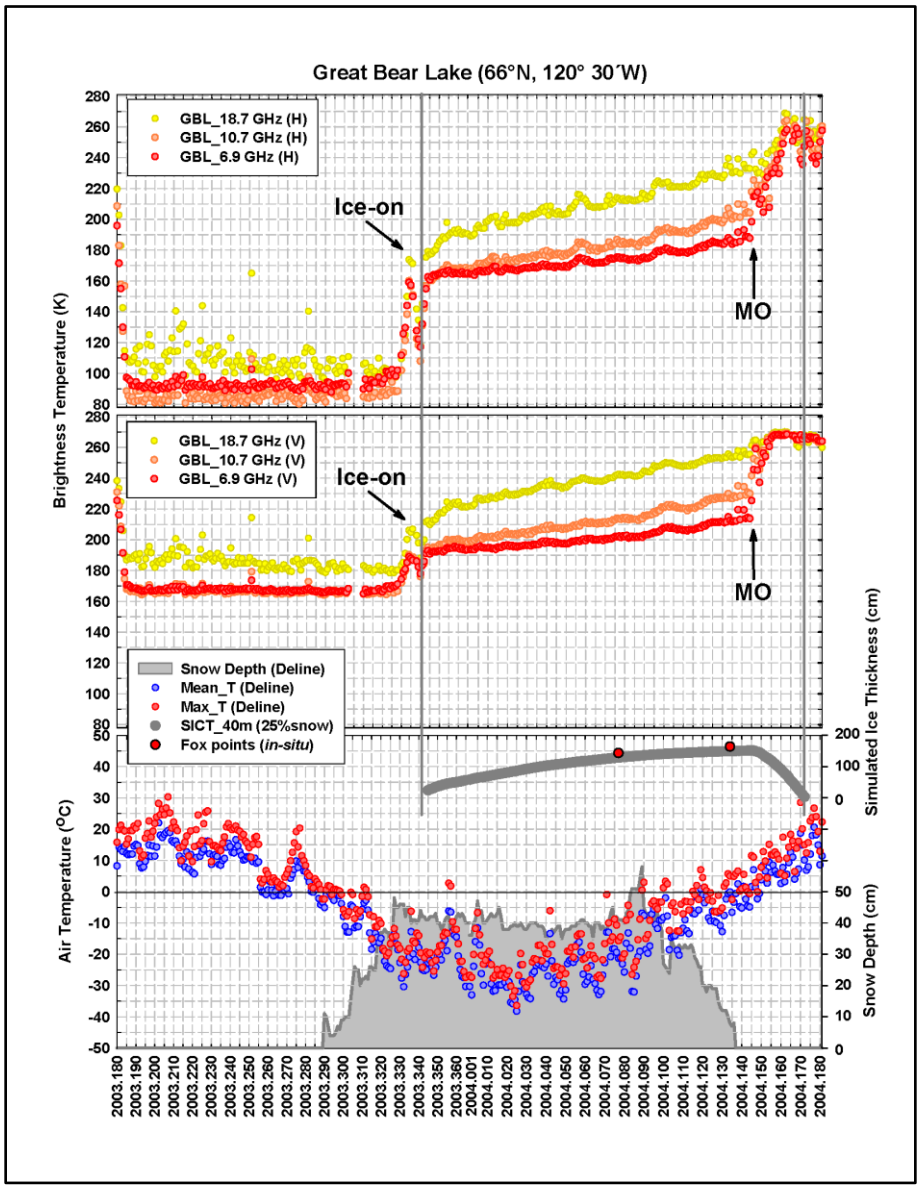

Figure 6.3: Time series of H-pol (top panel) and V-pol (middle panel) brightness temperatures at 6.9, 10.7, and 18.7 GHz for GBL site during ice season 2003-2004. The time series of maximum (Max_T, red) and mean (Mean_T, blue) air temperatures obtained at the Deline meteorological station is shown in the bottom panel along with snow depth (grey). Simulated ice thicknesses obtained with CLIMo are represented by the thick grey curve. The two red circles overlaid on the ice thickness curve correspond to *in situ* measurements made during field visits on GBL (65°15' N, 122°51.5 'W).

The multiple layer adaptation of the modified HUT emission model takes into consideration the influence of multiple reflections between layer boundaries at which transmission, reflection and refraction are calculated by the Fresnel equations (Lemmetyinen et al., 2010). The HUT model expansion for multiple layers also presents the inclusion of ice layers within the simulated snowpack, describing the ice as a simple non-scattering layer of absorptive media (Lemmetyinen et al., 2011). Emission from the medium under the stacked snow and ice layers is determined from the calculated dielectric constant of the medium and the roughness of ice/water interface (Gunn et al., 2010). For snow layers, the HUT model applies the delta-Eddington approximation to the radiative transfer equation (absorption, scattering and extinction coefficients), which applies an empirical constant to determine the forward scattered intensity through the medium (Lemmetyinen et al., 2009; 2010). The emission of a medium with thickness d_0 can be obtained from:

$$T_{SNOW} = T_0 \frac{\kappa_a}{\kappa_e - q\kappa_s}\left(1 - \frac{1}{L}\right) \quad \textbf{(6.2)}$$

$$= T_{phys} \frac{\kappa_a}{\kappa_e - q\kappa_s}\left(1 - \exp((-\kappa_e + q\kappa_s) \cdot d_0 \cdot \sec\theta)\right) \quad \textbf{(6.3)}$$

where T_{phys} is the physical temperature, 1/L is the attenuation, κ_a is absorption coefficient, which is determined from complex dielectric constant of dry snow, κ_s is scattering coefficient, κ_e is extinction coefficient, θ is the incidence angle from nadir and q is an empirical constant defining the total forward scattered incoherent intensity in the snowpack (Lemmetyinen et al., 2010). For snow, the empirical parameter (q) in equation (6.2) has been estimated as q = 0.96 by fitting the HUT model to experimental snow slab emission data (Gunn et al., 2010). By simplifying equation (6.2), the emission from a layer consisting of pure ice (q = 1) can be obtained from

$$T_{ICE} = T_{phys}(1 - \exp((-\kappa_a) \cdot d_0 \cdot \sec\theta)) \quad \textbf{(6.4)}$$

where T_{ICE} is the physical ice temperature (Lemmetyinen et al., 2010).

Forward simulations of T_B at 18.7 GHz (H-pol and V-pol) were performed at the three lake ice sites falling within the footprints of AMSR-E. Mean daily air temperature from meteorological stations, and ice thickness and snow depth estimated with CLIMo were used as forcing variables in HUT simulations for seven winters (2002-2009). All other parameters required by HUT, except the root-mean-square (RMS) roughness of ice, were kept constant (e.g. snow density = 0.3 g/cm^3, ice density = 0.916 g/cm^3, snow grain size = 1 mm). Forward simulations were carried out by setting the RMS roughness of ice at 0 mm first and then 1 mm to account for possible roughness effects at the ice/water interface. An additional simulation was performed by keeping the daily air temperature constant at -5 ^{o}C for the full length of the ice seasons to examine if the oscillating behavior of T_B is indeed related to the temperature-dependent imaginary part of the index of refraction of ice (Chang et al., 1997). To minimize the possibility of wet snow which affects T_B, only days where the maximum air temperature was below -1^{o}C were considered for comparison between HUT forward simulations and AMSR-E T_B.

6.3.3 Development and evaluation of ice thickness retrieval algorithm

The ice thickness retrieval algorithm was developed and evaluated using simple linear regression where the independent (predictor) variable consists of AMSR-E T_B data. Since much of the general trajectory and variability in T_B during the ice season can be explained by ice thickening and the temperature-dependent oscillatory pattern (see **Figure 6.3**), as demonstrated by Kang et al. (2010) and forward simulation results with the HUT model (described in section 6.4), two sets of regression equations were developed; one that combines AMSR-E T_B data from both GBL and GSL sites, referred to as Global, and the other one called Regional which consists of two separate equations (one for GBL and one for GSL). The later were derived to account for possible differences due to the latitudinal position of the lakes and the corresponding temperature differences.

When ground-based measurements are few or non-existent, lake ice models such as CLIMo provide a means to develop and evaluate predictive equations of ice thickness from space-

borne T_B measurements. We used ice thickness estimates from CLIMo along with AMSR-E T_B data at three sites/pixels (see **Figure 6.1**) on a daily basis and over seven ice seasons (2002-2009) for this purpose. The approach is based on the use of "training" paired observations to develop the predictive regression equations and independent paired observations at AMSR-E pixels to evaluate the equations. Two sampling strategies were considered for the selection of paired observations. First, the AMSR-E pixels from each GBL and GSL site were randomly selected from all days available over the seven ice seasons as "training" pixels (70 percent) to develop the predictive equations of ice thickness from T_B, and another set of pixels (30 percent) was chosen for evaluating the equations. The 70/30 percent random sampling was repeated 10 times to better assess the predictive capabilities of the equations. Second, the paired observations of AMSR-E pixels and CLIMo from the first six of the seven ice seasons (i.e. 2002-2003 to 2007-2008) were chosen as "training" years and those from the seventh year (2008-2009) to evaluate out-of-sample prediction. This was repeated seven times by iterating between the six "training" years and the out-of-sample year.

Three statistical indices were then calculated as measures of performance of the predictive (regression) equations, including their validation against the *in situ* ice thickness measurements, and also for comparison between HUT forward simulation results and AMSR-E T_B values. The indices include the refined version of the index of agreement (d_r) (Willmott et al., 2011), the root mean square error (RMSE) and the mean bias error (MBE). d_r is intended to be a descriptive measure in the evaluation of model performance, ranging from -1 (worst performance) and 1 (best possible performance).

$$d_r = \begin{cases} 1 - \dfrac{\sum_{i=1}^{N} |P_i - O_i|}{c \sum_{i=1}^{N} |O_i - \bar{O}|}, & \text{when } \sum_{i=1}^{N} |P_i - O_i| \le c \sum_{i=1}^{N} |O_i - \bar{O}| \\ \dfrac{c \sum_{i=1}^{N} |O_i - \bar{O}|}{\sum_{i=1}^{N} |P_i - O_i|} - 1, & \text{when } \sum_{i=1}^{N} |P_i - O_i| > c \sum_{i=1}^{N} |O_i - \bar{O}| \end{cases} \quad \textbf{(6.5)}$$

P_i *and* O_i are the predicted (modeled) and observed values, respectively. $\bar{O}$ is the average observed value, N is the number of paired data used for model evaluation, and $c = 2$. The d_r statistics expresses the sum of the magnitudes of the differences between the model-predicted and observed deviations about the observed mean relative to the sum of the magnitudes of the perfect-model ($P_i = O_i$, for all i) and observed deviations about the observed mean (Willmott et al., 2011).

$$\text{RMSE} = \sqrt{\frac{\sum_{i=1}^{N} (P_i - O_i)^2}{N}} \quad \textbf{(6.6)}$$

$$\text{MBE} = \frac{\sum_{i=1}^{N} [P_i - O_i]}{N} \quad \textbf{(6.7)}$$

The RMSE is a measure of non-systematic error; for example, if there is no deviation between the simulated and observed values, the RMSE value will be zero. The MBE provides a measure of systematic error, indicating whether a model under-predicts

(negative value) or over-predicts (positive value). Both the RMSE and MBE values are reported in the units of the variable of interest (either in cm for ice thickness or K for T_B in this study). Following development and evaluation of the linear regression equations (Global and Regional) they were applied to map ice thickness on a monthly basis (January-April) on both GBL and GSL.

6.4 Results and discussion

6.4.1 General Sensitivity of AMSR-E T_B to ice thickness

The AMSR-E T_B measurements from the three frequencies (6.9, 10.7, and 18.7 GHz) and two polarizations (H-pol and V-pol), along with corresponding CLIMo simulated lake ice thicknesses, are presented in **Figure 6.4** and **Table 6.2**. Coefficient of determination (R^2) values found in **Table 6.2** indicate that a large proportion of the variations in AMSR-E T_B can be explained by ice thickness, particularly at the 18.7 and 10.7 frequencies. R^2 values are moderately lower (0.52-0.93; average 0.77-0.79) and the slope of the relation smaller (0.08-0.18 K • cm^{-1}; average 0.10-0.13 K • cm^{-1}) at 6.9 GHz compared to the higher frequencies. R^2 values are generally of the same order of magnitude at 10.7 GHz and 18.7 GHz. At 10.7 GHz, R^2 values are overall larger (0.77-0.98; average 0.90) and with steeper slopes (0.16-0.28; average 0.22) at H compared to V polarization (R^2: 0.70-0.96; average 0.88 – Slopes: 0.10-23; average 0.17 K • cm^{-1}). In the case of the 18.7 GHz frequency, the slopes also tend to be steeper at H polarization (0.17-0.41; average 0.30 K • cm^{-1}) but the R^2 values larger at V polarization (0.81-0.98; average 0.92). A tentative explanation for the lower R^2 values at 6.9 GHz may be due to the fact that the AMSR-E footprint at this frequency covers a larger area (74 km x 43 km) than at 10.7 GHz (51 km x 30 km) and 18.7 GHz (27 km x 16 km), such that it encompasses a greater range of ice thicknesses for the T_B value recorded by the sensor compared to the single ice thickness values simulated with the 1-D lake ice model on the corresponding days.

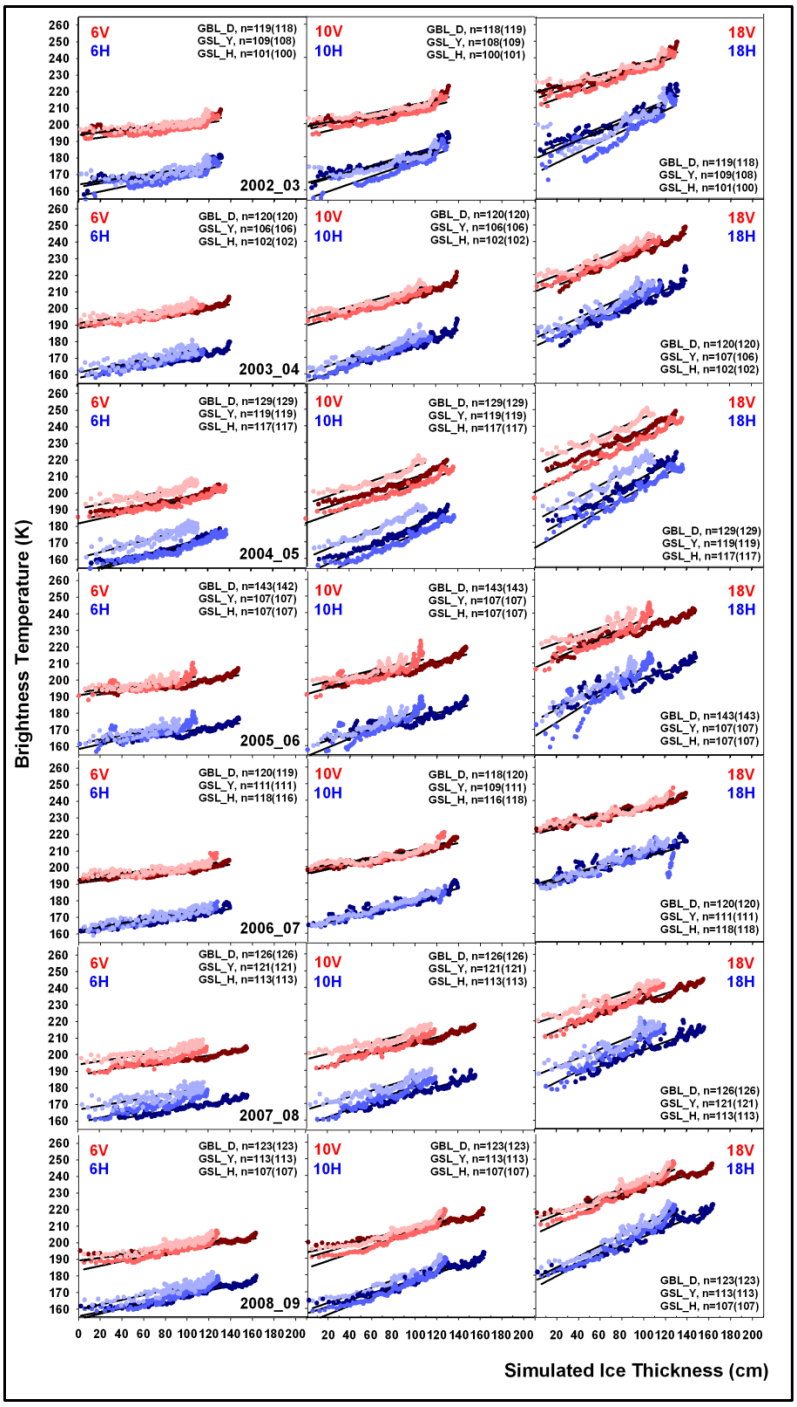

Figure 6.4: Plots of AMSR-E T_B and simulated ice thickness from CLIMo between ice-on and melt-onset dates for seven ice seasons (2002 to 2009; top to bottom graphs). Blue symbols are for H-pol (GBL_D: dark blue; GSL_Y: medium blue; GSL_H: light blue) and red symbols for V-pol (GBL_D: dark red; GSL_Y: medium red; GSL_H: light red). Coefficient of determination (R^2) and slope of relation values for each plot are given in Table 6.2.

Interestingly, the strength of the relation between T_B and ice thickness (simulated with CLIMo) is somewhat stronger for colder (e.g. 2003-2004) than for warmer winters (e.g. 2005-2006) at any of the frequencies and polarizations examined (i.e. higher R^2 values; see **Table 6.2, Figures 6.4 and 6.5**), showing the influence of inter-annual climate variability on the strength of the relation (although still very high in most cases). As an example, T_B values exhibit greater intra-seasonal variability during winter 2005-2006 (warmer) compared to 2003-2004 (colder) (see **Figure 6.5**) due to larger fluctuations in air temperature during the later ice season. Looking at the three sampling sites in the two large lakes, the GBL site generally shows the strongest relation between T_B and ice growth/thickening at the frequencies examined (**Table 6.2**). Plots of 18.7 GHz V-pol for ice season 2003-2004 (**Figure 6.5a to Figure 6.5c**) show relatively less intra-seasonal variability of T_B with ice growth than during 2005-2006 (**Figure 6.5d to Figure 6.5f**). In addition, the higher R^2 values for GBL (**Figures 6.5a and 6.5d**) reveal somewhat less variability in T_B with ice thickness than at the two sites in GSL.

Given the strength of the relation between AMSR-E TB at 18.7 GHz and simulated ice thickness as illustrated above, and in the perspective of developing long time series of ice thickness estimates from passive microwave satellite sensors operating in the 18-19 GHz range (e.g. SSM/I and SMMR, 1978-present) as a climate data record, this frequency is of particular interest to form the basis of a retrieval algorithm.

Table 6.2: Coefficient of determination (R^2) and slope of relation between AMSR-E T_B and ice thickness from CLIMo (2002-2009) for sampling footprints at GBL_D (Deline), GSL_Y (Yellowknife), and GSL_H (Hay River). Slopes (K cm^{-1}) are in brackets

GBL-D	6.9V	6.9H	10.7V	10.7H	18.7V	18.7H
0203	0.73(0.08)	0.76(0.11)	0.86(0.15)	0.86(0.19)	0.91(0.21)	0.89(0.27)
0304	0.89(0.10)	0.86(0.12)	0.95(0.19)	0.92(0.21)	0.96(0.26)	0.91(0.30)
0405	0.91(0.14)	0.93(0.18)	0.94(0.22)	0.96(0.28)	0.97(0.29)	0.96(0.36)
0506	0.80(0.09)	0.78(0.09)	0.89(0.16)	0.84(0.16)	0.90(0.19)	0.85(0.21)
0607	0.87(0.08)	0.84(0.10)	0.91(0.13)	0.88(0.17)	0.93(0.15)	0.88(0.19)
0708	0.92(0.09)	0.91(0.11)	0.96(0.16)	0.93(0.19)	0.95(0.21)	0.90(0.25)
0809	0.87(0.08)	0.92(0.13)	0.94(0.14)	0.95(0.20)	0.97(0.18)	0.95(0.26)
GSL-Y	6.9V	6.9H	10.7V	10.7H	18.7V	18.7H
0203	0.72(0.09)	0.74(0.14)	0.86(0.16)	0.82(0.23)	0.93(0.23)	0.83(0.32)
0304	0.88(0.11)	0.88(0.14)	0.96(0.19)	0.96(0.23)	0.97(0.27)	0.93(0.31)
0405	0.90(0.15)	0.92(0.18)	0.95(0.23)	0.96(0.28)	0.98(0.32)	0.92(0.37)
0506	0.52(0.10)	0.65(0.15)	0.70(0.19)	0.78(0.27)	0.84(0.29)	0.82(0.41)
0607	0.68(0.09)	0.90(0.12)	0.80(0.15)	0.93(0.17)	0.88(0.17)	0.60(0.17)
0708	0.86(0.12)	0.84(0.14)	0.93(0.20)	0.93(0.23)	0.95 (0.28)	0.91(0.33)
0809	0.85(0.14)	0.88(0.16)	0.91(0.22)	0.93(0.26)	0.95(0.30)	0.94(0.34)
GSL-H	6.9V	6.9H	10.7V	10.7H	18.7V	18.7H
0203	0.60(0.08)	0.55(0.10)	0.78(0.14)	0.77(0.17)	0.84(0.18)	0.74(0.27)
0304	0.71(0.10)	0.68(0.13)	0.89(0.18)	0.92(0.22)	0.93(0.25)	0.91(0.31)
0405	0.75(0.13)	0.81(0.17)	0.88(0.23)	0.95(0.28)	0.92(0.28)	0.93(0.36)
0506	0.58(0.09)	0.61(0.12)	0.77(0.16)	0.89(0.23)	0.81(0.23)	0.81(0.35)
0607	0.60(0.06)	0.79(0.11)	0.86(0.10)	0.98(0.18)	0.89(0.14)	0.96(0.24)
0708	0.71(0.10)	0.63(0.11)	0.89(0.17)	0.89(0.19)	0.92(0.22)	0.88(0.27)
0809	0.82(0.12)	0.78(0.14)	0.93(0.19)	0.91(0.23)	0.94(0.26)	0.92(0.33)
AVG (02-09)	0.77(0.10)	0.79(0.13)	0.88(0.17)	0.90(0.22)	0.92(0.23)	0.88(0.30)

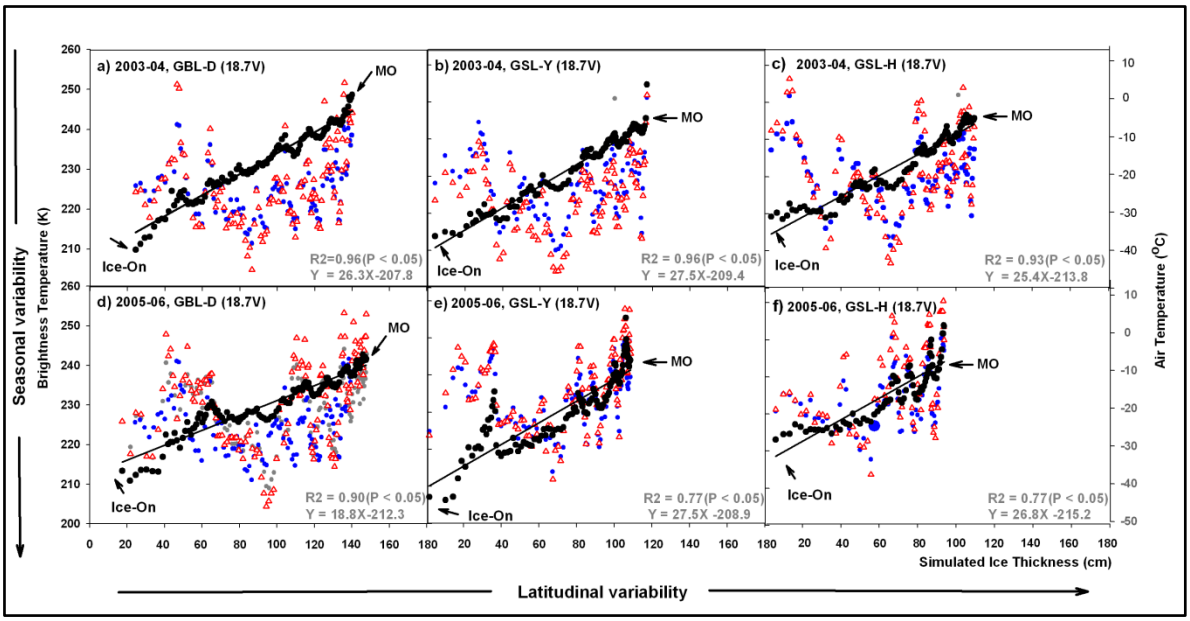

Figure 6.5: Plots of AMSR-E T_B at 18.7 GHz (V-pol) and simulated ice thickness with CLIMo for a cold (2003-2004; top) and a warm (2005-2006; bottom) winter season at GBL_D (left), GSL-Y (center), and GSL_H (right) sampling footprints. The blue and red symbols represent the daily mean and maximum air temperature, respectively (with scale on secondary y axis, right hand side of figure).

6.4.2 AMSR-E TB versus HUT forward simulations

In **Figure 6.6**, the temporal evolution T_B at 18.7 GHz from AMSR-E at horizontal (upper) and vertical (middle) polarizations is compared to that from HUT forward simulations (0 and 1 mm RMS, and constant -5^{o}C with 0 mm RMS) over the same period for GBL. Similar to the AMSR-E time series, T_B values derived with HUT forward simulations also show the oscillatory pattern earlier attributed to the temperature-vulnerable absorption length of ice. In support of this explanation, a HUT simulation under a constant rather than variable wintertime air temperature of -5^{o}C (with 0 mm RMS) was performed. Results from this simulation reveal a constant increase in T_B with ice growth at both H and V polarizations without the oscillatory pattern due to air temperature variability as observed during the ice season. While AMSR-E observations at 18.7 GHz (H-pol) match relatively well HUT derived T_B*s* for GBL (2003-2004), those at V-pol are about 15-20 K higher than HUT simulations with a RMS roughness of ice 0 mm (middle, **Figure 6.6**). HUT simulated

T_B values with a RMS of 1 mm tend to match those of AMSR-E quite well at V-pol during the middle/late ice growth/thickening season. A tentative explanation for the differences is that roughness effects represented with a 1 mm RMS are more prominent later in the ice season while they are less so earlier in the winter and, therefore, more closely match the 0 mm RMS at the GBL site.

The temporal evolution of AMSR-E T_B values is compared in more details with that of HUT at 18.7 GHz (H-pol and V-pol; 0 mm and 1 mm RMS) for all three sites (GBL_D, GSL_Y, and GSL_H) during the seven ice growth seasons (2002-2009) (**Figure 6.7**). Both the time series of AMSR-E and HUT T_B illustrate the oscillatory pattern from the temperature-vulnerable absorption length of ice. Overall, HUT simulated T_B values at H-pol with 0 mm RMS and at V-pol with 1 mm RMS provide the closest match with AMSR-E T_B*s*. The H-pol T_B*s* (with 0 mm) over the entire ice growth season and V-pol T_B*s* (with 1 mm) during the middle/late ice growth/thickening season show the closest correspondence between AMSR-E and HUT simulations (**Figures 6.7)**. The d_r statistics indicates better performance of HUT model simulations at 18.7 GHz (V-pol) with 1 mm RMS (d_r = 0.47-0.60) than at H-pol (d_r = 0.25-0.44), while with 0 mm RMS H-pol (d_r = 0.40-0.63) provides superior performance than V-pol (d_r = -0.22-0.17) **(Table 6.3**). The RMSE and MBE statistical measures indicate that HUT simulations with a 0 mm RMS are closer to AMSR-E at H-pol (MBE: -6.44 to -10.84 K; RMSE: 8.30 to 11.90 K). For V-pol, smaller biases are found with a 1 mm RMS (MBE: -7.05 to -9.35 K; RMSE: 8.57 to 11.16 K).

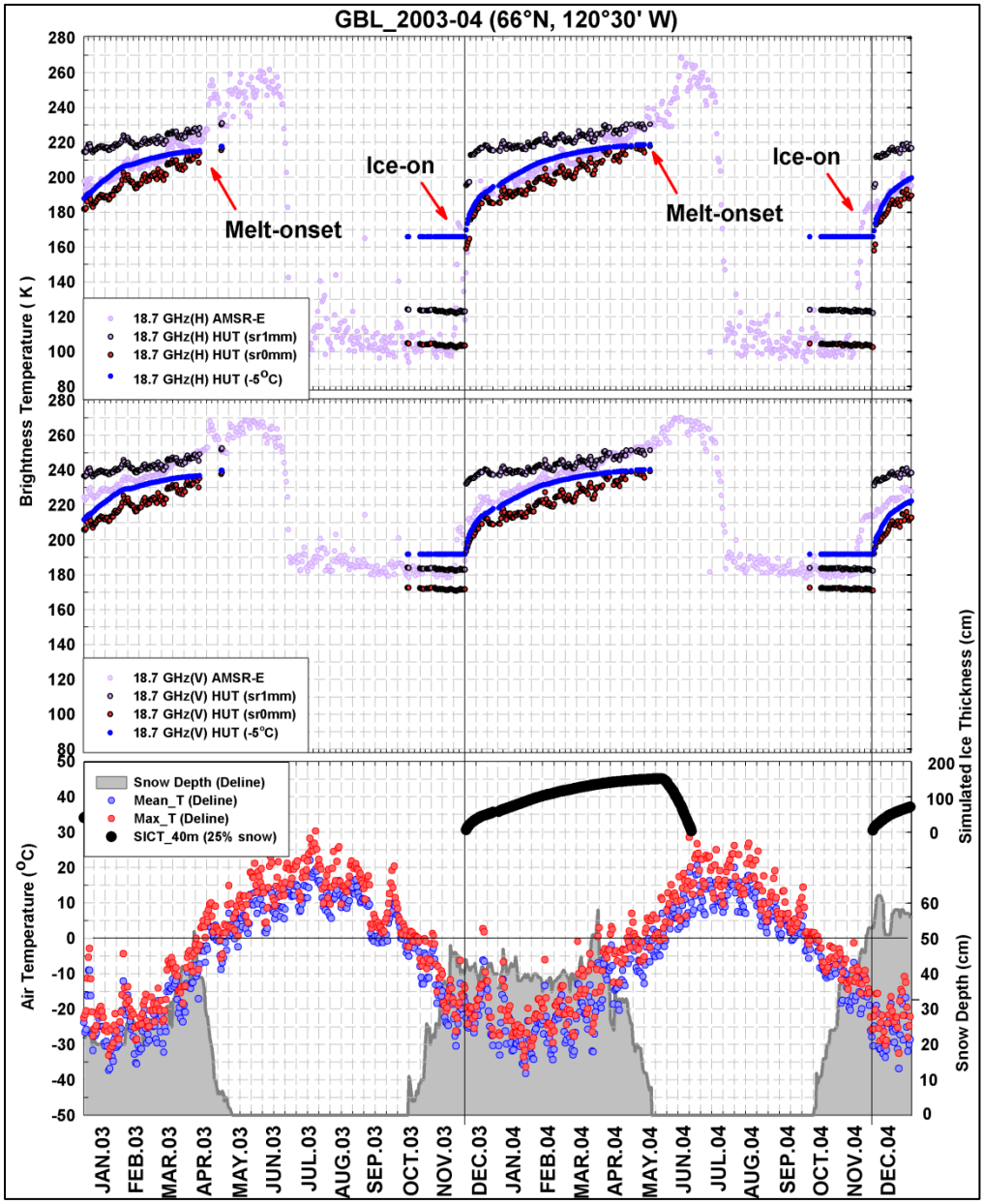

Figure 6.6: Temporal evolution of AMSR-E T_B at 18.7 GHz (light purple) in comparison with HUT simulated T_B at 18.7 GHz with RMS roughness of ice 0 mm (dark circle red) and 1 mm (dark circle blue) at both horizontal (top panel) and vertical (middle panel) polarizations at sampling site nearby Deline at GBL (2003-2004). HUT simulated T_B using a constant air temperature (-5°C) is shown in blue (top and middle panels). The time series of maximum (Max_T, red) and mean (Mean_T, blue) air temperatures obtained at the Deline meteorological station is shown in the bottom panel along with snow depth (grey). Simulated ice thicknesses obtained with CLIMo are represented by the thick black curve.

The HUT forward simulations indicate that results at H and V polarizations are comparable. Without intensive field measurement campaigns that would allow for characterization of variable ice thickness and ice type (Gunn et al., 2010) within the AMSR-E footprints, it is difficult to clearly show through HUT simulations performed in this study that V-pol is more sensitive to ice thickness than H-pol as it was suggested from the statistical analysis described in the previous section. It is clear, however, that the 18.7 GHz frequency is sensitive to the seasonal evolution of ice thickness on the two larger northern lakes. This is supported by both the statistical analysis and HUT forward simulation results. Also, V-pol is known to be less sensitive to surface roughness than H-pol suggesting that V-pol is better suited for the estimation of ice thickness.

Table 6.3: Comparison of HUT simulated and AMSR-E T_B at 18.7 GHz (H- and V-pol) for sampling footprints at GBL_D (Deline), GSL_Y (Yellowknife), and GSL_H (Hay River). The top and bottom tables show results with RMS roughness of 0 mm and 1 mm.

0mm	GBL-D		GSL-Y		GSL-H	
roughness	18.7H	18.7V	18.7H	18.7V	18.7H	18.7V
RMSE (cm)	8.56	13.74	8.30	13.88	11.90	17.19
MBE (cm)	-6.93	-13.05	-6.44	-13.49	-10.84	-16.72
I_a	0.56	0.02	0.63	0.17	0.40	-0.22
1mm	GBL-D		GSL-Y		GSL-H	
roughness	18.7H	18.7V	18.7H	18.7V	18.7H	18.7V
RMSE (cm)	16.54	9.91	18.69	11.16	15.75	8.57
MBE (cm)	-15.08	-8.46	-16.77	-9.35	-13.58	-7.05
I_a	0.26	0.47	0.25	0.48	0.44	0.60

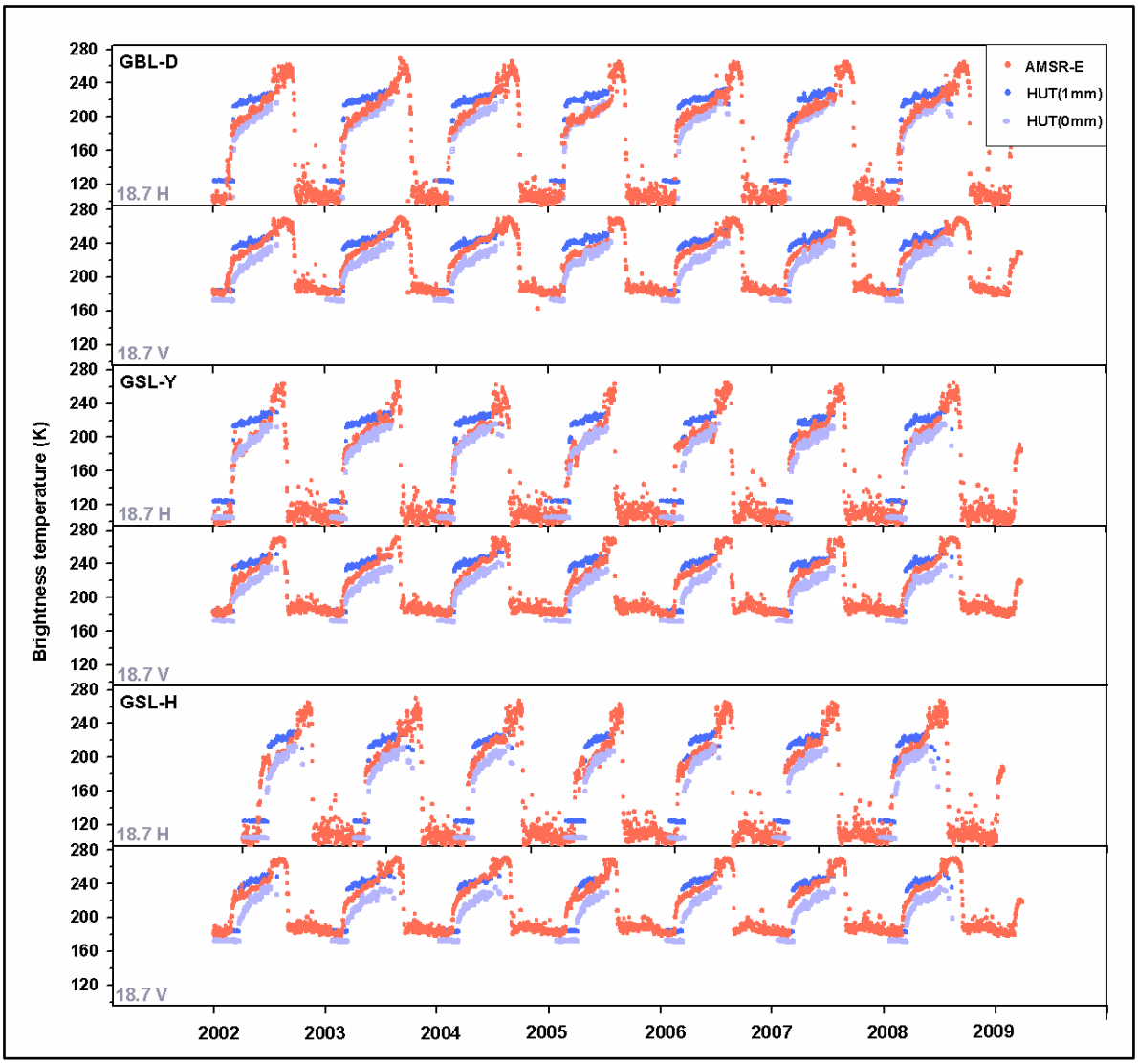

Figure 6.7: Comparison between AMSR-E T_B (red dots) and HUT simulated T_B (blue dots) at 18.7 GHz (H-pol and V-pol) from 2002-2009 with RMS roughness of ice 0 mm (light blue) and 1 mm (blue) for all three sites, GBL_D (Deline, top) and GSL_Y (Yellowknife, middle) and GSL_H (Hay River, bottom).

6.4.3 Ice thickness equations and their evaluation

The AMSR-E T_B at 18.7 GHz V-pol is the predictor variable that forms the basis of the ice thickness retrieval equations. Three regression-based equations of ice thickness are proposed based on available paired observations (AMSR-E T_B and CLIMo simulated ice thickness data at three sampling footprints) from all seven ice seasons; one that combines GBL and GSL into a single equation (ICT_{Global}) and one for each GBL (ICT_{GBL}) and GSL (ICT_{GSL}):

$$ICT_{Global} = 3.75 \times T_B - 790.308 \quad \textbf{(6.8)}$$

$$ICT_{GBL} = 4.13 \times T_B - 869.906 \quad \textbf{(6.9)}$$

$$ICT_{GSL} = 3.22 \times T_B - 672.048 \quad \textbf{(6.10)}$$

Equations 6.8-6.10 were developed by averaging T_B values of the same Julian day for the seven ice seasons (lower panels of **Figure 6.8**), therefore reducing the oscillatory behavior of brightness temperatures observed in each individual year due to air temperature variability (upper panels of **Figure 6.8**). The reasoning behind the three separate equations is due to the fact that the slope of the relation between T_B and simulated ice thickness with CLIMo is different for GBL than for GSL. The rate of change for GBL (4.13 cm per Kelvin) is slightly greater than that for GSL (3.22 cm per Kelvin) due to differences in regional climate (the middle and right lower panels of **Figure 6.8**). Combining data from both lakes (ICT_{Global}) results in a slope of 3.75 cm per Kelvin. Equation 6.8 may therefore be more applicable for a first guess prediction of ice thickness on other large lakes found at high latitudes where no previous equations have been developed, while equations 6.9 and 6.10 present a refinement for the specific lakes.

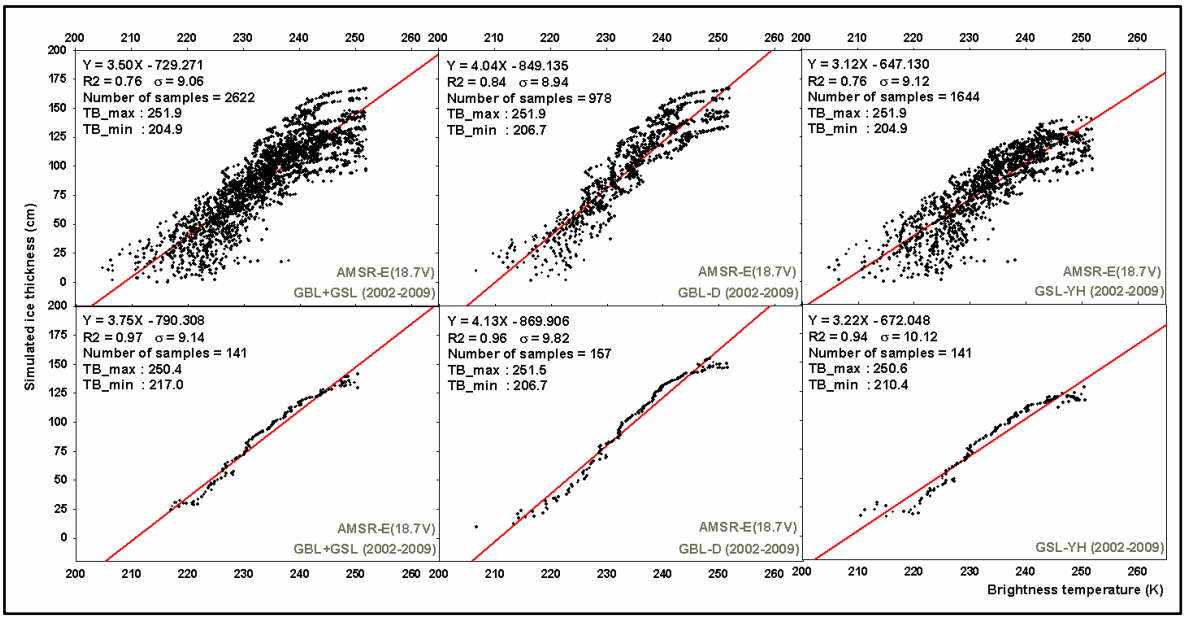

Figure 6.8: Linear regression plots between simulated lake ice thickness (y-axis) from CLIMo and AMSR-E T_B (upper x-axis) at 18.7 GHz (V-pol) from 2002-2009 are shown in the upper panels for all three lake sites combined (top left), GBL_D (Deline, top middle), GSL_YH (Yellowknife and Hay River, top right). Daily T_B values averaged from seven years are shown in the bottom panels. Predictive equations, coefficient of determination (R^2) and standard deviation (σ) values, as well as the number of paired T_B observations and simulated ice thicknesses, and maximum (minimum) T_B values are also shown on the plots.

Figure 6.9 presents a comparison between ice thickness predicted with the global (top panel) and regional (lower panel) regression equations and *in situ* measurements from a limited number of sites and years (described earlier in 3.1.3). Results from the application of regional equations to GBL and GSL show slightly better estimates (RMSE = 19.33 cm, MBE = 7.94 cm, and d_r = 0.67) than using the global equation (RMSE = 23.33 cm, MBE = 13.42 cm, and d_r = 0.59). In both cases the equations over-predict ice thicknesses, although the issue of AMSR-E footprint size versus limited-area *in situ* sampling must be kept in mind when interpreting these results.

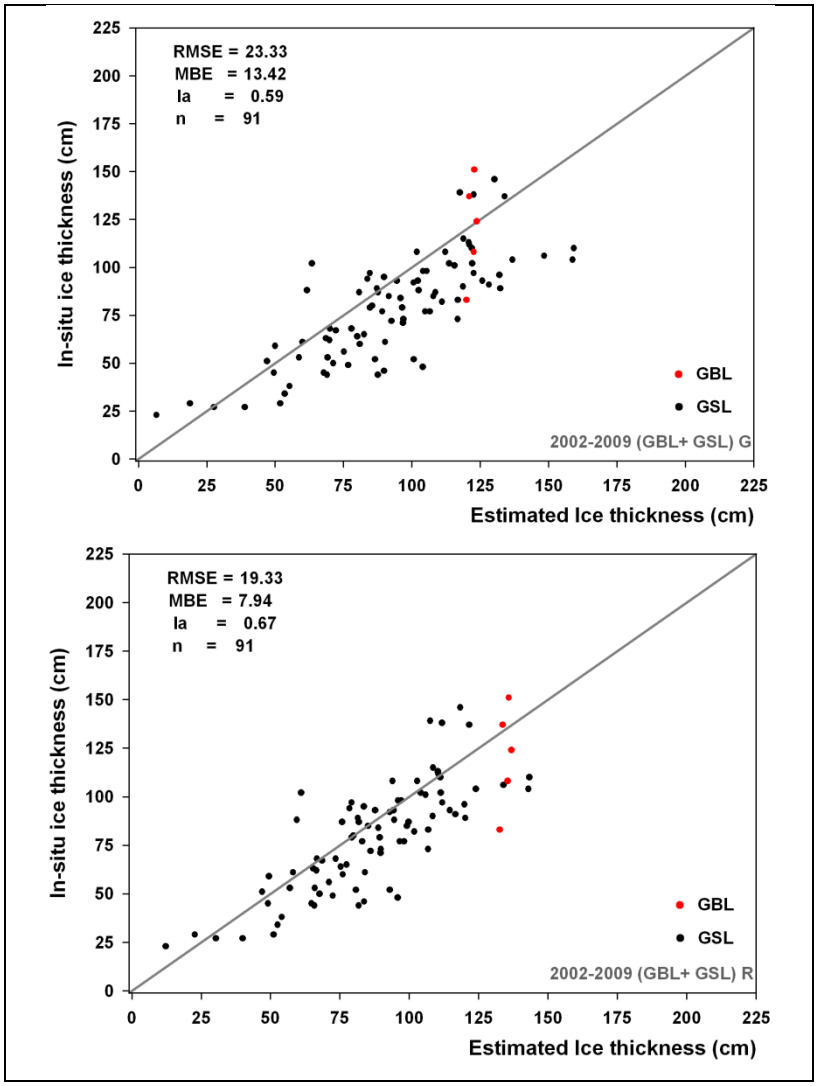

Figure 6.9: Comparison between estimated ice thicknesses from linear regression equations applied to AMSR-E 18.7 GHz V-pol T_B and in-situ measurements for Great Bear Lake (five measurements in 2007, in red) and Great Slave Lake (Back Bay, 2002-2009, in black). The top panel shows results using the global equation (GBL and GSL combined) and the lower panel using two regional equations (GBL and GSL separately).

Table 6.4: Comparison of ice thickness from regression-based on 18.7 GHz V-pol T_B and independent estimates from CLIMo for GBL_D, GSL_Y, and GSL_H sites (2002-2009). The upper section of the table presents average statistical indices calculated from training/validation (70%/30%) while the lower section shows those from out-of-sample prediction (6 years/7th year).

	GBL_D	GSL_Y	GSL_H
T_B 70%/30%	18.7V	18.7V	18.7V
RMSE (cm)	15.41	12.61	14.78
MBE (cm)	-0.22	0.08	-0.13
d_r	0.81	0.83	0.77
6yrs/7th	18.7V	18.7V	18.7V
RMSE (cm)	18.12	14.41	16.12
MBE (cm)	1.87	1.34	3.50
d_r	0.77	0.80	0.74

Since *in situ* measurements of ice thickness are limited for the period of study (n=91), a second verification of the performance of the linear regression equations was performed where AMSR-E T_B measurements on all dates over the seven ice seasons (2002-2009) from the three sampling footprints on GBL and GSL were randomly selected 10 times with 70 percent training pixels to develop predictive equations of ice thickness from T_B (10 equations for each of GBL_D, GSL_Y and GSL_H, not shown) and the remaining 30 percent of pixels used for validation (see details in 3.3). This was also verified using the out-of-sample approach where six years of T_B measurements were used to develop the predictive equations (seven equations for each of GBL_D, GSL_Y and GSL_H, not shown) and the seventh year used for validation (repeated seven times by changing the out-of-sample year from Year 1 to Year 7). Results from this evaluation are reported in **Table 6.4** as the median values of the statistics calculated from the 10 random selections of 70% training/30% validation (top portion of table) and seventh out-of-sample year strategy (bottom portion of table) for GBL_D, GSL-Y, and GSL_H. The index of agreement (d_r) indicates that the linear regression equations perform very well at predicting ice thickness

on both GBL and GSL with d_r = 0.77-0.83 (70%/30% strategy) and d_r = 0.74-0.80 (out-of-sample strategy). The MBE (1.34-3.50 cm) and RMSE (14.41-18.12 cm) values are slightly larger for predictions using out-of-sample years. A better performance is achieved with ice thickness predictions from the 70% training/30% validation approach (MBE: -0.22-0.08 cm, RMSE: 12.61-15.41 cm). The above results strongly justify the use of simple linear regression equations for mapping ice thickness on GBL and GSL.

6.4.4 Monthly ice thickness mapping

One advantage of the regression-based equations developed in this study is that they can be applied to map spatial patterns of ice thickness across large lakes throughout the winter period using a single predictor variable (e.g. satellite-based passive microwave T_B data). This is in comparison to 1-D thermodynamic ice models such as CLIMo that require meteorological forcing variables and information on lake depth that are often not available for high-latitude regions. The regression equations (Eq. 6.8, 6.9, and 6.10) were applied to map monthly ice thickness on GBL and GSL (**Figures 6.10 and 6.11)**. The maps show the gradual increase of ice thickness from January to April (averages calculated from all ice seasons) due to increasing emissivity with ice growth (thickening). The maps on the left-hand side of **Figures 6.10 and 6.11** were produced using the global equation while those on the right-hand side using the regional equations. Application of the global equation results in 10-15 cm thinner ice on GBL and 10-15 cm thicker ice estimates on GSL for each month, compared to the application of the lake-specific (regional) equations. In general, monthly ice thicknesses are on average 5-15 cm thicker for GBL than for GSL. Also noteworthy is that the spatial variability of ice thickness across both lakes diminishes once lake ice growth slows down (less conductive heat loss with thicker ice) in March and April.

Other than the important role of air temperature (see **Table 6.1**) as a controlling factor on ice growth, spatial patterns in ice thickness observable for each month on both GBL and GSL (**Figures 6.10 and 6.11**) can be explained by the combination of at least two other factors, lake depth and on-ice snow depth. The influence of lake depth is particular evident during the early ice growth period (January and to a lesser extent February). For the same

time period, thicker ice forms in the shallower sections of the lakes. Thinner ice can generally be found in the deeper sections of both lakes that form an ice sheet later in the late fall to early winter period (Kang et al., 2012). The bathymetry maps of GBL and GSL (see **Figure 6.2**) provide support for this observation. Thinner ice can be seen for the deepest sections of GBL (e.g. McTavish Arm, Keith Arm), and the eastern part of the main body of GSL. Due to its insulating role the presence of snow on ice is also known to influence the seasonal evolution of ice thickness (e,g Brown and Duguay, 2010). Rouse et al. (2008b) report that the end-of-winter maximum ice thickness can vary by as much as 50-60 cm across GBL and GSL, and perhaps even more, just due to the variable snow depth conditions which are strongly controlled by redistribution by wind on the ice surface. Late winter (April) ice thickness maps generated with the regional equations show thicker ice in the central basin of GSL and a section of McTavish Arm in GBL that is likely related to the presence of thinner snow on ice in these areas of the lakes. The reason for this suggestion is that for these same areas of GBL and GSL the ice was relatively thinner during the early period of ice growth, but has grown thicker by the end of the ice season.

A statistical summary of estimated monthly ice thicknesses for all ice seasons (2002-2009) is provided in **Table 6.5**. Maximum, minimum, and mean estimated ice thickness increase gradually from January to April on both GBL and GSL. The standard deviation of estimated ice thickness is generally higher in January (8.2-17.9 cm) than in other months because ice growth rates are more important and variable across the lakes early in the ice cover period. Estimated ice thicknesses during a warmer winter season (e.g. 2005-2006) are somewhat smaller than in other winter seasons due to later freeze-up in the two lakes (Kang et al., 2012). Otherwise late winter ice thicknesses are found to be somewhat larger in April 2004, 2005 and 2009, which is likely due to the particularly colder conditions during the early ice seasons of these years. As indicated earlier, snow is also an important controlling factor of ice growth such that it is at times difficult to determine with certainty which of air temperature or snow is the main variable responsible for the observed ice thickness variations between years.

Table 6.5: Monthly estimates of ice thickness from global and regional (in brackets) equations for GBL and GSL. Indicated are maximum (Max), minimum (Min), average (Average), and standard deviation (STDEV) of ice thickness from January to April, 2003-2009.

	GBL (cm)	Average *TB* ICT				GSL (cm)	Average *TB* ICT			
		JAN	FEB	MAR	APR		JAN	FEB	MAR	APR
2003	Max	117.6 (100.7)	102.9(103.2)	117.1(117.1)	142.1(140.1)	Max	100.7(93.0)	103.2(95.2)	117.1(107.1)	140.1(126.8)
	Min	47.5 (48.1)	67.8(58.5)	81.3(81.7)	107.0(103.3)	Min	48.1(47.8)	58.5(56.8)	81.7(76.7)	103.3(95.2)
	Average	68.7 (66.1)	85.7(80.5)	105.8(101.7)	131.3(126.7)	Average	66.1(63.3)	80.5(75.7)	101.7(93.9)	126.7(115.4)
	STDEV	11.0 (11.4)	5.8(9.0)	7.3(7.1)	6.6(6.8)	STDEV	11.4(9.8)	9.0(7.7)	7.1(6.1)	6.8(5.8)
2004	Max	119.8 (120.6)	117.3(132.2)	115.8(129.2)	144.0(147.2)	Max	120.6(110.1)	132.2(120.1)	129.2(117.5)	147.2(132.9)
	Min	49.2 (42.9)	85.3(86.2)	95.9(102.8)	106.0(85.6)	Min	42.9(43.4)	86.2(80.6)	102.8(94.8)	85.6(80.1)
	Average	79.4 (70.6)	99.2(100.0)	109.2(112.7)	134.5(129.8)	Average	70.6(67.2)	100.0(92.5)	112.7(103.3)	129.8(118.0)
	STDEV	13.9 (17.9)	5.7(8.7)	3.5(4.3)	5.8(11.1)	STDEV	17.9(15.3)	8.7(7.5)	4.3(3.7)	11.1(9.5)
2005	Max	112.8 (126.3)	113.8(133.1)	137.5(145.5)	150.3(150.3)	Max	126.3(115.0)	133.1(120.8)	145.5(131.5)	150.3(135.7)
	Min	78.6 (66.9)	96.0(96.1)	101.4(114.1)	117.9(124.4)	Min	66.9(64.0)	96.1(89.1)	114.1(104.6)	124.4(113.4)
	Average	88.9 (85.4)	104.7(106.3)	122.6(126.6)	138.0(138.9)	Average	85.4(79.4)	106.3(97.2)	126.6(114.6)	138.9(125.1)
	STDEV	15.1 (9.7)	15.9(6.1)	19.0(5.4)	21.0(4.5)	STDEV	9.7(10.4)	6.1(9.2)	5.4(10.1)	4.5(10.5)
2006	Max	123.0 (114.2)	119.7(119.3)	118.5(130.4)	133.9(147.8)	Max	114.2(104.6)	119.3(109.0)	130.4(118.6)	147.8(133.4)
	Min	50.5 (30.8)	69.7(67.9)	82.0(98.2)	94.7(111.9)	Min	30.8(33.0)	67.9(64.9)	98.2(90.9)	111.9(102.6)
	Average	77.3 (66.9)	93.5(89.1)	101.4(113.6)	117.9(129.3)	Average	66.9(64.0)	89.1(83.0)	113.6(104.1)	129.3(117.6)
	STDEV	15.9 (18.5)	10.7(11.4)	7.6(6.9)	7.6(6.4)	STDEV	18.5(15.8)	11.4(9.8)	6.9(5.9)	6.4(5.5)
2007	Max	132.6 (133.2)	112.9(118.3)	115.2(125.3)	139.5(139.6)	Max	133.2(121.0)	118.3(108.1)	125.3(114.1)	139.6(126.4)
	Min	53.0 (57.2)	66.8(78.6)	89.3(98.4)	115.0(105.9)	Min	57.2(55.7)	78.6(74.1)	98.4(91.1)	105.9(97.5)
	Average	81.9 (86.4)	88.8(94.5)	103.5(112.5)	130.1(126.6)	Average	86.4(80.7)	94.5(87.7)	112.5(103.2)	126.6(115.3)
	STDEV	15.3 (17.8)	8.4(8.2)	4.6(4.4)	4.8(7.3)	STDEV	17.8(15.3)	8.2(7.1)	4.4(3.8)	7.3(6.2)
2008	Max	113.1 (114.8)	103.0(107.3)	120.7(122.1)	142.6(139.8)	Max	114.8(105.2)	107.3(98.7)	122.1(111.4)	139.8(126.6)
	Min	61.2 (64.5)	69.4(83.1)	70.9(95.3)	90.0(86.2)	Min	64.5(61.9)	83.1(77.9)	95.3(88.4)	86.2(80.6)
	Average	81.8 (84.4)	92.1(93.3)	105.3(110.2)	128.1(120.7)	Average	84.4(79.0)	93.3(86.7)	110.2(101.2)	120.7(110.2)
	STDEV	9.5 (11.3)	5.8(4.2)	8.6(5.4)	9.5(11.7)	STDEV	11.3(9.7)	4.2(3.6)	5.4(4.6)	11.7(10.1)
2009	Max	111.8 (121.5)	117.2(126.2)	125.8(124.3)	145.8(148.1)	Max	121.5(110.9)	126.2(115.0)	124.3(113.3)	148.1(133.7)
	Min	69.2 (62.8)	92.5(88.0)	89.0(99.4)	115.3(116.8)	Min	62.8(60.5)	88.0(82.2)	99.4(91.9)	116.8(106.9)
	Average	87.6 (82.0)	105.4(99.5)	112.0(111.8)	137.8(135.6)	Average	82.0(76.9)	99.5(91.9)	111.8(102.5)	135.6(122.9)
	STDEV	8.2 (11.4)	3.6(6.2)	5.0(3.5)	3.3(4.9)	STDEV	11.4(10.1)	6.2(6.0)	3.5(4.3)	4.9(5.5)
2002-2009	Max	118.0(112.0)	107.6(115.3)	115.2(123.9)	136.9(138.2)	Max	112.0(102.7)	115.3(105.6)	123.9(112.9)	138.2(125.2)
	Min	60.8(56.7)	84.2(85.9)	94.7(105.7)	116.0(113.0)	Min	56.7(55.2)	85.9(80.4)	105.7(97.3)	113.0(103.6)
	Average	81.0(77.4)	95.9(94.7)	108.9(112.7)	131.5(129.7)	Average	77.4(73.0)	94.7(87.9)	112.7(103.3)	129.7(117.9)
	STDEV	10.7(13.0)	4.2(5.9)	3.7(3.3)	3.6(4.1)	STDEV	13.0(11.2)	5.9(5.1)	3.3(2.8)	4.1(3.5)

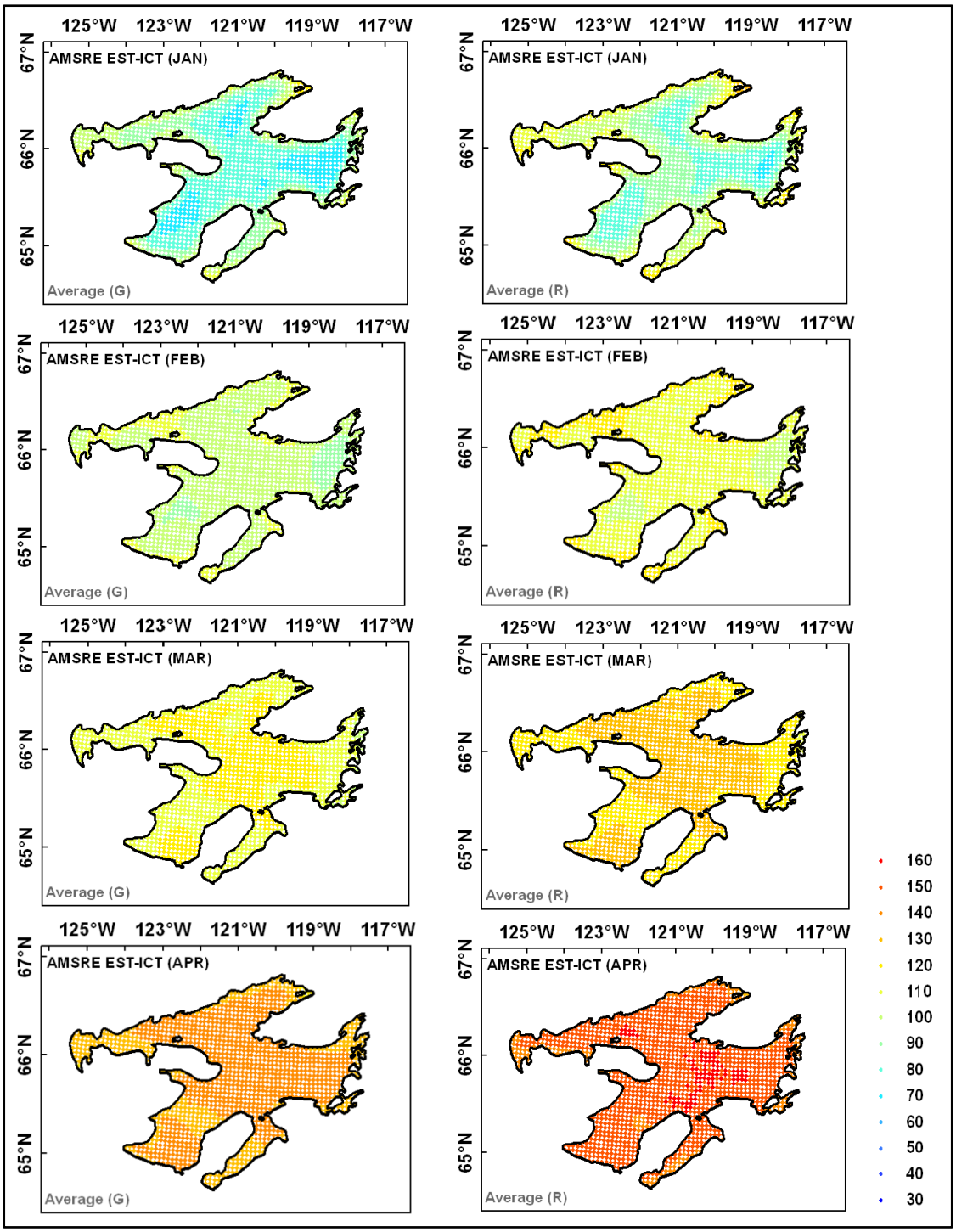

Figure 6.10: AMSR-E derived estimated lake ice thickness monthly maps (from January to April) on average for Great Bear Lake from global equation (left panel) and from regional equation (right panel). The legend is in centimeter (from 30-160 cm).

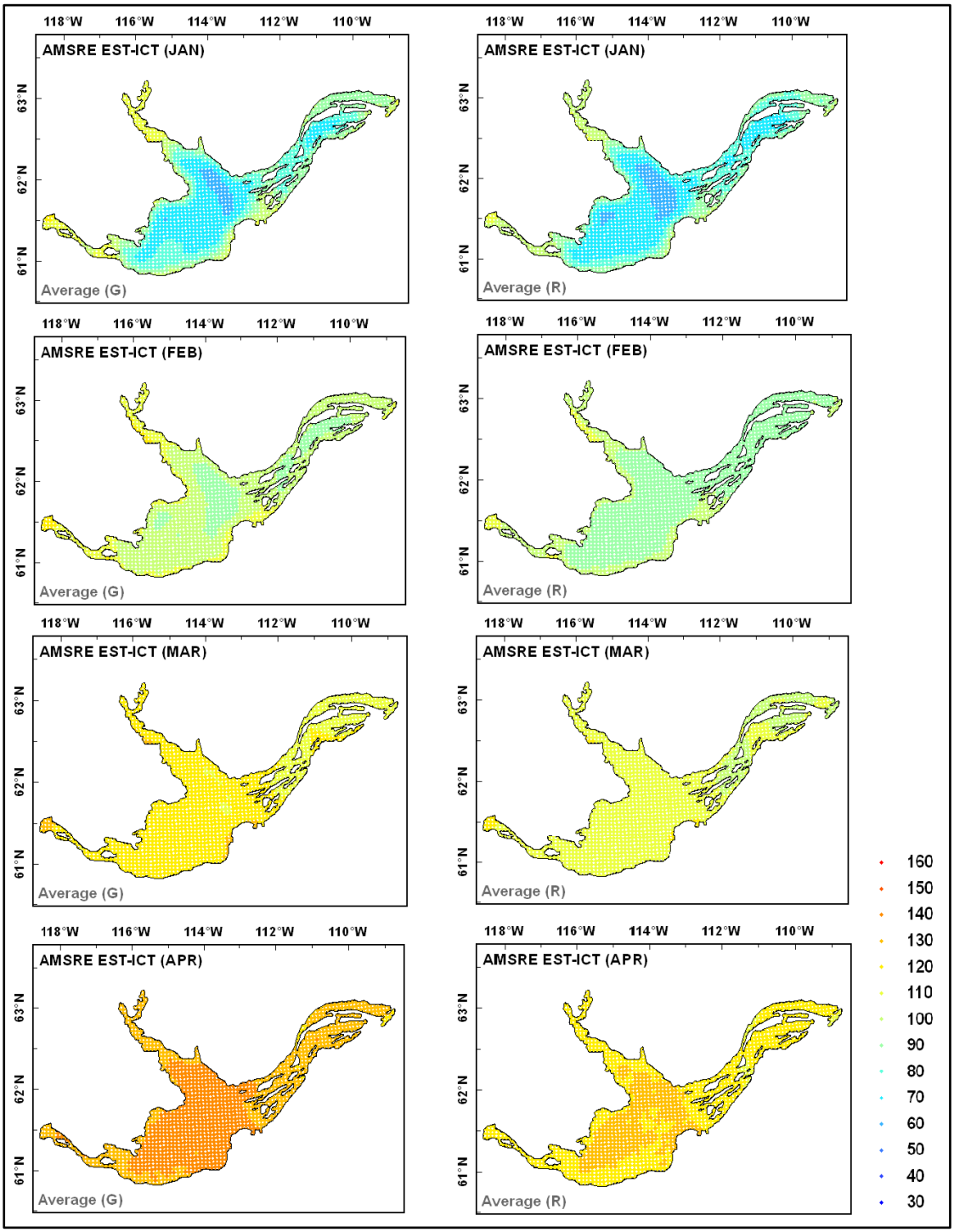

Figure 6.11: AMSR-E derived estimated lake ice thickness monthly maps (from January to April) on average for Great Slave Lake from global equation (left panel) and from regional equation (right panel). The legend is in centimeter (from 30-160 cm).

6.5 Conclusion

The 18.7 GHz (V-pol) was shown to be the most useful AMSR-E channel for estimating ice thickness on GBL and GSL. A statistical analysis revealed that this frequency is sensitive to lake ice growth as a result of the increase in emissivity, and by extension T_B, from the radiometrically colder (thinner) ice to thicker ice later in the ice season. The strength of this relation was demonstrated by comparing AMSR-E T_B data with simulated ice thicknesses obtained with CLIMo on a daily basis over several ice seasons (2002-2009). This was supported by results obtained with HUT forward model simulations that reproduced well the oscillatory pattern observed in AMSR-E T_B time series. HUT simulations of T_B provided further evidence of the sensitivity of the 18.7 GHz frequency to ice thickness, although experiments conducted by setting the RMS roughness of ice to 0 mm and 1 mm did not allow to clearly determine, as was shown from the statistical (R^2) analysis, whether V or H should be the preferred polarization for estimating ice thickness.

Using paired daily AMSR-E T_B measurements and simulated ice thickness obtained with CLIMo for three sampling sites, simple linear regression-based ice thickness prediction equations were developed with the purpose of producing monthly lake ice thickness maps between ice-on and melt-onset dates. Overall, the estimated lake ice thickness was found to be thicker by 5-15 cm on GBL compared to GSL. Since the general ice growth rate on GSL is slower than on GBL, due to the influences of climatic controls (mostly air temperature), regional equations were proposed that are specific to the two lakes. These equations provide slightly better estimates of ice thickness compared to the global equation when compared against *in situ* measurements.

Ice thickness mapped on a monthly basis from January to April revealed that, in addition to air temperature, lake depth and snow depth on ice are two other key variables that influence ice growth rates on different sections of GBL and GSL. Monthly estimates of ice thickness determined for all ice seasons between 2002 and 2009 showed that colder winter seasons (e.g. 2003-2004) display, as expected, higher ice thickness than warmer winter seasons (e.g.

2005-2006). For ice season 2005-2006, in particular, the warmer fall conditions resulted in later freeze-up (Kang et al., 2012), thus delaying ice growth/thickening in both lakes compared to other ice seasons.

In conclusion, the AMSR-E ice thickness retrieval equations developed in this study offer the advantage over traditional *in situ* measurements and 1-D ice model in that they can be applied to estimate ice thickness at the pixel level on large northern lakes. This allows for the analysis of intra-seasonal and inter-annual variability in ice thickness on such lakes in response to climate conditions. The global and regional ice thickness regression equations proposed should be tested on other large lakes in the future (i.e. Lake Baikal, Lake Ladoga, and Lake Onega) to be determined if the equations are transferrable to other large lakes of the Northern Hemisphere found in other climate regions. In addition, a more thorough investigation of forward simulations with the HUT emission model than performed herein should be conducted by examining more closely the effect of different lake ice types (e.g. clear ice without and with bubble inclusions that act as scatterers) as well as roughness at the ice/water interface. This will require field deployments and the use of coincident synthetic aperture radar (SAR) such as TerraSAR-X to characterize ice types, as recently suggested by Gunn et al. (2010). These are two lines of inquiry that we are actively pursuing.

Chapter 7: General conclusions

7.1 Summary

In this thesis, we have presented for the first time the potential AMSR-E brightness temperature measurements to determine ice growth/thickening and timing of freeze-up and break-up on large northern lakes. The poor spatial (point) and temporal coverage of ground-based observations in most countries of the Northern Hemisphere makes passive remote sensing a desirable tool for examining both the role and response of ice cover in climate-lake interactions. The ice cover retrieval algorithms specifically developed for lake ice thickness and ice phenological events will help to analyze the response of ice cover on GBL and GSL to climate variability and change in a consistent manner since passive microwave satellite sensors provide daily acquisitions year round over the entire lake surfaces.

In addition to introductory and background material covered in Chapters 1-2, Chapter 4 showed that the temporal evolution of T_Bs at 18.7 GHz (H-pol) and its sensitivity to ice cover permits to distinguish between the timing and duration of ice phenological events (i.e. freeze-onset/melt-onset; ice-on/ice-off dates; freeze/melt duration; ice cover duration) over large lakes over seven ice seasons (2002-2009). The spatio-temporal variability of these ice phenology events is related to regional climate, latitudinal influence, lake depth, and, in particular, the influence of incoming water from Slave River for GSL. Located in a colder climate region, during the freeze-up period, both freeze-onset and ice-on dates happen about one week earlier while freeze duration lasts approximately one week longer on GBL than on GSL. Results revealed that during the break-up period melt-onset and ice-off dates occur on average one week and approximately four weeks later, respectively, on GBL while melt duration lasts about three weeks longer on this lake compared to GSL. Earlier melt over two lakes are influenced by air temperature variability and ice thickness, which can result in later freeze-onset in following winter seasons (due to greater summer heat storage). In general, ice cover duration is usually three to four weeks longer, depending on

the ice season, on GBL than GSL. Like melt-onset and ice-off date, ice cover duration is to some extent influenced by river inflow from Slave River into GSL. Results from an initial comparison between AMSR-E estimated ice phenological parameters and those from QuikSCAT, NOAA/IMS and CIS products showed that relatively coarse resolution AMSR-E 18.7 GHz H-pol T_B data are suitable for observing ice phenology on the two lakes, at least in their main basins on a regular basis.

In Chapter 5, the key finding to emerge from this thesis is that the temporal evolution of T_B at both 10.65 GHz (H-pol) and 18.7 (V-pol) in AMSR-E is associated with ice growth and thickening, corresponding to significant changes in emissivity from open water through maximum end-of-winter ice thickness. Results showed a stronger relation with ice thickness at 18.7 GHz frequency (V-pol) and 10.65 GHz (H-pol) than at 6.9 GHz. This may be due to the coarser spatial resolution of the lower frequency channel as a previous study (Hall *et al.*, 1981), using airborne data correlated with a limited number of ground survey measurements, showed a greater sensitivity of 5-6 GHz measurements to ice thickness. In this thesis, some differences in the strength of the relation were observed when comparing T_B and ice thickness estimates from a cold versus a warm winter. The strength of the relation between T_B at the 10.7 (H-pol) and 18.7 (V-pol) GHz frequencies and ice thickness was higher for the colder winter, when less inter-seasonal variability in air temperature was detected at meteorological stations located in the vicinity of the lake sites. These results suggest that T_B measurements obtained from AMSR-E offer a high potential for estimating ice thickness on large northern lakes.

In Chapter 6, another major objective was to develop a retrieval algorithm to estimate ice thickness from T_B measurements obtained from AMSR-E 18.7 GHz (V-pol) over GBL and GSL. HUT emission model results reproduced the wavy pattern observable in the temporal evolution of T_B measurements from AMSR-E during the ice growth season and further reinforced the suggestion brought forward in Chapter 5, in that 18.7 GHz (V-pol) is a suitable channel for estimating ice thickness. The ice thickness retrieval algorithm was then used to generate monthly lake ice thickness products. The estimated lake ice thickness on GBL was found to be on average 5-15 cm thicker than on GSL. Furthermore, ice growth

rate on GSL is slower than on GBL due to the influences of regional climatic controls (i.e. air temperature), and non-climatic controls (i.e. lake bathymetry and incoming water from river). The different spatial ice thickness distribution in monthly ice thickness products can be explained by the variability of lake depth, lake currents, and on-ice snow distribution.

Overall, the main contributions of this thesis are: 1) the development of an ice phenological retrieval algorithm that allows to detect all stages of ice phenology (FO, ice-on and FD; MO, ice-on and MD; and ICD); 2) the development of an ice thickness retrieval algorithm applicable from ice-on until MO dates; 3) documenting and deepening our understanding of the intra-seasonal and inter-annual variability in ice cover phenology and thickness on GBL and GSL in relation to climatic (e.g. air temperature) and non-climatic factors (e.g. lake depth, river inflow), and 4) the first comparison between AMSR-E derived ice phenology parameters with those obtainable from other existing lake ice products (NOAA/IMS and CIS). Thus, AMSR-E brightness temperature measurements present an invaluable opportunity to estimate ice phenology parameters and ice thickness on a regular basis.

7.2 Limitations

There are a few limitations identified with this study, and these were alluded to some extent in the Chapters 4 and 6 related to the development and application of retrieval algorithms on GBL and GSL. First, the relatively coarse spatial resolution of AMSR-E input the product results in a certain level of land contamination in T_B measurements along lakeshores and where a high concentration of islands exists. All ice phenological parameters reported herein were therefore also derived within confidence regions (i.e. main basins of the lakes). Compared to AMSR-E WCI dates, for example, those derived from the CIS and NOAA/IMS are considerably later in GSL as ice cover is estimated to remain longer with these two products when examining the full extent of GBL and GSL. Second, for the investigation of ice phenological events in other large lakes (i.e. Lake Ladoga and Lake Baikal), the suite of criteria developed for GBL and GSL (i.e. minimum and maximum thresholds, averages of preceding and succeeding days in the time series) may

need to be adjusted because those lakes are situated in different climate regions. Third, for the ice thickness retrieval algorithm, it was found that ice growth rates are influenced by air temperature such that the slope of the relation between T_B and ice thickness is not the same between a cold and a warm winter. The effect of inter-annual variability in air temperature should be examined more closely in future enhancements of the ice thickness product, especially if the algorithm is to be applied to other large lakes of the northern hemisphere such as Baikal and Ladoga.

7.3 Recommendations for Future work

The synergistic use of spaceborne instruments operating at a different wavelength is an effective means for monitoring lake ice phenological events and to improve ice phenological retrieval accuracy, particularly the timing of ice-on and ice-off over large northern lakes. For example, ice phenological events derived from the Quick Scatterometer (QuikSCAT), the Advanced Microwave Scanning Radiometer (AMSR-E), and the Moderate Resolution Imaging Spectroradiometer (MODIS) instruments (MODIS Lake Surface Temperature (LST) and the Normalized Difference Snow Index (NDSI)) over large northern lakes should be analyzed together and possibly blended to document the spatial and interannual variability in lake ice cover such a high latitude. Similar to the study of Kouraev et al. (2007), the combination of wide spatial coverage and good temporal resolution for passive microwave satellite (i.e. AMSR-E and SSM/I) and high radiometric sensitivity and along-track spatial resolution of recent altimetric satellites (i.e. Jason-2, ENVISAT, ICESat/GLAS, and CryoSat-2) could be tested on GBL and GSL, not only to derive ice phenology but also potentially for ice thickness. For example, the evolution of vertically polarized T_B derived from AMSR-E level 2A raw brightness temperature could be compared with ice thicknesses obtained with recent estimates from the Jason-2 Ku-band radar altimeter data (since 2008).

Long time series of passive microwave T_B measurements (over 30 years) from the SMMR and the SSM/I are seen as a valuable data source for examining the historical response of

GBL and GSL ice cover to climate conditions. New ice phenology and ice thickness retrieval algorithms (H-pol: phenology and V-pol: thickness) could be developed using 19.35 GHz T_B data (1987-2009) from SSM/I as well as 18 GHz T_B data (1979-1987) from SMMR over the two lakes in their main basin. The response of ice cover phenology and thickness would be substantiated by climate data from the GBL and GSL regions, and a limited number of ground-based observations over the period of study (e.g. Back Bay in GSL). The presence of first-order trends in ice phenological parameters and maximum ice thickness would be tested for statistical significance using the non-parametric Mann-Kendall test and the magnitude (slope) of the trends (number of days change per year) with Sen's method.

Another research topic relates to examining the polarization difference at 36.5 GHz (37.0 GHz), which is the difference between vertical and horizontal polarized brightness temperatures, derived from AMSR-E and SSM/I to determine fractional ice coverage (0 to 100 percent) during freeze-up (from freeze-onset to ice-on date) and break-up (from melt-onset to ice-off date). This ice fraction information could be evaluated from MODIS/Aqua LST and NOAA/IMS 4 km snow and ice products as well as Canadian Ice Service (CIS) lake ice fraction database. Furthermore, Arctic Radiation and Turbulence Interaction Study Sea Ice (ASI) algorithms which have developed such a product from T_B at AMSR-E 89.0 GHz (Spreen et al., 2008) should be compared with fractional ice coverage products from AMSR-E 36.5 GHz T_B measurements.

Finally, in spite of the ending of the AMSR-E mission due to a problem with the rotation of its antenna, work will continue on ice cover algorithms (ice phenology and thickness) using data from other satellite platform. SSM/I on DMSP still operate but there are new prospects as well. One source of relatively untapped data is from the U.S. Naval Research Lab WindSat satellite, which operates in discrete bands at 6.8, 10.7, 23.8, and 37.0 GHz and with similar spatial resolutions and incidence angles (50-55) as AMSR-E. Also, passive microwave T_B data are to be available from AMSR-2 onboard the Global Change Observation Mission-Water (GCOM-W1) which is scheduled to launch 2012. In addition,

the passive microwave radiometer (1.41 GHz with 40 km resolution) onboard the Soil Moisture Active Passive (SMAP) instrument is another exciting prospect that ought to expose new lake ice information in large northern lakes.

Bibliography

Adams, W. P. (1976), Diversity of lake cover and its implications. *MUSK-OX, 18*: 86-98.

Adams, W. P. and N. T. Roulet (1980), Illustration of the roles of snow in the evolution of the winter cover of a lake. *Arctic, 33*, 100-116.

Adams, W. P. and N. T. Roulet (1984), Sampling of snow and ice on lakes. *Arctic, 37*(3), 270-275.

Allison, I., R. G. Barry, and B. Goodison (2001), Climate and Cryosphere (CliC) Project. Science and co-ordination plan. Version 1, *World Climate Research Programme*, Geneva, Switzerland, WCRP-114 WMO/TD 1053.

Arcone, S. A., Yankielun, N. E., and E. F. Chacho (1997), Reflection profiling of arctic lake ice using microwave FM-CW radar, *IEEE Transactions on Geoscience and Remote Sensing, 35*(2): 436-443.

Assel, R. A., K. Cronk, and D. C. Norton. (2003), Recent trends in Laurentian Great Lakes ice cover, *Climatic Change*, 57. 185-204.

Ashton, D. G.: River and lake ice thickening, thinning, and snow ice formation. Cold Regions Science and Technology, 68(1-2), 3-19, 2011, doi:10.1016/j.coldregions.2011.05.004.

Austin, J. A., and S. M. Colman (2007), Lake superior summer water temperatures are increasing more rapidly than regional air temperatures: a positive ice-albedo feedback. *Geophysical Research Letters, 34*(6), L06604, doi:10.1029/2006GL029021.

Barry, R. G., and J. A. Maslanik (1993), Monitoring lake freeze-up/break-up as a climate indicator, in Snow Watch *'92*, edited by R. G. Barry, B. E. Goodison and E. F. LeDrew, *Glaciological Data Report GD-25,* pp. 66-79, NSIDC, University of Colorado, Boulder, CO. 66-79.

Belzile, C., W. F. Vincent, J. A. E. Gibson, P. Van Hove (2001), Bio-optical characteristics of the snow, ice, and water column of a perennially ice-covered lake in the high Arctic. *Canadian Journal of Fisheries and Aquatic Sciences, 58*, 2405-2418.

Bengtsson, L. (1986), Spatial variability of lake ice covers. *Geografiska Annaler., Series A, Physical Geography, 68*(1/2), 113-121.

Blanken, P., W. Rouse, and W. M. Schertzer (2008), The time scales of evaporation from great slave lake. In Cold Region Atmospheric and Hydrologic Studies: *The Mackenzie GEWEX Experience Volume 2: Hydrologic Processes*, Edited Ming-ko Woo, 181–196, Springer, Springer Berlin Heidelberg, in press.

Bolsenga, S. J., M. Evans, H. A. Vanderploeg, and D. G. Norton (1996), PAR transmittance through thick, clear freshwater ice. *Hydrobiologia, 330,* 227-230.

Bolsenga, S. J., and H. A. Vanderploeg (1992), Estimating photosynthetically available radiation into open and ice-covered fresh-water lakes from surface characteristics - a high transmittance case-study. *Hydrobiologia, 243/244,* 95-104.

Bolsenga, S. J., C. E. Herdendorf, and D. G. Norton (1991), Spectral transmittance of lake ice from 400-850 nm. *Hydrobiologia, 218,* 15-25.

Bolsenga, S. J. (1969), Total albedo of Great Lake ice. *Water Resources Research, 5*(5), 1132-1133.

Bonsal, B. R., T. D. Prowse, C. R. Duguay, and M. P. Lacroix (2006), Impacts of large-scale teleconnections on freshwater-ice break/freeze-up dates over Canada. *Journal of Hydrology, 330,* 340-353.

Bordonski, G. S. and S. D. Krylov (1998), Loss factor behavior of freshwater. *IEEE Transactions on Geoscience and Remote Sensing, 36*(2), 678-680.

Brown, L. C. and Duguay, C. R.: A comparison of simulated and measured lake ice thickness using a Shallow Water Ice Profiler. Hydrological Processes, 25(19), 2932-2941, 2011a. DOI: 10.1002/hyp.8087.

Brown, L.C. and Duguay, C.R.: The fate of lake ice in the North American Arctic. The Cryosphere, 5, 869-892, doi:10.5194/tc-5-869-2011, 2011b.

Brown L. C. and C. R. Duguay (2010), The response and role of ice cover in lake-climate interactions. *Progress in physical geography, 34*(4), doi:10.1177/0309133310375653.

Bryan, M. L., and R. W. Larson (1975), The study of freshwater lake ice using multiplexed imaging radar. *Journal of Glaciology, 14*(72), 445-457.

Burns, B. A., R. Shuchman, C. Mätzler, and J. Dowdeswell (1986), Analysis of multichannel SAR data of Spitsbergen, *international geoscience and remote sensing symposium*, 367-371.

Bursa, A. S. and L. Johnson (1967), Nannoplankton of Marine Origin from Great Bear Lake in the Northwest Territories of Canada, *Nature*, *214*, 528 – 529.

Chang, A. T. C., J. L. Foster, D. K. Hall, B. E. Goodison, A. E. Walker, J. R. Metcalfe, and A. Harby (1997), Snow parameters derived from microwave measurements during the BOREAS winter field campaign. *Journal of Geophysical Research, 102*(D24), 29663-29671.

Derksen C., A. Walker, and B. Goodison (2003), A comparison of 18 winter seasons of in situ and passive microwave-derived snow water equivalent estimates in Western Canada. *Remote Sensing of Environment, 88,* 271-282.

Doran, P. T., C. P. McKay, W. P., Adams, M. C., English, R. A., Wharton, and M. A., Meyer (1996), Climate forcing and thermal feedback of residual lake-ice covers in the high Arctic. Limnology and Oceanography, 41, 839–848.

Duguay, C., Brown, L., Kang, K-K., and Kheyrollah Pour, H: [Arctic]. Lake ice. [In State of the Climate in 2011]. Bulletin of the American Meteorological Society. In review.

Duguay, C., Brown, L., Kang, K-K., and Kheyrollah Pour, H: Lake ice. In Richter-Menge, J., M. O. Jeffries and J. E. Overland, Eds., *Arctic Report Card 2011*, http://www.arctic.noaa.gov/reportcard, 2011.

Duguay, C. R., T. D. Prowse, B. R. Bonsal, R. D. Brown, M. P. Lacroix, and P. Ménard, (2006), Recent trends in Canadian lake ice cover. *Hydrological Processes, 20*, 781-801.

Duguay, C. R., and P. M. Lafleur (2003a), Determining depth and ice thickness of shallow sub- Arctic lakes using space-borne optical and SAR data. *International journal of remote sensing, 24*(3), 475-489.

Duguay, C. R., G. M. Flato, M. O. Jeffries, P. Ménard, K. Morris, and W. R. Rouse (2003b), Ice-cover variability on shallow lakes at high latitudes: model simulations and observations. *Hydrological Processes, 17*, 3465-3483.

Duguay, C. R., T. J. Pultz, P. M. Lafleur, and D. Drai (2002), RADARSAT backscatter characteristics of ice growing on shallow sub-arctic lakes, Churchill, Manitoba, Canada. *Hydrological Processing*, 16, 1631-1644.

Duguay, C. R., W. R. Rouse, P. M. Lafleur, D. L. Boudreau, Y. Crevier, T. J. Pultz (1999), Analysis of muti-temporal ERS-1 SAR data of subarctic tundra and forest in the northern Hudson Bay Lowland and implications for climate studies. *Canadian Journal of Remote Sensing 25*, 21-23.

Duguay, C. R., P. M. Lafleur (1997), Monitoring ice freeze-up and break-up of shallow tundra lakes and ponds using ERS-1 SAR data. In *Proceedings of the International Symposium: Geomatics in the era of RADARSAT (GER '97)*; 6 pp. CD-ROM.

Elachi, C. (1976), Imaging radar observations of frozen arctic lakes. *Remote Sensing of Environment, 5*, 169-175.

Environment Canada, 2010. Ice Thickness Program Collection. Canadian Ice Service (http://www.ec.gc.ca/glaces-ice/default.asp?lang=En&n=E1B3129D-1).

Eppler, D. T., L. D. Farmer, A. W. Lohanick, M. R. Anderson, D. J. Cavalieri, J. C. Comiso, P. Gloersen, C. Garrity, T. C. Greenfell, M. Hallikainen, J. A. Maslanik, C. Mätzler, R. A. Melloh, I. Rubinstein, and C. T. Swift (1992), Passive Microwave Signatures of Sea Ice. In Microwave Remote Sensing of Sea Ice, Edited Frank D. Carsey, 47-72, Geophysical Monograph 68, American Geophysical Union, Washington, DC.

Frenette, J-J., P. Thibeault, J-F., Lapierre (2008), Presence of algae in freshwater ice cover of fluvial Lac Saint-Pierre (St. Lawrence River, Canada). *Journal of Phycology, 44*, 284-291.

French, H. M., and O. Slaymaker, (1993), Canada's cold environments. Montreal and Kingston: McGill-Queen's University Press.

Gloersen, P. (1973), Passive microwave images of lake ice, *Significant Accomplishments in Sciences*, Proceedings of a symposium held 7-8 November, 1972 at the NASA Goddard Space Flight Center. NASA SP-331. Washington, DC: National Aeronautics and Space Administration, 1973, 187-189.

Gough, W.A., Gagnon, A.S., and Lau, H.P.: Interannual variability of Hudson Bay ice thickness. Polar Geography, 28 (3), 222-238, 2004.

Grenfell T. C., and J. C. Comiso (1986), Multifrequency Passive Microwave Observations of First-Year Sea Ice Grown in a Tank. *IEEE Transactions on Geoscience and Remote Sensing*, *GE-24*(6), 826-831.

Gunn, G. E., C. R., Duguay, C., Derksen, J., Lemmetyinen, and P. Toose (2010a), Evaluation of the Helsinki University of Technology's modified snow emission model over lake ice using airborne passive microwave measurements. *Remote Sensing of Environment, 115(1),* 233-244.

Gunn, G. E (2010b), An investigation into the effects of variable lake ice properties on passive and active microwave measurements over tundra lakes near Inuvik, N.W.T, *Master's Thesis at University of Waterloo*, Waterloo, Ontario, Canada

Hall, D. K., G. A., Riggs, J. L. Foster, S. V., Kumar (2010), Development and evaluation of a cloud-gap-filled MODIS daily snow-cover product. *Remote Sensing of Environment*, *114* (3), 496-503.

Hall, D. K., J. E. Box, K. A. Casey, S. J. Hook, C. A. Shuman, and K. Steffen (2008), Comparison of satellite-derived and in-situ observations of ice and snow surface temperature over Greenland. *Remote Sensing of environment,112,* 3739-3749.

Hall, D. K., G. A., Riggs, and V. V. Salomonson (2001), Algorithm Theoretical Basis Document (ATBD) for the MODIS Snow and Sea Ice-Mapping Algorithms. http://modis-snow-ice.gsfc.nasa.gov/atbd.html.

Hall, D. K., D. B. Fagre, F. Klasner, G. Linebaugh, and G. E. Liston (1994), Analysis of ERS 1 synthetic aperture radar data of frozen lakes in northern montana and implications for climate studies. *Journal of Geophysical Research, 99*(C11): 22,473-22,482.

Hall, D. K. (1993), Active and passive microwave remote sensing of frozen lakes for regional climate studies No. *Glaciological data rep D-25* in Barry, R. G., Goodison, B. E., and Ledrew, E. F. (eds.).

Hall, D. K., J. L. Foster, A. T. C. Chang, and A. Rango (1981), Freshwater ice thickness observations using passive microwave sensors. *IEEE Transactions on Geoscience and Remote Sensing, GE-19*(4), 189-193.

Helfrich, S. R., D. McNamara, B. H. Ramsay, T. Baldwin and T. Kasheta (2007), Enhancements to, and forthcoming developments in the Interactive Multisensor Snow and Ice Mapping System (IMS). *Hydrological processes, 21*, 1576-1586.

Hewison, T. J. (2001), Airborne measurements of forest and agricultural land surface emissivity at millimeter wavelengths. *IEEE Transactions on Geoscience and Remote Sensing*, *39*(2), 393-400.

Hewison, T. J., and S. J. English (1999), Airborne retrievals of snow and ice surface emissivity at millimeter wavelengths. *IEEE Transactions on Geoscience and Remote Sensing*, *37*, 1871−1879.

Hirose, T., M. Kapfer, J. Bennett, P. Cott, G. Manson, and S. Solomon (2008), Bottomfast ice mapping and the measurement of ice thickness on tundra lakes using C-band synthetic aperature radar remote sensing, *Journal of the American Water Resources Association, 44*(2), 285-292.

Hinzman, L. D., D. J. Goering, and D. L. Kane (1998), A distributed thermal model for calculating soil temperature profiles and depth of thaw in permafrost regions, *Journal of Geophysical Research, 103(*D22), 28975-28991

Howell, S. E. L., L. C. Brown, K.-K. Kang, and C. R. Duguay (2009a), Lake ice phenology variability on Great Bear Lake and Great Slave Lake, Northwest Territories, Canada, from SeaWinds/QuikSCAT: 2000-2006. *Remote Sensing of Environment, 113*, 816-834.

Howell, S. E. L., C. R. Duguay, T. Markus (2009b), Sea ice conditions and melt season duration variability within the Canadian Arctic Archipelago: 1979-2008. *Geophysical Research Letters, 36*(L10502), doi:10.1029/2009GL037681.

Iliescu, D., and I. Baker, (2007), The structure and mechanical properties of river and lake ice. *Cold Regions Science and Technology 48,* 202-217.

Jakkia, J., M. Leppäranta, T. Kawamura, K. Shirasawa, and K. Salonen (2009), Radiation transfer and heat budget during the ice season in Lake Pääjärvi, Finland. *Aquatic Ecology, 43*(3), 681-692.

Jeffries, M. O. and K. Morris, (2007), Some aspects of ice phenology on ponds in central Alaska, USA. *Annals of Glaciology, 46,* 397-403.

Jeffries, M. O. and K. Morris, (2006), Instantaneous daytime conductive heat flow through snow on lake ice in Alaska. *Hydrological Processes, 20,* 803-815.

Jeffries, M. O., K. Morris, and C. R. Duguay, (2005a) Lake ice growth and decay in central Alaska, USA: observations and computer simulations compared. *Annals of Glaciology, 40,* 195-199.

Jeffries, M. O., K. Morris, and N. Kozlenko, (2005b) Ice characteristics and processes, and remote sensing of frozen rivers and lakes in *Remote sensing in northern hydrology: Measuring environmental change.* Edited by Duguay, C.R. and A. Pietroniro, Geophysical Monograph 163, American Geophysical Union, Washington, DC, 63-90.

Jeffries, M. O., K., Morris, and G. E. Liston, 1996. A method to determine lake depth and water availability on the North Slope of Alaska with spaceborne imaging radar numerical ice growth modeling, *Arctic,* 49(4), 367-374.

Jeffries, M. O., K., Morris, W. F., Weeks, and H. Wakabayashi, (1994), Structural and stratigraphic features and ERS 1 synthetic aperture radar backscatter characteristics of ice growing on shallow lakes in NW Alaska, winter 1991-1992. *Journal of Geophysical Research, 99*(C11), 22459-22471.

Jeffries, M. O., H., Wakabayashi, W. F. Weeks, (1993), ERS-1 SAR backscatter changes associated with ice growing on shallow lakes in Arctic Alaska. *IEEE Transactions on Geoscience and Remote Sensing, 4*, 2001-2004.

Jensen, J. R. (2007), *Remote sensing of environment: An Earth Resource Perspective*, 249-261, Pearson Prentice-Hall, Upper Saddle River, in press.

Jensen, O. P., B. J. Benson, J. J. Magnuson, V. M. Card, M. N. Futter, P. A. Soranno, K. M. Stewart (2007), Spatial analysis of ice phenology trends across the Laurentian Great

Lakes region during a recent warming period. *Liminology and Oceanography, 52*(5), 2013-2026.

Johnson, L. (1975), Physical and chemical characteristics of Great Bear Lake, Northwest Territories. *Journal of the fisheries research board of Canada, 32*(11), 1971-1987.

Kaleschke, L., Tian-Kunze, X., Maaß, N., Mäkynen, M., and Drusch, M.: Sea ice thickness retrieval from SMOS brightness temperatures during the Arctic freeze-up period. Geophysical Research Letters, 39, L05501, doi:10.1029/2012GL050916, 2012.

Kang. K-K, C. R. Duguay, S. E. L. Howell, C. P. Derksen, and R. E. J. Kelly (2010), Sensitivity of AMSR-E Brightness Temperatures to the Seasonal Evolution of Lake Ice Thickness, *Geoscience and Remote Sensing Letters, 7*(4), 751-755.

Kang. K-K, C. R. Duguay, and S. E. L. Howell (2012a), Estimating ice phenology on large northern lakes from AMSR-E: algorithm development and application to Great Bear Lake and Great Slave Lake, Canada, *The Cryosphere, 6*(2), 235-254.

Kang. K-K, C. R. Duguay, J. Lemmetyinen, and Y. Gel (2012b), Development of ice thickness retrieval algorithms for large northern lakes from spaceborne brightness temperature measurements *in preparing the submission of the Cryosphere.*

Kelly, R. E. J. (2009). The AMSR-E snow depth algorithm: Description and initial results. *Journal of the Remote Society of Japan, 29*(1), 307-317.

Kelly, R. E. J., A. T. C. Chang, L. Tsang, and J. L. Foster (2003), Development of a prototype AMSR-E global snow area and snow volume algorithm, *IEEE Transactions on Geoscience and Remote Sensing, 41*(2), 230-242.

Key, J. and others (2007). Integrated Global Observing Strategy Cryosphere Theme Report, *WMO/TD-No. 1405*, World Meteorological Organization, Geneva, 100 pp.

Kheyrollah Pour, H., Duguay, C.R., Martynov, A., and Brown, L.C.: Simulation of surface temperature and ice cover of large northern lakes with 1-D models: A comparison with MODIS satellite data and *in situ* measurements. *Tellus Series A: Dynamic Meteorology and Oceanography*, 64, 17614, DOI: 10.3402/tellusa.v64i0.17614, 2012.

Kim E. J. and A. W. England (2003). A yearlong comparison of plot-scale and satellite footprint-scale 19 and 37 GHz brightness of the Alaskan North Slope, *Journal of Geophysical Research, 108*(D13): 4388, doi:10.1029/2002JD002393.

Kozlenko, N., and M. O. Jeffries (2000), Bathymetric mapping of shallow water in thaw lakes on the North Slope of Alaska with spaceborne imaging radar. *Arctic, 53*(3): 306-316.

Kouraev, A. V., S. V. Semovski, M. N. Shimaraev, N. M. Mognard, B. Legresy, and F. Remy (2007a), Observations of Lake Baikal ice from satellite altimetry and radiometry. *Remote Sensing of Environment*, *108*(3), 240-253.

Kouraev, A. V., S. V. Semovski, M. N. Shimaraev, N. M. Mognard, B. Legresy, and F. Remy (2007b), The ice regime of Lake Baikal from historical and satellite data: Relationship to air temperature, dynamical, and other factors. *Limnology and Oceanography*, *52*(3), 1268-1286.

Launiainen, J., and B. Cheng (1998), Modeling of ice thermodynamics in natural water bodies. *Cold Regions Science and. Technologyl. 27*, 153–178.

Latifovic, R. and D. Pouliot (2007), Analysis of climate change impacts on lake ice phenology in Canada using the historical satellite data record. *Remote sensing of Environment, 106,* 492-507.

Leconte, R. and P. D. Klassen (1991), Lake and river ice investigations in northern Manitoba using airborne SAR Imagery. *Arctic, 44*(1), 153-163.

Lemmetyinen, J., Kontu, A., Kärnä, J-P., Vehviläinen, J., Tatias T., and Pulliainen, J.,: Correcting for the influence of frozen lakes in satellite microwave radiometer observations through application of a microwave emission model. Remote Sensing of Environment, 115, 3695-3706, 2011.

Lemmetyinen, J., J. Pulliainen, A. Rees, A. Kontu, and Y. Qiu, and C. Derksen (2010), Multiple-Layer adaptation of HUT snow emission model: comparison with experimental data. *IEEE Transactions on Geoscience and Remote sensing*, *48*(7), 2781-2794.

Lemmetyinen, J., C. Derksen, J. Pulliainen, W. Strapp, P. Toose, A. Walker, S. Tauriainen, J. Pihlflyckt, J.-P. Kärnä, and M. T. Hallikainen (2009), A comparison of airborne microwave brightness temperatures and snowpack properties across the boreal forests of Finland and Western Canada. *IEEE Transaction on Geoscience and Remote Sensing*, *47*(3), 965–978.

Lenormand, F., C. R. Duguay, and R. Gauthier (2002), Development of a historical ice database for the study of climate change in Canada, *Hydrological Processes, 16*, 3707-3722.

León, L.F., Lamb, D. C. L., Schertzerb, W. M., Swaynea, D. A., and Imbergerc, J.: Towards coupling a 3D hydrodynamic lake model with the Canadian Regional Climate Model: Simulation on Great Slave Lake, Environmental Modelling & Software, 22, 787-796, 2007.

Leshkevich G. A. and S. V. Nghiem (2007), Satellite SAR Remote Sensing of Great Lakes Ice Cover, Part 2. Ice Classification and Mapping. *Journal of Great Lakes Research, 33*, 736-750.

Leshkevich, G. A. (1985), Machine classification of freshwater ice types from Landsat-1 digital data using ice albedos as training sets, *Remote Sensing of Environment, 17*(3), 251-263.

Leshkevich, G. A. (1988), Non-Lambertian reference panel effect on spectral reflectance measurements of freshwater ice. *International Journal of Remote sensing, 9,* 825-883.

Leverington, D. W. and C. R. Duguay (1997), A neural network method to determine the presence or absence of permafrost near Mayo, Yukon Territory, Canada. *Permafrost and Periglacial Processes, 8,* 205-215.

Livingstone, D. M. (1997), Break-up dates of alpine lakes as proxy data for local and regional mean surface air temperatures. *Climatic Change, 37*(2), 407-439.

Long, D., and B. Hicks (2005) Standard BYU QuikSCAT/SeaWinds land/ice image products. *Report Provo*, Utah. Brigham Young University.

Lopes, R. M. C, K. L. Mitchell, S. D. Wall, G. Mitri, M. Janssen, S. Ostro, R. L. Kirk, A. G. Hayes, E. R. Stofan, J. I. Lunine, R. D. Lorenz, C. Wood, J. Radebaugh, P. Paillou, H. Zebker, and F. Paganelli (2007), The Lakes and Seas of Titan, *Eos Trans. AGU, 88*(51), doi:10.1029/2007EO510001.

Magnuson, J. J., D. M. Robertson, B. J. Benson, R. H. Wynne, D. M. Livingstone, T. Arai, R. A. Assel, R. G. Barry, V. Card, E. Kuusisto, N. G. Granin, T. D. Prowse, K. M. Stewart, V. S. Vuglinski (2000), Historical Trends in Lake and River Ice Cover in the Northern Hemisphere, *Science, 289*(5485), 1743 – 1746, doi: 10.1126/science. 289.5485.1743

Maslanik. J. A. and R. G. Barry (1987). Lake Ice Formation and Breakup as an Indicator of Climate Change: Potential for Monitoring Using Remote Sensing Techniques. *The Influence of Climate Change and Climatic Variability on the Hydrologic Regime and Water Resources*, International Association of Hydrological Sciences Press, *IAHS Publ. No. 168*, 153-161.

Matsuoka, T., S. Mae, H. Fukazawa, S. Fujita, and O. Watanabe (1998), Microwave dielectric properties of the ice core from Dome Fuju, Antarctica. *Geophysical Research Letters, 25*(10), 1573-1576.

Matsuoka, T., S. Fujita, and S. Mae (1996), Effect of temperature on dielectric properties of ice in the range 5–39 GHz. *Journal of Applied Physics, 80*(10), 5884-5890.

Mätzler, C. and U. Wegmüller (1987), Dielectric properties of fresh-water ice at microwave frequencies, *Journal of physics D: Applied Physics, 20*, 1623-1680.

Mckay, C. P., G. D. Clow, R. A. Wharton Jr., and S. W. Squyres (1985), Thickness of ice on perennially frozen lakes. *Nature, 313*(14), 561-562.

Melloh, R. A., D. T. Eppler, L. D. Farmer, L. W. Gatto, and E. F. Chacho (1991), Interpretation of passive microwave imagery of surface microwave imagery of surface snow and ice, Harding Lake, Alaska, *CRREL REP. 91-11,* 30 pp., U.S. Army Cold Reg. Res. And Eng. Lab., Hanover, NH.

Melloh, R. A. and L. W. Gatto (1990), Interpretation of passive and active microwave imagery over snow-covered lakes and rivers near Fairbanks Alaska, *proceedings of the workshop on applications of remote sensing in hydrology, Saskatoon*, 259-278.

Mellor, J, C., Bathymetry of Alaskan Arctic lakes: a key to resource inventory with remote sensing methods, *Ph. D. thesis*, Univ. of Alaska, Fairbanks, 1982.

Ménard, P., C. R. Duguay, G. M. Flato, and Rouse (2002), Simulation of ice phenology on Great Slave Lake, Northwest, Territories, Canada. *Hydrological Processes, 16*, 3691-3706.

Moore, D. B. H., and A. F. Gregory (1977), The use of satellite imagery for monitoring ice break-up along the Mackenzie river, N.W.T., *Arctic, 30*(4), 234-242.

Morris, K., M. O. Jeffries, and W. F. Weeks (1995), Ice processes and growth history on arctic and sub-arctic lakes using ERS-1 SAR data. *Polar Record*, 31(177): 115-128.

Mullen, P. C. and S. T. Warren (1988), Theory of the optical properties of lake ice. *Journal of Geophysical Research 93*, 8403-8414.

Naoki, K., J. Ukita, F. Nishio, M. Nakayama, J. C. Comiso, and A. Gasiewski (2008), Thin sea ice thickness as inferred from passive microwave and in situ observations, *Journal of Geophysical Research, 113*, C02S16, doi:10.1029/2007JC004270.

Nghiem, S. V. and G. A. Leshkevich (2007), Satellite SAR Remote Sensing of Great Lakes Ice Cover, Part 1. Ice Backscatter Signatures at C-Band. *Journal of Great Lakes Research, 33*, 722-735.

Nolan, M., G. Liston, P. Prokein, J. Brigham-Grette, V. L. Sharpton, and R. Huntzinger (2003), Analysis of lake ice dynamics and morphology on Lake El'gygytgyn, NE Siberia, using synthetic aperture radar (SAR) and Landsat, *Journal of Geophysical Research, 108*(D2), 8162, doi:10.1029/2001JD000934.

Page, D. F. and R. O. Ramseier (1975), Application of radar techniques to ice and snow studies. *Journal of Glaciology, 15*(73), 171-191.

Palecki, M. A, and R. G. Barry (1986), Freeze-up and break-up of lakes as an index of temperature changes during the transition seasons: a case study for Finland. *Journal of Climate and Applied Climatology, 25*, 893–902.

Parashar, S. K., C. Roche, and R. D. Worsfold (1978), Four channel synthetic radar imagery results of freshwater ice and sea ice in Lake Melvile. C-CORE Publication 78-11. St. John's:Memorial University, Centre for Cold Ocean Resources Engineering. 16p.

Petrov, M. P., A-Y. Terzhevik, N. I. Palshin, R. E. Zdorovennov, and G. E. Zdorovennova (2005), Absorption of solar radiation by snow-and-ice cover of lakes. *Water Resources, 32*(5), 496-504.

Pilant, D. (1995), SSM/I time series observations of Great Lakes ice and snow, in *Proceedings of the 52nd Eastern Snow Conference*, Toronto, Canada, pp. 21-25.

Rannie, W. F. (1983), Breakup and freezeup of the red river at Winnipeg, Manitoba Canada in the 19th century and some climatic implications, *Climate change, 5*(3), 283-296.

Rees, W. G. (2006), *Remote sensing of snow and ice*, 118-121, Taylor & Francis, in press.

Reid, T and N. Crout (2008), A thermodynamic model of freshwater Antarctic lake ice, *Ecological modeling*, 210, 231-241.

Routlet, N. T., and W. P. Adams (1986), Spectral distribution of light under a sub-arctic winter lake cover. *Hydrobiologia*, 134, 89-95.

Rouse, W. R., P. D. Blanken, N. Bussières, C. J. Oswald, W. M. Schertzer, C. Spence, and A. E. Walker (2008a), An Investigation of the Thermal and Energy Balance Regimes of Great Slave and Great Bear Lakes," *J. Hydrometeor.*, 9(6), 1318-1333.

Rouse, W. R., P. D. Blanken, C. R. Duguay, C. J. Oswald and W. M. Schertzer (2008b), "Climate-Lake Interactions," in *Cold Region Atmospheric and Hydrologic Studies: The Mackenzie GEWEX Experience Volume 2*: *Hydrologic Processes*, Edited Ming-ko Woo, 139–160, Springer, Berlin Heidelberg, in press.

Rouse, W. R. (2008c), Forty-five years in climatology-a personal odyssey, *The Canadian Geography*, 52(1), 5-21.

Rouse, W. R., J. Binyamin, P. D. Blanken, N. Bussieres, C. R. Duguay, C. J. Oswald, W. M. Schertzer, and C. Spence (2008d), The influence of lakes on the regional energy and water balance of the central Mackenzie river basin. In Cold Region Atmospheric and

Hydrologic Studies: *The Mackenzie GEWEX Experience Volume 1*: *Atmospheric Processes*, Edited Ming-ko Woo, 309–325, Springer, Berlin Heidelberg, in press.

Schertzer, W. M., W. R. Rouse, P. D. Blanken, A. E. Walker, D. C. L. Lam, and L. Leon (2008), Interannual variability of the thermal components and bulk heat exchange of Great Slave Lake. In Cold Region Atmospheric and Hydrologic Studies: *The Mackenzie GEWEX Experience Volume 2: Hydrologic Processes*, Edited Ming-ko Woo, 197–219, Springer, Berlin Heidelberg, in press.

Schertzer, W. M., W. R. Rouse, P. D. Blanken and A. E. Walker (2003), Over-Lake Meteorology and Estimated Bulk Heat Exchange of Great Slave Lake in 1998 and 1999, *Journal of Hydrometeorology, 4:*649-659.

Seidou, O., T. Ouarda, L. Bilodeau, M. Hessami, A. St-Hilaire, and P. Bruneau (2006), Modeling ice growth on Canadian lakes using artificial neural networks, *Water Resources Research, 42*, W11407, doi:10.1029/2005WR004622.

Sellmann, P. V., W. F. Weeks, and W. J. Campbell (1975), Use of side-looking airborne radar to determine lake depth on the Alaskan north slope. *Available from the National Technical Information Service, A01 in microfiche. Special Report 230*, 7 pp.

Serreze, M. C. and R. G. Barry (2005), The Arctic Climate System, Cambridge University Press, Edinburgh, in press.

Skinner, W. R. (1993), Lake Ice Conditions as a Cryospheric Indicator for Detecting Climate Variability in Canada, *in Snow Watch '92 –Detection Strategies for Snow and Ice*, edited by Barry, R. G., Goodison, B. E., and Ledrew, E. F., Glaciological data rep. GD-25, World Data Center A, 204–240.

Skorve, J. and P. Vincent (1987), Some models of ice melt on high level lakes in southwest Norway, *Photogrammetric engineering and remote sensing, 53*(11), 1565-1570.

Spreen, G., L. Kaleschke, and G. Heygster (2008), Sea ice remote sensing using AMSR-E 89-GHz channels, *Journal of Geophysical Research, 113,* C02S03, doi:10.1029/2005JC003384

Surdyk, S (2002), Using microwave brightness temperature to detect short-term surface air temperature changes in Antarctica: An analytical approach. *Remote Sensing of Environment, 80,* 256-271.

Svendsen, E., K. Kloster, B. Farrelly, O. M. Johannessen, J. A. Johannessen, W. J. Campbell, P. Gloerse, D. Cavalieri, C. Mätzler (1983). Norwegian remote sensing experiment: Evaluation of the Nimbus 7 scanning multichannel microwave radiometer of sea ice research, *Journal of Geophysical Research, 88*, 2781-2791.

Swift, C. T., W. L. Jones, R. F. Harrington, J. C. Fedors, R. H. Couch, and B. L. Jackson (1980), Microwave radar and radiometric remote-sensing measurements of lake ice. *Geophysical Research Letters, 7*(4), 243-246.

Toose, P. (2007), The Influence of Snow Cover Variability and Tundra Lakes on Passive Microwave Remote Sensing of Late Winter Snow Water Equivalent in the Hudson Bay Lowlands. *Master thesis*, Univ. of Waterloo, 2007.

Ulaby, F. T., R. K. Moore, and A. K. Fung, (1986, 1982, 1981), Microwave remote sensing: active and passive, Vols. 1, 2 and 3, Addison-Wesley Publishing Company, MA.

Vuglinsky, V.S., Gronskaya, T.P., and Lemeshko, N.A.: Long-term characteristics of ice events and ice thickness on the largest lakes and reservoirs of Russia. Ice in the Environment: Proceedings of the 16th IAHR International Symposium on Ice Dunedin, New Zealand, 2nd–6th December 2002, International Association of Hydraulic Engineering and Research, 2002.

Wakabayashi, H., M. O. Jeffries, and W. F. Weeks (1993), C-band SAR backscatter from ice on shallow tundra lakes: observations and modeling. In: *Proc. First ERS-1 Symp.*, (4-6 November 1992, Cannes, France), ESASP-359: 333-337.

Walter, K. M., M. Engram, C. R. Duguay, M. O. Jeffries, and F.S. Chapin, III (2008), The potential use of synthetic aperture radar for estimating methane ebullition from Arctic lake. *Journal of the American Water Resources Association, 44*(2), 305-315.

Walker, A. E., A. Silis, J. Metcalf, M. Davey, R. Brown, and B. Goodison (2000), Snow cover and lake ice determination in the MAGS region using passive microwave satellite and conventional data. *Proc. Fourth Scientific Workshop for the Mackenzie GEWEX Study (MAGS),* Montreal, QC, Canada, NSERC and AES, Environment Canada, 89–91.

Walker, A. E., and M. R. Davey (1993), Observation of Great Slave Lake ice freeze-up and break-up processes using passive microwave satellite data. *Proceedings of the 16th Canadian Symposium on Remote Sensing*, 233-238, Sherbrooke, Quebec.

Weydahl, D. J. (1993), Detecting seasonal changes at Nordic latitudes using ERS-1 SAR images. *Geoscience and Remote Sensing Symposium,. IGARSS '93,* 3: 1462-1464.

Weyhenmeyer, G. A., A. K. Westöö, and E. Willén (2008), Increasingly ice-free winters and their effects on water quality in Sweden's largest lakes. *Hydrobiologia, 599,* 111-118.

Weeks, W. F., P. V. Sellman, and W. J. Campbell (1977), Interesting features of radar imagery of ice-covered North Slope lakes. *Journal of Glaciology, 18,* 129-136.

Weeks, W. F., A. G. Fountain, M. L. Bryan, and C. Elachi (1978), Differences in radar returns from ice-covered North Slope lakes. *Journal of Geophysical Research, 83*, 4069-4073.

Weeks, W. F., A. J. Gow, and R. J. Schertler (1981), Ground-truth observations of ice-covered North Slope lakes imaged by radar, *CRREL Res. Rep. 81-19*, 17pp., U. S. Army Cold Reg. Res. And Eng. Lab., Hanover, N.H., 1981.

White, D. M., P. Prokein, M. K. Chambers, M. R. Lilly, and H. Toniolo (2008), Use of synthetic aperture radar for selecting Alaskan Lakes for winter water use, *Journal of the American Water Resources Association, 44*(2), 276-284.

Williams, S. G. and H. G. Stefan (2006), Modeling of lake ice characteristics in north America using climate, geography, and lake bathymetry. *Journal of Cold Regions Engineering, 20*(4), 140-167.

Willmott, C. J., S. M. Robeson, and K. Matsuura (2011), A refined index of model performance. International Journal of Climatology, doi: 10.1002/joc.2419, 2011.

Wiesnet, D. R. (1979). Satellite studies of freshwater ice movement on Lake Erie. *Journal of glaciology, 24*, 415-426.

Woo, M-K., W. R., Rouse, R. E., Stewart, and J. M. R. Stone, (2008). The Mackenzie GEWEX Study: A contribution of cold region atmospheric and hydrologic sciences. In Ming-ko Woo (Ed.), *Cold region atmospheric and hydrologic studies: The Mackenzie GEWEX experience Volume 1: Atmospheric dynamics*, Edited M. K. Woo, Springer-Verlag, Berlin, Germany. Ch. 11, pp. 181–196.

Woo, M-K., P. Modeste, L. Martz, J. Blondin, B. Kochtubajda, D. Tutcho, J. Gyakum, A. Takazo, C. Spence, J. Tutcho, P. Di Cenzo, G. Kenny, J. Stone, I. Neyelle, G. Baptiste, M. Modeste, B. Kenny, and W. Modeste (2007). Science meets traditional knowledge: water and climate in the Sahtu (Great Bear Lake) region, Northwest Territories, Canada. *Arctic*, Vol. 60, No. 1, 37-46.

Woo, M. (1985), Focus:Hydrology of snow and ice. *The Canadian Geographer, 29*(2): 173-183.

Worsfold, R. D., S. K. Parashar, D. C. Strong (1981), The Lake Melville/Labrador offshore synthetic aperture radar study- Winter 1979, *Canadian Symposium on Remote Sensing, 6th, Halifax, Canada.*

Wynne R. H. and T. M. Lillesand (1993), Satellite observation of lake ice as a climate indicator: initial results from statewide monitoring in Wisconsin. *Photogrammetric engineering and remote sensing, 59*(6), 1023-1031.

Wynne, R. H., J. J. Magnuson, M. K. Clayton, T. M. Lillesand, and D. C. Rodman (1996), Determinants of temporal coherence in the satellite-derived 1987-1994 break-up dates of lakes on the Laurentian Shield, *Limnology and Oceanography*, *41*(5), 832-838.

Zaier, I, C. Shu, T. Ouarda, O. Seidou, F. Chebana (2010), Estimation of ice thickness on lakes using artificial neural network ensembles, *Journal of Hydrology*, *383,* 330-340.

Zhang, T., R. L. Armstrong, and J. Smith (2003), Investigation of the near-surface soil freeze-thaw cycle in the contiguous United States: Algorithm development and validation. *Journal of Geophysical Research, 108*(D22), 8860-8874.